Characterization of two-phase flow in non-deformable and deformable porous media

Fredrik Kvalheim Eriksen

Thesis submitted for the degree of Master of Science

Department of Physics
University of Oslo

October 2012

Acknowledgements

I would like to use this opportunity to thank the people who made the writing of of this thesis possible. First of all, I want to direct a special thanks to my supervisor Knut Jørgen Måløy for giving me an assignment in this exiting field of research. He has guided me through the year by giving me valuable theoretical and practical advices as well as giving me the opportunity to work with and control the project on my own. It is also worth to mention that I attended two courses he lectured, where I learned a lot of the experimental thinking I have used during this project.

I also want to thank Ken Tore Tallakstad for sharing office with me during the time of this project and for upgrading the lightbox, Mihailo Jankov for all the valuable help with experimental equipment and supplies, Michael for showing me the PIV software and explaining its principles, and Rene Castberg for practical tips and help with equipment.

I would also give a thanks to the rest of the people in the complex group for being a generally helpful and nice group of people.

Finally, my parents Jon Amund Eriksen and Jannecke Kvalheim deserve a thanks for their support and help, both before and during the work with this thesis.

Oslo, September 2012

Contents

Chapter 1

Introduction and motivation

Flow of fluids in porous media is a process that can be found in many situations in nature as well as in industrial processes. Examples are oil recovery,

The work in this thesis is focused on investigating horizontal two phase flow in a quasi two dimensional porous media. The porous media specimen is created within a radial Hele-Shaw cell, which consists of two parallell glass discs separated with a small distance. Experiments were performed on porous media samples having three different border conditions:

1. Non-deformable: The radial Hele-Shaw cell is filled with a disordered monolayer of spherical glass beads of 1mm diameter. The beads are glued to the plates of the cell, which makes the porous media non-deformable.
2. Constricted deformable: The radial Hele-Shaw cell is packed with an approximate monolayer of ∼1mm spherical glass beads. The beads are *not* glued to the plates of the cell, but they are confined to the cell volume by an elastic constriction around the rim. The constriction is permeable to fluids and makes the porous media deformable to some extent.
3. Open Deformable: The radial Hele-Shaw cell is packed with an approximate monolayer of ∼1mm sperical glass beads. The beads are neither glued to the plates of the cell or constricted at the rim. Since the beads are free to leave the cell at the rim, the porous media is called open deformable.

Chapter 2

Porous media, fluids and flow

This chapter presents the basic theory and parameters of porous media, fluids and flow. Then, the basic theory is used to explain the principles of *two phase flow in porous media*. Towards the end, the basic ideas of *fractals* are introduced and linked to their use in characterizing two phase flow patterns.

2.1 Defining parameters and properties

There are several parameters and properties of porous media, fluids and flow. They are helpful in characterizing different aspects of porous media, fluids and flow as well as they are required in certain calculations. We will look at some important parameters and give them a simple yet sufficient explanation.

2.1.1 Characteristics of Porous Media

A porous media is a material or an envionment which is filled with internal voids. These voids are often interconnected by tiny tunnels or openings. The voids are called pores and the interconnections are called pore necks [1]. There are many different kinds of porous media, e.g. sand, limestone, concrete and sponge. Porous media may be deformable or rigid, organized or random. An example of a deformable porous media is a volume of randomly packed particles, like sand. A non-deformable porous media can be a solid material full of randomly sized and positioned voids like limestone. Since there are many varieties of porous media, some parameters are necessary to define material properties.

Porosity

An essential property of a porous media is its porosity. This is a quantitative measure of how porous a material actually is, as porosity ϕ is defined as the ratio of pore space volume V_P to the total volume of the object V_T [2],

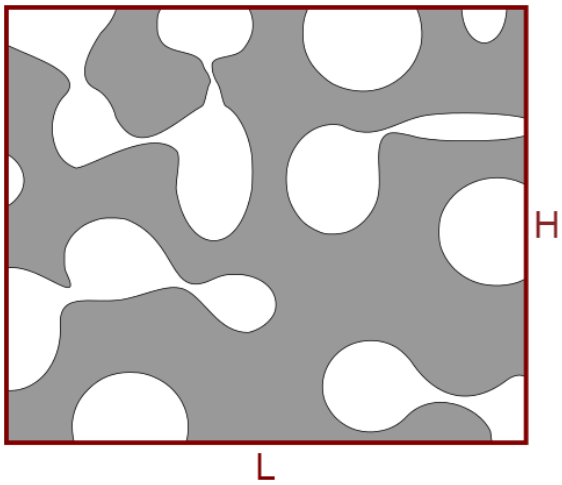

Figure 2.1: A two dimensional porous media is illustrated with white pore space and grey material matrix. The total "volume" of the porous material is given by the total area it occupies, indicated by the red square. The porosity is seen the ratio of the white area to the area of the red rectangle.

$$\phi = \frac{V_P}{V_T}. \tag{2.1}$$

This ratio is illustrated in fig. 2.1.

The porosity of a material is a dimensionless number from 0 to 1, where $\phi = 0$ indicates a completely solid material. As a reference, porosities in soil varies between 0.02 and 0.4, making this porosity interval interesting in petroleum industry [2].

Saturation

The pores and pore necks creating the pore space of a material are normally filled with one or more fluids. It is interesting to know the saturation of fluids in the pore space of a material, so saturation S_F is defined as the ratio of fluid volume V_F to the pore space volume V_P [2],

$$S_F = \frac{V_F}{V_P}. \tag{2.2}$$

Saturation of a fluid is a dimensionless quantity between 0 and 1, where $S_F = 1$ means that the entire pore space is filled with that fluid. On the other hand, if a fluid 1 has a saturation $S_1 < 1$, it is clear that the rest of the pore space is filled with one or more additional fluids in order to satisfy

$$\sum_i S_i = 1, \tag{2.3}$$

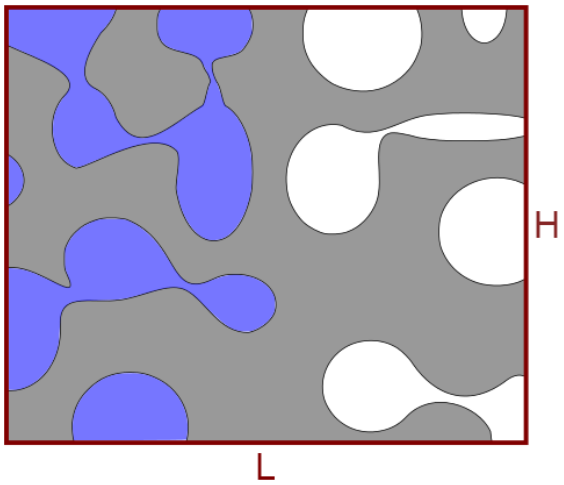

Figure 2.2: The rectangular two dimensional porous media with its pore space saturated by two fluids. It is easy to see that the sum of the fluid "volumes" is the same as the pore space shown in figure 2.1.

where S_i is the saturation of fluid i in the pore space. Equation (2.3) arises from the assumption that the entire pore space volume is filled with *some* fluid. Figure 2.2 illustrates the same porous media as in fig. 2.1 saturated with two fluids.

Randomness

The organization of the pore space, i.e. the size distribution and positions of pores and pore necks, is an important property of a porous medium. The extremes of such organization are on one side a pore space completely organized in space with no size distribution, and on the other side no organization in space and the widest possible size distribution. In nature the organization of the pore space is somewhere in between [1].

Unless the pore space is completely organized, it is not straight forward to describe the pore and pore neck positions. We would need a list of all positions, which would require a ton of work to obtain. A more simple way to indicate the randomness of a pore space is to look at its pore neck size distribution plot. A completely organized specimen will have a defined sharp peak at the pore neck size, while a maximum randomized specimen will have an even size distribution over many pore neck sizes. In between we may obtain a gaussian distribution.

This can be visualized by comparing figures 2.3 and 2.4, which shows that the nearest neighbor distances are all the same in a completely organized material, while the distribution of nearest neighbor distances in a more random environment goes over a range of lengths. For a large sample it would probably be a gaussian distribution. By counting the surrounding neighbor distances for each particle and account for double counting, a pore neck distribution can be approximated [1].

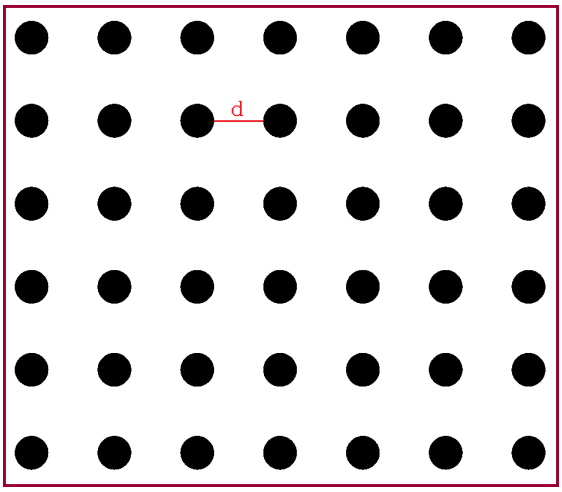

Figure 2.3: As an analog to the distribution of pore neck widths, the distribution of nearest neighbor distances can be an indicator of organization. Here, the material is completely organized with the same nearest neighbor distances d. This results in no size distribution, indicating complete organization in space.

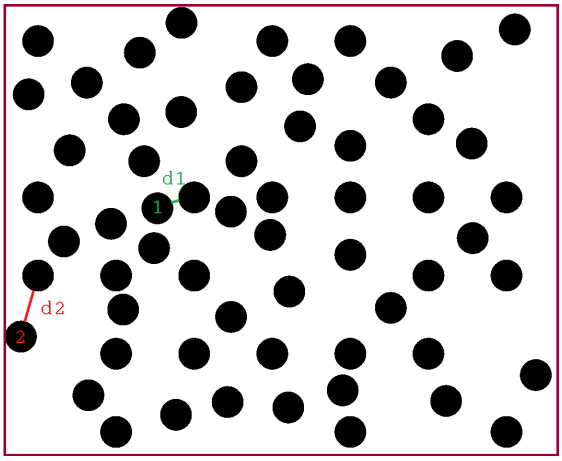

Figure 2.4: As an analog to the distribution of pore neck widths, the distribution of nearest neighbor distances can be an indicator of organization. Here, the material is random with various nearest neighbor distances d_i. This results in a range of the size distribution, indicating less organization in space.

Permeability

The permeability k of a material describes its ability to transport fluid, or in other words a factor of how easy fluid flows through it. Permeability is a characteristic quantity of a material and has units of area, m^2. In oil industry the unit darcy is used for permeability, where 1 darcy = $9.87 \cdot 10^{-9} cm^2 \approx 1 \mu m^2$ [2].

Length scales

There are two length scales to consider when it comes to porous media. One is the *specimen size* and the other is the *pore size*.

The specimen size scale is used when macroscopic quantities is investigated such as permeability or saturation. Typical specimen sizes are in the order of 10^{-2}m or more. A specimen is always considered to include more than one pore such that the specimen length goes over a number of pore lengths [2].

The pore size scale is used when explaining behavior and effects on the smallest scale in the specimen, the typical pore neck width. Typical pore neck widths are in the order of 10^{-3}m or less.

2.1.2 Parameters and properties of fluids

A fluid is a substance that are able to flow and change shape in the presence of external forces. A fluid may flow through tubes, fill containers, mix or not mix with other fluids, be deformed, etc. Therefore the term fluid includes not only all liquids but also all gases. As we know from everyday experience, different fluids have different properties; water is fairly easy to stir and pour out of a glass, while honey requires more force to be set in motion, and most of the time, air is a fluid in our environment we barely notice. The example above is only a difference in one of the many characteristic properties of fluids. Basic parameters and fluid properties will be introduced and explained in this section.

Density

As for any substance, the density ρ of a fluid is defined as mass per volume, usually with units [g/cm^3], and is given by [3]

$$\rho = \frac{m}{V}. \tag{2.4}$$

Equation (2.4) is useful if we want to know the density of a fluid when we know its volume and mass. We can also note that substances with higher density than a given fluid will generally sink to the bottom of it, and substances with lower density than that fluid will float on top of it.

Viscosity

All natural fluids have an internal resistance to move [3]. This resistance is the viscosity μ of a fluid. Viscosity is a property we can see on a fluid as how thick it is, and the thicker it is the more viscous it is. As an example, oil is more viscous than water, and we know that it requires more effort to set oil in motion than water.

There are two different quantities used to describe viscosity: *Dynamic* viscosity and *kinematic* viscosity.

Dynamic viscosity is just the long name for the viscosity of a fluid, and has units of pressure seconds, [Pa·s] [2].

The kinematic viscosiy ν of a fluid is its dynamic viscosity divided by its density [2],

$$\nu = \frac{\mu}{\rho}. \tag{2.5}$$

Kinematic viscosity has units of area per second, usually [mm^2/s]. This parameter is more useful in some calculations because different fluids with different viscosities and densities may have the same kinematic viscosity, which gives them equal flow behavior.

Surface tension

The interface of a fluid is the boundary between the fluid and a solid, or to some other fluid with which it cannot mix. A free surface of a fluid is the interface between two imiscible fluids.

Paperclips can be placed on water surfaces without sinking even though they have higher densities than water. The force supporting the paperclip and preventing it from sinking is the force of surface tension of the water. The surface tension γ of a fluid surface is a property enabling it to withstand some external force.

Surface tension arises from the cohesive forces between molecules in a fluid [3]. The cohesive interaction means that the equal molecules of the fluid attract eachother. In the bulk of the fluid the net cohesion force on molecules is zero, as they are attracted equally in all directions. On the surface the molecules experience a net cohesion force directed into the fluid, simply because there are no attractive forces outside of the surface. This is illustrated in figure 2.5. As the outer surface molecules are pulled towards the interior of the fluid an internal pressure builds up, and the fluid will reach a minimum volume when these forces neutralize eachother, e.g. water droplets are spherical.

At the minimum volume where the cohesive forces on the surface molecules are neutralized by the forces from the internal pressure of the fluid, the surface molecules are in a steady equilibrium. So to move the stable surface molecules or deform the surface, we have to do work. A relation for the surface tension can be deduced from this [1]:

$$\gamma = \frac{dW}{dA}, \tag{2.6}$$

which is the work necessary per change of surface area. Surface tension has units of energy per area J/m^2, or force per length N/m.

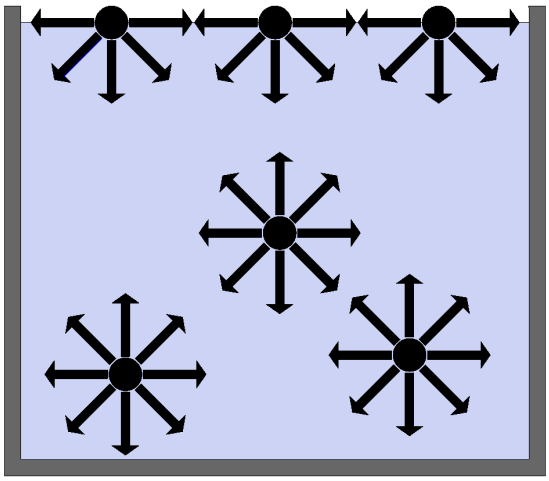

Figure 2.5: The molecules of a fluid experience attractive cohesive forces between eachother. This fluid is in an open container and has a free surface, so the net force on the molecules is dependent on position: The forces neutralize eachother in the bulk, while at the surface they constitute a net inward force on the surface molecules.

Wettability

Wettability is the tendency of a fluid to smear out on a smooth solid surface. A fluid can be classified as either wetting or non-wetting, determined by its angle of contact θ with a smooth solid surface. The contact angle is measured around the triple point of contact between a fluid, an atmosphere and a solid, starting from the solid surface inside the fluid and ending at the fluid surface to the atmosphere as in figure 2.6 [2]. The contact angle may have the values $0° \leq \theta \leq 180°$, see fig. 2.6.

A perfect wetting fluid has the contact angle $\theta = 0°$. Wetting fluids have the contact angles $0° < \theta \leq 90°$, and non-wetting fluids have the contact angles $90° < \theta < 180°$. A perfect non-wetting fluid has the contact angle $\theta = 180°$.

The wetting property of a fluid arises from a combination of the internal cohesive forces of the fluid, favoring non-wetting, and the adhesive forces between the fluid surface molecules and the solid surface molecules, favoring wetting [2]. The wettability of a fluid also depends on the same properties of the atmosphere.

Capillary action

For fluids with a surface of macroscopic length scale, the surface looks flat at equilibrium. However, if we look at the edges of such surfaces at small enough length scales, we see that the surface curves as illustrated in fig. 2.7. This curving is due to the effects of wettability of the liquid and atmosphere to the solid they are in contact with, i.e. the surface at the edge tends to the equilibrium contact angle between the given substances [2].

In the limit where the lenght scale of the surface of a liquid is similar to the length scale of the wetting effects, a phenomenon called *capillary action* occurs [2]. Tubes with inner diameter on

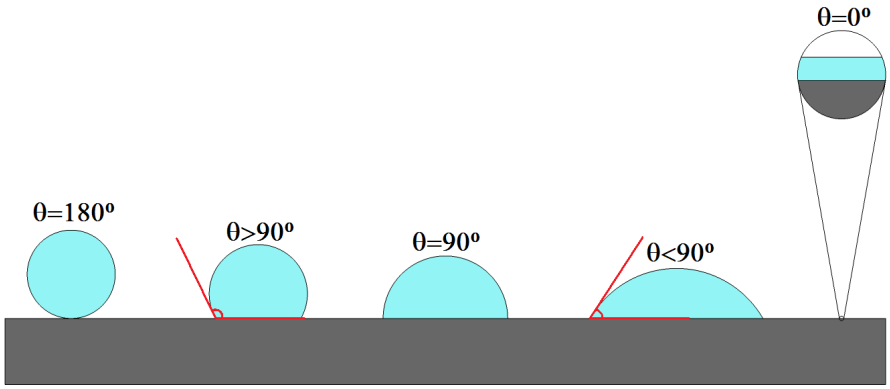

Figure 2.6: Fluids with different contact angles on a smooth solid surface. From left to right, the wetting properties of the droplets goes from perfect non-wetting to perfect wetting. The contact angle is measured as indicated by the red angles.

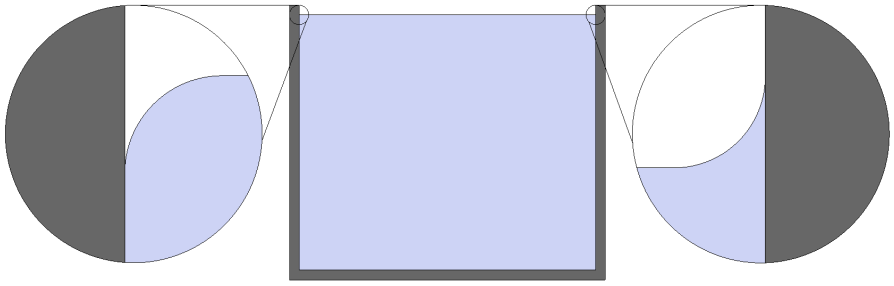

Figure 2.7: This container is large enough for the fluid to form a stable "flat" surface as to maintain a minimum surface area. At small enough length scales we see curved surfaces due to wetting: the blue fluid is non-wetting on the left container wall, while it is wetting on the right container wall.

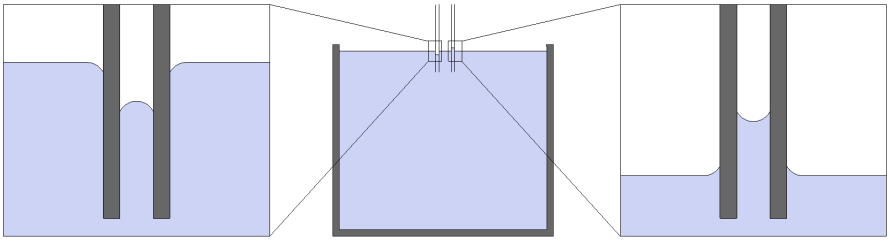

Figure 2.8: Two capillaries are lowered vertically into a fluid. Capillary action of the fluid occurs in the capillaries: The fluid is non-wetting in the left capillary, causing it to be pushed down the repulsing tube walls. The fluid is wetting in the right capillary, causing it to rise due to the attraction of the tube walls. Capillary action stops when the capillary forces are neuralized by e.g. internal fluid pressure or the force of gravity.

a scale of $I.D \leq 10^{-3}$m are called capillaries and gives the phenomenon a name. Figure 2.8 illustrates the principles of capillary action where open capillaries are vertically and partially immersed in a fluid. Capillary action depends on surface tension, wettability and fluid pressure [2].

Compressibility

Fluids can be classified as compressible or incompressible. Whether a fluid is considered compressible or incompressible is important in flow problems.

Compressibility κ is a measure of the relative change in volume of a specimen as a response to a uniform pressure change on its surface [3]. It is given by

$$\kappa = -\frac{1}{V}\frac{\partial V}{\partial p}, \tag{2.7}$$

where V is the volume of the specimen and p is the pressure.

Compressibility has units of area per force m^2/N, or inverse pressure Pa^{-1}.

Gases are considered compressible, while most liquids can be considered incompressible. Generally, at a given pressure change a fluid is considered incompressible if the compressibility is negligible, or compressible if the compressibility is significant. We should note that all fluids are compressible at a sufficient pressure change.

Internal pressure

In a steady state, the pressure p in an incompressible fluid, i.e. the pressure inside its surface, is the same everywhere. Since the pressure in the fluid is uniform, every surface element of the fluid surface experience the same amount of pressure from the fluid interior [3]. If the surface of an incompressible fluid experience a pressure change, this pressure is quickly redistributed evenly throughout the fluid.

2.1.3 Parameters of flow

Flow is the motion and behavior of fluids under the influence of external forces. There are different regimes of flow, which means that fluids may flow at various velocities and behave differently, given different conditions. Flowing fluids are often given a flow rate, a flow velocity and their flow regime is characterized.

Volume flow and volume flux

The volume flow rate Q of a fluid is a measure of the rate of its flow in terms of volume per second [2], [m^3/s]. As an example, if we use 10 seconds to fill a $10^{-3}m^3$ tank with water, the average volume flow rate of the water is $Q = 10^{-4}m^3/s$ (corresponding to 1dl per second).

The volume flux v of a fluid can be considered as the velocity of the average flow front needed to satisfy

$$v = Q/A, \tag{2.8}$$

where A is the cross section of the fluid perpendicular to the flow direction [2].

The volume flux is also called the *Darcy velocity*. This flow parameter is useful when investigating macroscopic properties of fluid flow.

Reynolds number

There are two main regimes of flow: *laminar* flow and *turbulent* flow.

Laminar flow is characterized as when a fluid flows in thin layers that slide against eachother with different velocities. This is a stable form of flow and is due to low flow velocities with respect to viscous forces in the fluid. Lava flowing around a rock is an example of a fluid with laminar flow [2].

Turbulent flow is characterized by chaotic behavior. This is an unstable form of flow because it is inviscid, which means the fluid has low or even neglectable viscosity compared to the flow velocity. Smoke from an extinguished candle is an example of a fluid with turbulent flow [2].

The Reynolds number Re is a dimensionless number used in characterizing flow into either of these two regimes. It is defined as [2]

$$Re = \frac{vl}{\nu}, \tag{2.9}$$

where v is the darcy velocity, ν is the kinematic viscosity and l is any length of relevance, like the length of an object diverting the flow or the width of a pipe. Low Reynolds numbers $Re \ll 1$ indicates laminar flow as viscous forces dominates. High Reynolds numbers $Re \gg 1$ indicates turbulent flow as viscosity can usually be neglected.

2.2 Phenomenological laws and flow equations

There are a number of equations available to solve flow problems. In some cases phenomenological descriptions are sufficient to explain or predict flow behavior, while for other cases differential equations have to be used on a microscopic level. Either way, these equations are important tools in the understanding of fluid flow behavior.

2.2.1 Young-Laplace equation

When the surrface between two imiscible fluids is curved, the surface tension leads to a pressure difference between the two fluids in contact.

The pressure on the concave side exeeds the pressure on the convex side by Δp, given by the Young-Laplace equation [2]

$$\Delta p = \gamma \left(\frac{1}{R_1} + \frac{1}{R_2} \right), \tag{2.10}$$

where γ is the surface tension between the two fluids, R_1 and R_2 are the principal radii of curvature of the interface.

2.2.2 Fluid equations of motion

The derivation of equations of motion for fluids [2] concludes that the rate of change of momentum density equals the force per unit volume,

$$\rho \frac{D\mathbf{u}}{Dt} = \rho \frac{\partial \mathbf{u}}{\partial t} + \rho \mathbf{u} \nabla \mathbf{u} = -\nabla p + \mathbf{f}_\mu + \mathbf{F}, \tag{2.11}$$

where $\mathbf{u}(\mathbf{r}, t)$ is local flow velocity, $\mathbf{f}_\mu$ is the viscous force and $\mathbf{F}$ is the external force. The continuity equation

$$\frac{\partial \rho}{\partial t} + \nabla \cdot \rho \mathbf{u} = 0 \tag{2.12}$$

states that $\nabla \cdot \mathbf{u} = 0$ for incompressible fluids, and simplifies eq. (2.11) to the Navier-Stokes equation

$$\rho \frac{D\mathbf{u}}{Dt} = -\nabla p + \mu \nabla^2 + \mathbf{F}, \tag{2.13}$$

for incompressible fluids. The dynamic flow equations describe the flow dynamics of fluids on a particle level, and require sufficient boundary conditions in order to obtain solutions to a flow problem. However, equation (2.11) serves to illustrate the forces that play into the flow of fluids, i.e. the pressure gradient, the viscous force and some external force.

The boundary conditions for flow in porous media is as complex as the geometry of the sample, so they will be hard to define precisely [1]. Instead of dynamical equations, some of the flow properties in porous media can be explained and characterized macroscopically.

2.2.3 Darcy's law

Darcy's law is a phenomenological law concerning the flow of a fluid through a porous media on the specimen scale. The law relates Darcy velocity to the permeability, viscosity and pressure gradient. It is defined as [2]

$$\mathbf{v} = -\frac{k}{\mu}(\nabla p - \rho \mathbf{g}), \tag{2.14}$$

where $|\mathbf{v}| = v$ is the Darcy velocity, k is permeability, μ is viscosity, ∇p is the pressure gradient and $\mathbf{g}$ is the acceleration of gravity, $-g$, perpendicular to the ground.

For horizontal flow of a fluid where gravity can be neglected, Darcy's law simplifies to

$$\mathbf{v} = -\frac{k}{\mu}\nabla p. \tag{2.15}$$

Note that horizontal flow is always in the opposite direction of a pressure gradient.

The continuity equation for porous media accounts for the fact that the fluid is excluded from the porous matrix [2],

$$\frac{\partial \phi \rho}{\partial t} + \nabla \cdot (\rho \mathbf{v}) = 0, \tag{2.16}$$

and written in terms of the Darcy velocity to express the volume flux per unit area and time. This continuity relation is based on average macroscopic quantities and is only valid on a specimen scale.

Combining equations (2.15) and (2.16) for horizontal flow of an incompressible fluid in a porous media, we get the Laplace equation for the pressure [4]

$$\nabla^2 p = 0. \tag{2.17}$$

2.3 Two-phase flow basics

2.3.1 Fluid displacement and fingering

Two phase flow in porous media obviously involves two fluids, where one is called the *defending fluid* and the other is called the *invading fluid* [1]. Initially, the defending fluid is completely saturating the porous media sample until the invading fluid enters the sample and displaces it. The flow pattern and the final saturation of the invading fluid both depend on the *fingering regime* [1]. The different fingering regimes in porous media can be explained by the dominating forces involved in the flow of the invading fluid.

There are two kinds of fluid displacement processes in porous media [1]:

1. The invading fluid is non-wetting and the defending fluid is wetting. This process is called *drainage*.

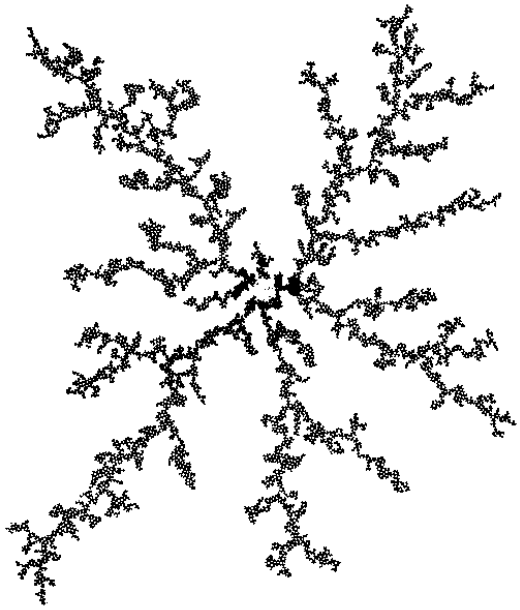

Figure 2.9: An intermediate viscous fingering pattern from an experiment where air (black) displaces an aqeous glycerol solution (white) in a two dimensional porous media.

2. The invading fluid is wetting and the defending fluid is non-wetting. This process is called *imbibition*.

Viscous fingering

The fingering regime of fluids invading with high Darcy velocity and where the viscosity of the invading fluid is much less than the viscosity of the defending fluid, $\mu_i \ll \mu_d$, is called *viscous fingering* [4]. The pattern of viscous fingers, fig. 2.9, is a result of the dominant viscous forces driving the flow, and can be explained qualitatively by Darcy's equation.

Assume a circular and horizontal 2 dimensional porous media sample saturated with a viscous defending fluid with viscosity μ_d. The porous media is situated in the ambient pressure p_0. The invading fluid is considered inviscid, $\mu_i \approx 0$, and is contained in a reservoir with pressure $p > p_0$. The reservoir containing the invading fluid is connected to the center of the circular porous media, and due to the viscosity of the defending fluid there is a pressure gradient between the reservoir and the outside of the porous media:

$$\nabla p = \frac{p_0 - p}{r}, \tag{2.18}$$

where r is the sample radius. Initially, the pressure gradient is equal along the radius in all angular directions and points towards the center.

According to eq. (2.15), the pressure gradients induce flow in the defending fluid directed radially outwards from the center of the porous media. Inherently, the invading fluid invades an area in

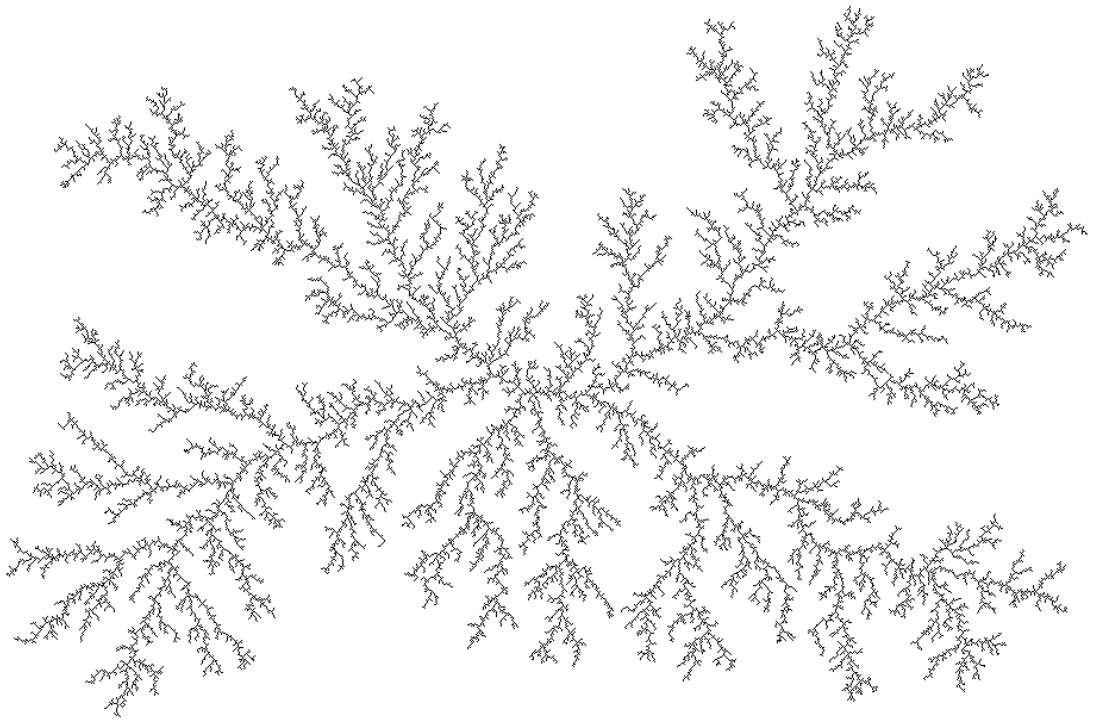

Figure 2.10: A Diffusion Limited Aggregation simulation of viscous fingering at breakthrough of a circular two dimensional porous media.

the central region of the porous media and the displacement front has now an arbitrary shape due to the pore distribution. This is the moment the displacement front becomes unstable and favors viscous fingering of the invading fluid: If we consider the shape of the displacement front a short time after the start of the invasion, we see that some points are closer to the surface of the sample than others. Considering that the pressure in the invading fluid is still p and uniform, we conclude that the pressure gradients are steeper at points closer to the surface than at points closer to the center. The pressure gradients can be written as

$$\nabla p = \frac{p_0 - p}{d_i}, \tag{2.19}$$

where d_i is the shortest distance from point i at the displacement front to the surface (rim) of the porous media.

Combining this with Darcy's equation, we find that the displacement of defending fluid and thus the invasion of invading fluid is favored at the tips of the finger pattern. Fingers created at an early stage grows fastest due to their increasing length compared to the other growing fingers, and therefore has steeper pressure gradients with respect to the other fingers. The characteristics of the pattern is long invasion fingers with few or none trapped clusters [4].

The viscous fingering regime can be simulated with the *DLA* algorithm listed in appendix A.1, and a result is shown in 2.10.

Capillary fingering

Drainage processes with very low flow rate of the invading fluid, such that the Darcy velocity of the flow is $v \sim 0$ on a specimen size scale, are in the *capillary fingering* regime [1]. The flow of the capillary fingering regime can not be explained on the specimen scale due to the very low flow rate, and hence $\nabla p \sim 0$. However, where we can neglect the forces of gravity, the flow can be explained qualitatively on the pore size scale with the help of the Young-Laplace equation, eq. (2.10).

As before, assume a circular and horizontal two dimensional porous media sample saturated with a viscous defending fluid with viscosity μ_d. The porous media is situated in the ambient pressure p_0. The invading fluid is considered inviscid, $\mu_i \approx 0$, and is constantly flowing into the center of the porous media with a very low volume flow rate Q_0 such that the pressure gradients over the sample can be neglected. Slowly, a cluster of the invading fluid is formed at the center of the porous media.

The displacement front, or the interface between the invading and defending fluids, experience the same pressure everywhere given by

$$p_{cap} = p_{nw} - p_w. \tag{2.20}$$

p_{cap} is the capillary pressure, and is defined as the pressure difference $p_{nw} - p_w$ between the non-wetting and wetting fluids in the drainage process [2].

According to the uniform pressure p_{cap} and eq. (2.10), the curvature of the fluid interface menisci in all pore necks will satisfy

$$p_{cap} = \gamma \left(\frac{1}{R_1} + \frac{1}{R_2} \right). \tag{2.21}$$

The volume flow rate Q_0 implies that the pressure p_{nw} of the invading fluid slowly increases, and leads to increasing capillary pressure due to eq. (2.20). This is a stable situation where the curvature of the interface menisci increases [1], until the capillary pressure exceeds a critical value p_c, given by the pore neck geometry at the displacement front as

$$p_c = \gamma \left(\frac{1}{R_{1,min}} + \frac{1}{R_{2,min}} \right) = \gamma \left(\frac{2}{b} + \frac{2}{l_{max}} \right). \tag{2.22}$$

Here, b is the plate separation and l_{max} is the width of the widest pore neck at the front. The barrier pressure p_c is therefore the pressure where the curvature of the interface meniscus in the largest pore neck is at its maximum. Whenever $p_{cap} > p_c$, the meniscus in the largest pore neck at the displacement front becomes unstable, and the pore that follows it is spontaneously invaded [1].

After each such invasion, the displacement front is presented to a new set of pore necks and two possibilities arise:

1. The new pore neck geometry at the displacement front is still such that $p_{cap} > p_c$, and another invasion occurs.

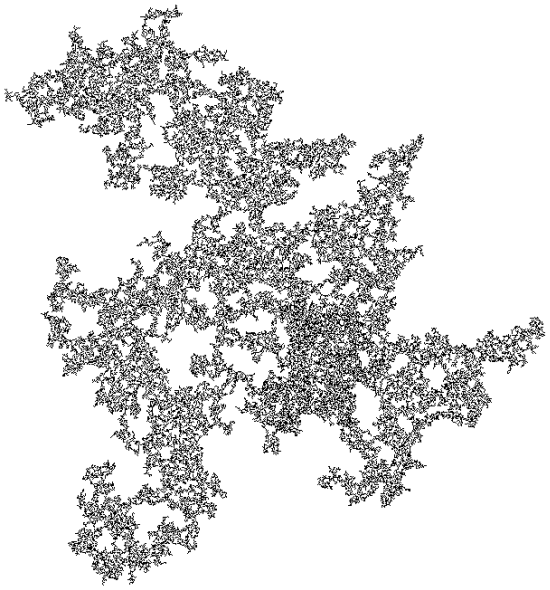

Figure 2.11: An Invasion Percolation simulation of capillary fingering at breakthrough of a circular two dimensional porous media.

2. The new pore neck geometry at the displacement front is such that $p_{cap} < p_c$, and the capillary pressure has to build up to overcome the new barrier pressure for another invasion to occur.

In a porous media with a random pore neck size distribution, this process creates a pattern with dense invasion clusters and many trapped clusters of defending fluid as in fig. 2.11. The place where the invading fluid breaks through is random, and given by the "easiest way out" in terms of the capillary barriers.

The process can be simulated with the *IP* algorithm listed in appendix A.2. Figure 2.11 shows a capillary fingering structure simulated with *IP*.

In imbibition processes similar to the example above, the exact opposite happens on the pore scale [1]. At the displacement front, the pressure of surface tension has to exceed the capillary pressure to induce an invasion. With respect to the invading fluid pressure, the capillary pressure must be lower than a critical value, $p_{cap} < p_{c'}$. It causes the non-wetting defending fluid to spontaneously retract into the next pore and at the same time "suck" the invading fluid along with it.

From eq. (2.20) we see that the capillary pressure is decreased when the wetting fluid pressure p_w is increased. As the wetting fluid pressure builds up, the capillary pressure p_{cap} decreases and the defending fluid is displaced into the widest part of the surrounding pores. Considering that the fluids have uniform pressure, we see that the smallest pore at the displacement front will give the highest $p_{c'}$ because the curvature of the meniscus there is smallest. Whenever $p_{cap} < p_{c'}$, the fluid interface in the smallest pore at the displacement front becomes unstable and the invading fluid invades the following pore necks.

After each such invasion, the displacement front is presented to a new set of pores and two possibilities arises:

1. The new pore geometry at the displacement front is still such that $p_{cap} < p_{c'}$, and another invasion occurs.
2. The new pore geometry at the displacement front is such that $p_{cap} > p_{c'}$, and the capillary pressure has to decrease to a lower value than the new critical pressure before another invasion occurs.

As we can imagine, the capillary fingering pattern will look a lot similar in an imbibition process as in a drainage process.

Stable displacement

Sometimes, two phase flow in porous media has a stable displacement front leading to the total saturation of the invading fluid. The stable displacement usually means that the least advanced portions of the displacement front is favored to advance over the most advanced portions.

Consider the viscous fingering example with the defending and invading fluids interchanged such that the viscous fluid displaces the inviscid. Now, the pressure gradients are steepest at the points of the displacement front closest to the center of injection. The least developed parts of the displacement front is favored to invade due to the pressure gradients and there will be a stable circular displacement front rather than fingers, as seen in fig. 2.12.

Another stable two phase flow displacement is an imbibition process where a viscous fluid invades an inclined two dimensional porous media sample with an inviscid defending fluid. The sides of the sample are sealed, except for a small opening at the top of the "hill", and the invading fluid flows in and displaces the defending fluid from the bottom of the sample. The gravity component against the flow direction will stabilize the displacement front: The hydrostatic pressure of the wetting fluid decreases the capillary pressure p_{cap} at points on the displacement front that is lower in altitude than others, and thus favors invasion at lower points whenever there are any. The result is a straight and level displacement front as in fig. 2.13.

Capillary fracturing

Capillary fracturing occurs in two phase flow in deformable porous media when the capillary forces overcome the frictional forces of the particles. The particles are pushed by the capillary forces at the displacement front to induce the opening of conduits or cracks in the flow direction [5]. The invasion front "plows" the particles, and eases the flow of the fluids. An image of capillary fracturing can be seen in figure 2.14.

2.3.2 Useful dimensionless ratios

Capillary number

The capillary number Ca is a measure of the ratio of viscous forces to capillary forces involved in the two phase flow. It is defined as [2]

$$Ca = \frac{v \cdot \mu}{\gamma}, \tag{2.23}$$

Figure 2.12: A stable viscous displacement of air (white) by a viscous liquid (black) in a deformable two dimensional porous media. Note that the displacement front is still within the porous media which is invisible while saturated with air.

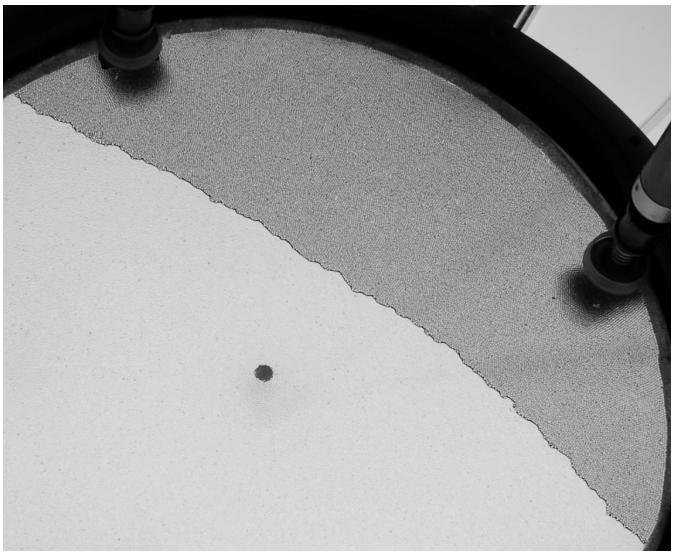

Figure 2.13: A stable imbibition displacement of air (white) by a viscous liquid (black) in a deformable two dimensional porous media. The wetting fluid flows into the sample from the top right corner while the sample inclines uphill towards the lower left corner, this results in a stable displacement front.

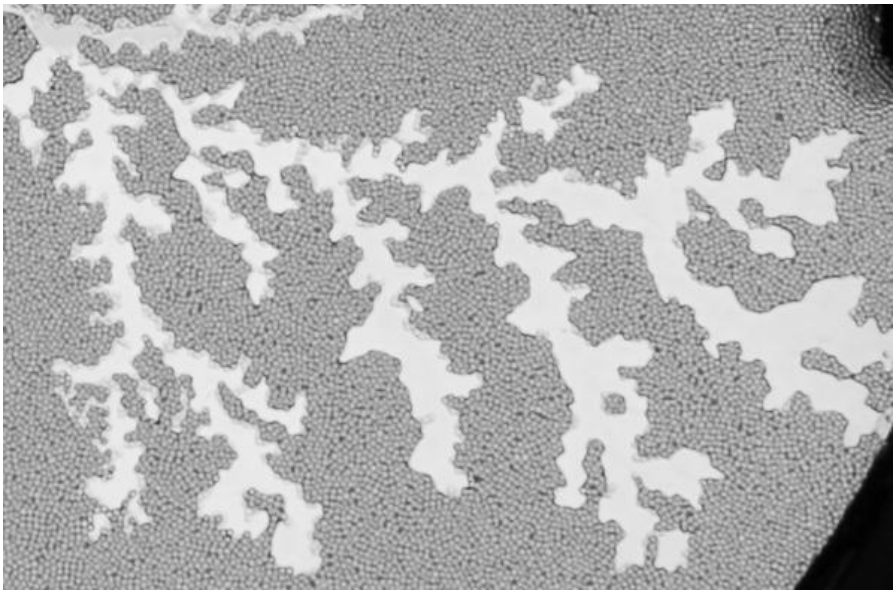

Figure 2.14: Capillary fracturing in a two phase flow displacement of glycerol (black) by air (white) in a deformable two dimensional porous media. The resulting fingers are much thicker than the average pore size. Pores can be spotted as small black clusters.

where v is the darcy velocity, μ is the dynamic viscosity of the wetting fluid and γ is the surface tension between the fluids. Ca is a dimensionless number.

Low capillary numbers $Ca \ll 1$ indicate domination of capillary forces and that capillary fingering occurs, while high capillary numbers $Ca \sim 1$ indicate the domination of viscous forces and that viscous fingering occurs.

Bond number

In a similar fashion as the capillary number, the bond number Bo is a measure of the ratio of gravitational pressure to capillary pressure over characteristic pores. It is defined by [1]

$$Bo = \frac{\Delta\rho g a^2}{\gamma}, \tag{2.24}$$

where $\Delta\rho = \rho_w - \rho_{nw} \approx \rho_w$ is the density difference between the wetting and non-wetting fluids, g is the gravity component in the direction of the flow, a is the typical pore size and γ is the surface tension between the fluids.

For a horizontal flow $Bo = 0$, while for a vertical flow Bo may be high. This means small bond numbers indicate domination of capillary forces, while high bond numbers indicate domination of gravitational forces.

2.4 Fractals and fractal dimension

2.4.1 Fractals

A fractal is a construction which is built up by parts that look like the whole in some way [6]. This is feature which makes fractals scale invariant and self similar at all scales. Simple fractals which satisfies this description can be generated using an *initiator* and a *generator* [6]. Simply put, the action of the generator when iterated once is to divide the initiator into smaller but similar pieces of initiators, usually in an arranged fashion. In every subsequent iteration, the generator divides the smaller initiators into even smaller but similar initiators, and arranges them in the same fashion every time. The initiator is referred to as the 0th generation and the generator can be seen as the 1st generation. This is somewhat difficult to visualize without examples, so we take a look at the triadic Koch curve and the triangular Sierpinsky gasket [6].

The triadic Koch curve is generated with the unit line segment as the initiator and the curve shown as the first generation in figure 2.15 as the generator.

The fifth generation triadic Koch curve in fig. 2.15 clearly shows the properties of self similarity and scale invariance, although this is only really true after infinite iterations.

The other example, the trianglar Sierpinsky gasket, has a filled equilateral triangle as the initiator. Shown as the first generation in figure 2.16, the generator removes a region of the initiator formed as a triangle with its corners centered at each side of the initiator.

The fifth generation of the triangular Sierpinsky gasket in fig. 2.16 also shows the properties stated to fractals. Note how these (prefractal) examples consists of different sized parts that look

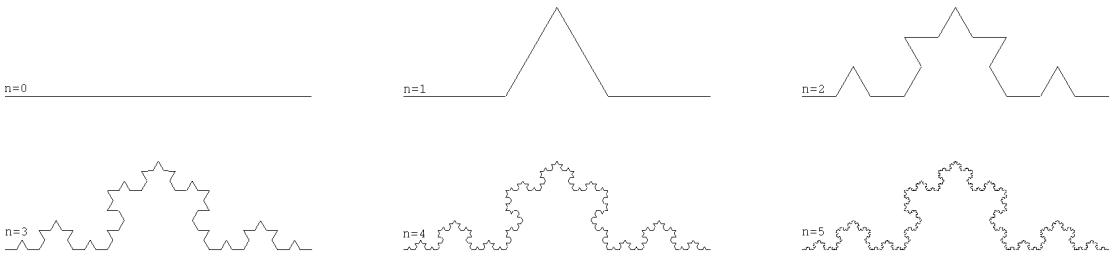

Figure 2.15: The first 5 generations of the triadic Koch curve including the initial 0th generation. The generation number is indicated by n.

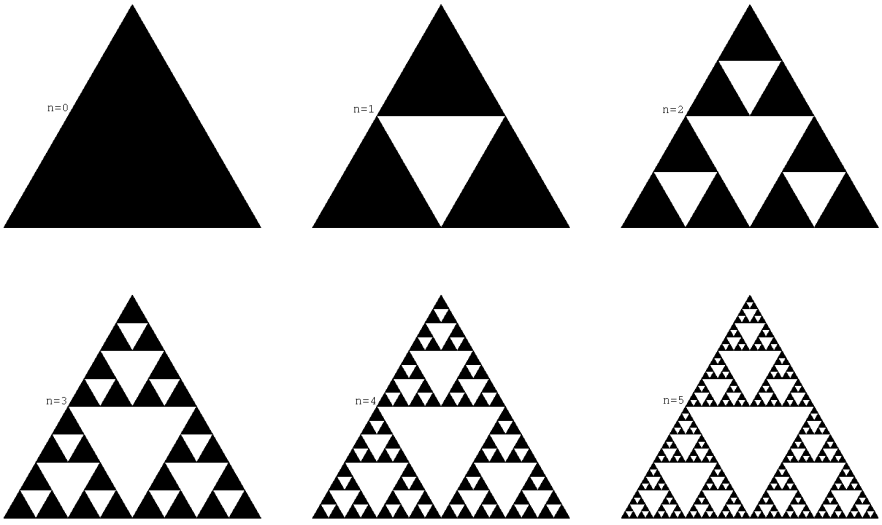

Figure 2.16: The first 5 generations of the triangular Sierpinsky gasket including the initial 0th generation. The generation number is indicated by n.

like the whole in some way. In their infinite generations (fractals), this property is seen on all size scales.

The generated examples above are rather simple and easy to construct. More complicated fractals can be obtained when the generator includes some rotation, mirroring, or some other affine transform [7].

Fractal dimension

Note how the fifth generation of the triadic Koch curve in fig. 2.15 seems to have a thicker line than the third generation. By taking a closer look, we see that this is due to the "wiggling" of the curve and that it is still only a line which fills no area.

However, we see that the length of the fifth generation Koch curve must be a lot longer than the original unit line segment, even though they extend equal lengths in space from left to right. Further, it can be proved that the length of the nth generation Koch curve $\to \infty$ when $n \to \infty$, and that the area of the Koch curve for any n is always 0 [7]. The same phenomena can be observed if we sum the circumferences of the triangles in the fifth generation Sierpinsky gasket and compare the sum with the circumference of the initial triangle.

At first it is surprising and confusing to read about a curve of infinite length and zero area, which at the same time is confined to an area of less than a unit square! This phenomena can luckily be explained in a comprehensive way in terms of topological dimensions ($D_T = 1, 2, 3$), and will also introduce the notion of dimension to fractal structures [6].

Imagine these two situations:

1. We attempt to measure an area ($D_T = 2$) by covering it with an infinetely thin line ($D_T = 1$) and then measure the length of the line.
2. We attempt to describe the size of an infinetely thin line segment ($D_T = 1$) by the area ($D_T = 2$) it occupies.

The length we find in the first scenario is infinite and the area we find in the second scenario is zero.

This illustrates that if we measure the size of an E dimensional structure with an infinitesimal $D_T < E$ dimensional "yardstick" we end up with an infinite value, and if we measure the size of an E dimensional structure with an infinitesimal $D_T > E$ dimensional "yardstick" we end up with zero [6]. On the other hand, if we measure the size of an E dimensional structure with an infinitesimal $D_T = E$ dimensional "yardstick", we get an exact finite result.

The example above is similar to the problem we have for the nth generation Koch curve, only that there is no topological dimension between 1 and 2 for which we gan get a finite length.

The *fractal dimension* D is introduced to accomodate this problem [6]. The fractal dimension can have all values $D \in (0, 3)$ and tells us in what dimension a fractal measure may have a finite value. A measure is said to be fractal if its fractal dimension strictly exceeds its topological dimension, $D < D_T$.

Then, for the nth generation triadic Koch curve, the fractal dimension of its length measure has to be $1 < D < 2$. The value is found to be $D \approx 1.26$ [6], confirming the simple description of fractal dimension.

Similar results have been found for *fractal surfaces* with $D \in (2, 3)$ and *fractal dust* with $D \in (0, 1)$ [6]. Also, other measures than length can be fractal and assigned a fractal dimension [7]. The most general description of a fractal dimension is that it is the scaling exponent of a scale invariant relationship, and once the fractal dimension is known for a measure, it can describe the measure on all scales. Methods of obtaining the dimension of a fractal structure are discussed in section 2.4.2.

Note that the calculation of the actual measure is another and more complicated problem [6], but the fractal dimension gives us a qualitative description of e.g. how the observable details of a curve scales with the scale length it is observed at.

Fractals observed in nature

Many natural processes results in fractal structures. Coastlines, rivers, mountains, lightning and two phase flow patterns in porous media are a few examples of the many fractals occuring in nature. Some important differences between natural and generated fractals should be noted [7]:

1. The self similarity and scale invariance properties is approximate or statistical.
2. The self similarity and scale invariance properties are valid over a limited range of scales only.

To understand the first point we must consider that many different forces are involved in forming natural fractals, while the generated fractals are given by a single repeated action. This adds an element of randomness to natural fractals. The second point is explained by the fact that the forces responsible of forming the fractal structure are effective over a limited range of distances. As an example, the forces creating a river path and its branches is not creating similar patterns at an atom scale. Figure 2.17 shows an example of a natural fractal created by two phase flow in a non-deformable porous media. Many plants has fractal structure as the fern shown in 2.18.

2.4.2 Methods to find fractal dimension

There are a number of ways to find various fractal dimensions of fractal structures [7], while only two of them will be described here. Those two are the *box counting dimension* and the *mass dimension*.

Box counting dimension

Remember the problem in section 2.4.1 where we attempted to measure the size of the triadic Koch curve. Let the measure be referred to as M_d, which in this case is the length measure of the triadic Koch curve in dimension d. The goal of the box counting method is to determine the fractal dimension D, which is the best method to describe the measure of a fractal.

The measure of size in dimension d can be defined as [6]

$$M_d = \sum \delta^d = N(\delta) \cdot \delta^d, \tag{2.25}$$

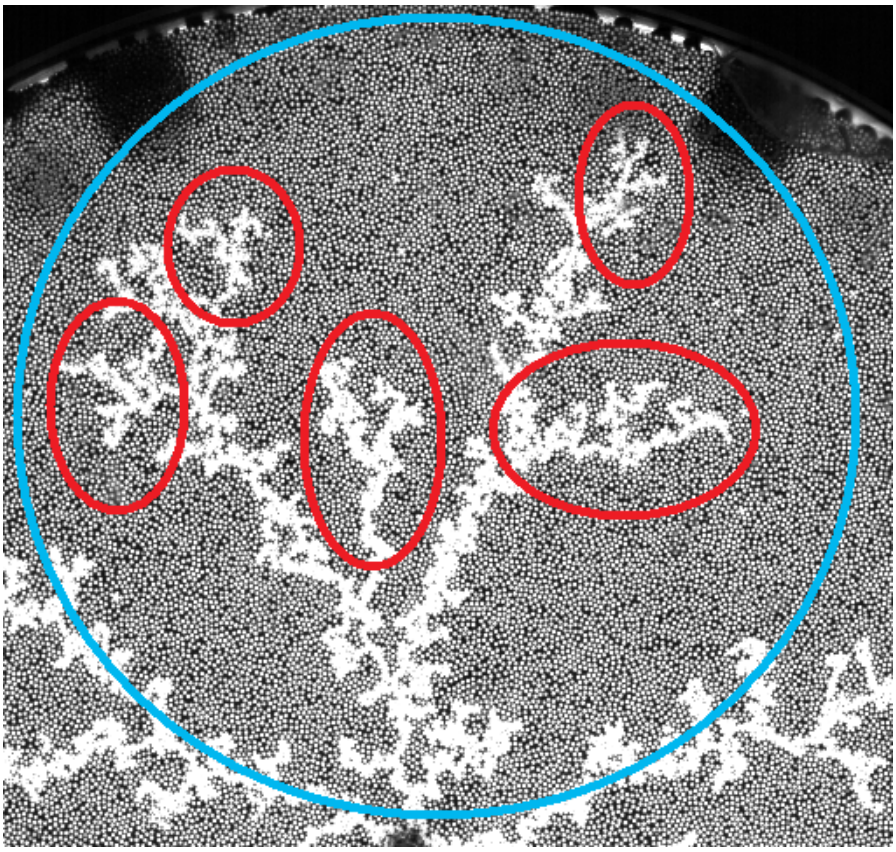

Figure 2.17: A part of a fractal viscous fingering pattern where air (white) invades glycerol (black). The initial branch inside the blue ring has split into two new branches. The two new branches develops brances with branches on them, some indicated by the red rings. The self similarity and fractal nature of viscous fingering can be observed as the splitting of branches at many scales.

Figure 2.18: It is easy to see the self similarity of this fern. Look at the tiniest leaves of the fern: They are organized in a pattern that looks like a fern. These tiny "ferns" are organized on branches that look like small ferns. These fern looking branches are arranged on the stem of the fern in the familiar pattern.

which is in terms of the number $N(\delta)$ of d dimensional "yardsticks" δ^d of size δ needed to cover the set of points in the fractal. This is increasingly accurate for smaller δ, and as previously discussed

$$M_d \underset{\delta \to 0}{\longrightarrow} \begin{cases} 0, & d > D \\ \\ \infty, & d < D. \end{cases} \tag{2.26}$$

It follows from equations (2.25) and (2.26) that for $\delta \to 0$,

$$N(\delta) \sim \frac{1}{\delta^D}. \tag{2.27}$$

Therefore, the determination of the box counting dimension of a fractal is done as follows [6]:

1. The number of boxes $N(\delta)$ needed to cover the set of points is counted over a range of decreasing box sizes δ. The dimension d of the boxes should be the euclidean dimension containing the fractal, ensuring that $d \geq D$.
2. The box counting fractal dimension D is found as the negative of the slope of the resulting $N(\delta)$ plotted against δ in a log-log plot [BOXPLOT], i.e. as the absolute value of the first order coefficient in the linear equation

$$log(N(\delta)) = -D \cdot log(\delta) + log(a) \tag{2.28}$$

   which best fits the plot, where a is an arbitrary constant.

The box dimension of a fractal describes the increase of details observed as the observing scale is decreased.

Mass dimension

In nature, physical systems and experimental results have a characteristic smallest length scale such as the radius of an atom R_0 [6]. So to apply this fact to the discussed ideas of fractal dimension we define "yardsticks" in terms of monomers. A monomer can be thought of as a sphere of radius R_0, the smallest length unit in a system. Macroscopic clusters of different topological dimensions can be described by such monomers as follows [6]:

A line can be thought of as a chain of monomers. A line of length $L = 2R$ (the length scale R of the line is measured from its center) can be represented in terms of the integer number N of monomers of size R_0,

$$N = (R/R_0)^1. \tag{2.29}$$

A 2 dimensional cluster can be seen as a flat collection of monomers, e.g a cluster of monomers that form a circular disc of radius R gives

$$N = \rho(R/R_0)^2, \tag{2.30}$$

where $\rho = \pi/2\sqrt{3}$ is the number density of close packed spheres on a plane. Similarly, a 3 dimensional cluster can be described as a collection of monomers, e.g. the number of monomers in a sphere of radius R is

$$N = \rho(R/R_0)^3, \tag{2.31}$$

where $\rho = \pi/3\sqrt{2}$ is the number density of close packed spheres in three dimensions.

These relations can only be applied in the limit $R \gg R_0$ where the monomers will make a smooth approximation of the cluster shape, as $N \to \infty$. In this asymptotic limit, we can write the relationship between the number of monomers N and the cluster size measured in terms of the radius R of the smallest circle that contains the entire cluster as

$$N = \rho(R/R_0)^D. \tag{2.32}$$

Eq. (2.32) is called the *number-radius* relation where D is the cluster dimension. Since the mass of each monomer is the same, N can be considered the mass of the cluster and ρ can be considered the mass density. The cluster dimension D is therefore often called the *mass dimension.*

For fractal clusters, the mass dimension equals their fractal dimension. Hence the number-radius relation can be used to find the fractal dimension of clusters [6].

A fractal cluster has the property that its density decreases as its radius increases in a way described by the exponent D (mass dimension) in eq. (2.32). In other words, a cluster is not fractal if its density is constant for increasing radii.

The mass dimension of a fractal gives a quantitative description of how it fills space for increasing radii, however it does not give any information about the shape of the fractal cluster.

Number-radius relation for two phase flow in circular porous media

In the processed images of experimental data, the air clusters are seen as collections of "filled pixels". The filled pixels have value 1 and are the white pixels, while the empty pixels are black and have value 0. Therefore, each filled pixel can be counted as a unit mass "monomer" centered at its pixel coordinates $\mathbf{p_i} = (x_i, y_i)$. The pixel at the center of injection $\mathbf{c} = (x_c, y_c)$ is chosen as the center of the cluster. This enables us to associate each filled pixel with a distance from the center of the cluster as

$$r_i = |\mathbf{p_i} - \mathbf{c}| = \sqrt{(x_i - x_c)^2 + (y_i - y_c)^2}. \tag{2.33}$$

The number-radius relation gives the number of filled pixels with pixel coordinates within a circle of radius r from the center of injection [6],

$$N(r) = N(r_i < r). \tag{2.34}$$

Since the experimental cluster has a finite size, there must exist a circle of radius r_{max} which contains all the N_0 filled pixels of the cluster. For $r > r_{max}$ the number-radius relation will become constant as $N(r > r_{max}) = N_0$. This must be considered in an attempt of determining the mass dimension of the cluster.

By introducing the gyration radius R_g of a cluster, the number-radius relation can be normalized to fit two phase flow clusters of different r_{max} sizes [6]. The radius of gyration is an alternate measure of the cluster size r_{max}, and is given by [6]

$$R_g = \sqrt{\frac{1}{N_0}\sum_i r_i^2}. \tag{2.35}$$

The radius of gyration is the root mean square distance of filled pixels from the center of injection.

When a log-log plot of $N(r)/N_0$ is plotted against r/R_g, the graph clearly shows a number-radius relation of the form [6]

$$N(r) = N_0 \left(\frac{r}{R_g}\right)^D f(r/R_g). \tag{2.36}$$

The function $f(r/R_g)$ accounts for the finite size of the cluster as

$$f(r/R_g) = \begin{cases} \text{constant}, & r/R_g < 1 \\ (r/R_g)^{-D}, & r/R_g \gg 1, \end{cases} \tag{2.37}$$

where the crossover point $r/R_g = 1$ can be seen as where the curve flattens as $N(r) \to N_0$.

The mass dimension D of the cluster is best found from equation (2.36) in the limit $r_{min}/R_g < r/R_g < 1$, where r_{min} is a limit due to the finite pixel size.

2.5 Multifractal measures

Consider a *population* of a quantity distributed over a volume of linear size L^E, called a geometric *support* [6]. The population may be any quantity that can be distributed over a support, such as the human population on the face of the earth or probabilities on a line segment. The description of a distribution tends to be similar whatever the linear scale L is.

Multifractal measures relates to the study of a population distributed on a support. Here, the distribution has fractal properties and the support can be a line, plane, volume or a fractal structure itself [6]. Multifractal measures builds on the idea that a fractal measure may be represented by a set of intertwined fractal subsets with different scaling exponents. The basic ideas of multifractal measures can be illustrated with some examples of iterative processes.

Curdling

Curdling is a process where an initially uniform distribution is clumped together to singularities with dense values. A form of a triadic Cantor set, fig. 2.19, can be used as an example of curdling [6]:

Assume that the initiator is a 1 dimensional bar of unit length $l_0 = 1$ and unit mass $\mu_0 = 1$. The initial density is therefore $\rho_0 = 1$. The generator process cuts the initiator into two equal

Figure 2.19: Sequence of generations of a triadic Cantor bar, where the initial bar (top) of length $l_0 = 1$ and mass $\mu_0 = 1$ is cut into two equal halves which are compressed to 1/3 of the initial bar length. The process is repeated for each generation. Since the total mass is conserved while the bar length decreases, the density of the bars increases as indicated by their height.

pieces of mass $\mu_1 = \mu_0/2$, and then compresses them so their lengths becomes $l_1 = l_0/3$. The new density is then $\rho_1 = \mu_1/l_1 = 3/2$.

If this process is repeated n times, we end up with $N = 2^n$ line segments of length $l_n = 3^{-n}$, mass $\mu_n = 2^{-n}$ and density $\rho_n = (3/2)^n$. Note that the initial mass μ_0 (population) is conserved,

$$\sum_{i=1}^{N} \mu_i = N \cdot \mu_n = 1, \tag{2.38}$$

while the combined length of the bar segments (support) decreases as

$$\sum_{i=1}^{N} l_i = N \cdot l_n = \left(\frac{2}{3}\right)^n. \tag{2.39}$$

Generally, the mass μ_i of the i-th line segment is found to be scaling with the length l_i as

$$\mu_i = l_i^{\alpha}, \tag{2.40}$$

where $\alpha = log(2)/log(3)$ is the *scaling exponent*. The density of the segment is given by

$$\rho_i = \mu_i/l_i = l_i^{\alpha-1}, \tag{2.41}$$

which diverges when $n \to \infty$, where $l_i \to 0$.

The scaling exponent is a classical notion in mathematics called the *Lipschitz-Hölder exponent* which controls the singularity of the density [6].

The singularities with exponent α is said to have a support of fractal dimension $f(\alpha) = D$ found by e.g. box counting of the d-measure, and which in this example is $f = log(2)/log(3)$. This example shows that the distribution (density) of a population (mass) may be seen to curdle onto tiny bar segments (support) when the generation number increases. Since the masses μ_i of each bar segment is equal in any given generation in this example they scale equally, and μ_0 is not

a multifractal measure. The point of this example is to show that if a population distribution curdles onto a specific number of sites which scales with a quantity (here n), the support is fractal. A more complicated example is needed to illustrate multiple fractal subsets.

The Lipschitz-Hölder exponents and fractal dimensions of subsets of the support

Imagine that the same initial bar as in the previous example was divided in half by the generator, which then assigned the mass $\mu_1 = 0.25\mu_0$ to the left half and the mass $\mu_2 = 0.75\mu_0$ to the right half. After n such generations, we have $N = 2^n$ bar segments of length $\delta_n = 2^{-n}$ with some mass μ. This is a binomial multiplicative process [6]. In this example, the masses μ_i of two bar segments are not necessarily equal but the total mass μ_0 is still conserved.

Consider the set $\mathcal{S}$ of N bar segments with a mass $\mu_i > 0$. This set is the support of the measure μ_0, and represents the whole initial bar, i.e it has the same dimension. The set $\mathcal{S}$ may however be separated into subsets $\mathcal{S}_k$ of points representing bar segments that have the mass μ_k, where $k = 1, 2, ..., m$ and m is the number of distinct values of μ_i observed in the n-th generation. The number m of distinct values of μ_i in the n-th generation is a consequence of all possible combinations that gives

$$\mu_i = {\mu_1}^i {\mu_2}^{n-i}, \tag{2.42}$$

where $i = 0, 1, ..., n$, which gives $m_n = n + 1$.

Therefore, we have $n+1$ subsets $\mathcal{S}_k$ of the original set $\mathcal{S}$ in the n-th generation, and if we define the mass μ_k in terms of the bar segment length $\delta_n = 2^{-n}$ and the Lipschitz-Hölder exponent α as [6]

$$\mu_k = \delta_n^\alpha, \tag{2.43}$$

we see that there are also m distinct values of α, one for each distinct mass value.

Then, the subsets $\mathcal{S}_k$ can equally well be written in terms of α . The union of subsets $\mathcal{S} = \bigcup_\alpha \mathcal{S}_\alpha$ completely describes the distribution of μ_0 over the n-th generation bar of unit length, and each subset is fractal with its own fractal dimension $f(\alpha)$ [6].

The sequence of mass exponents

A method to find the fractal dimensions of subsets of a multifractal measure, is to calculate the sequence of mass exponents $\tau(q)$ for the measure [6]. To understand the basics, assume that a multifractal measure is a population of N members distributed on a fractal support with a dimension D. The whole part $\mu_0 = N/N = 1$ of the population is distributed over all the points in the support containing different fractions μ_i of the population. Evidently, $0 < \mu_i < 1$ if the population is distributed over more than one point. This can be used to "enhance" the points in the support having a given μ_i and count the weighted number of boxes needed to cover this "enhanced" set of points as

$$M_d(q,\delta) = \sum_{i=1}^{N} \mu_i^q \delta^d = N(q,\delta)\delta^d \underset{\delta\to 0}{\longrightarrow} \begin{cases} 0, & d > \tau(q) \\ \\ \infty, & d < \tau(q). \end{cases} \tag{2.44}$$

Because $\mu_i < 1$, small values $q \to -\infty$ will make small values of μ_i dominate and large values $q \to \infty$ will make "large" values of μ_i dominate. The mass exponent $\tau(q)$ depends on the moment order q chosen, and the measure M_d is characterized by a whole sequence of mass exponents $[\tau(q_{min} < 0), \tau(q_{max} > 0)]$.

There is a connection between $\tau(q)$ and $f(\alpha)$ which can be used to obtain $f(\alpha)$ if we have $\tau(q)$ [6]. The equation

$$\alpha(q) = -\frac{d}{dq}\tau(q) \tag{2.45}$$

is used to find $\alpha(q)$, which is then put into

$$f(\alpha) = \tau(q) + q\alpha(q) \tag{2.46}$$

to find $f(\alpha)$.

We see that we can calculate $\tau(q)$ with the purpose of estimating the fractal dimensions $f(\alpha)$ of subsets of points that represents singularities $\mu = \delta^\alpha$ of the measure μ_0 supported by the union of these subsets.

2.5.1 Multifractal growth of two phase flow patterns

During two phase flow in porous media, the interface between the invading fluid and the defending fluid in the pore space can be represented by a set $\mathcal{H}$ of points representing N separate interfaces. This can be understood when considering that if the displacement front is situated at N pore necks, it consists of N small surfaces while the rest of the fluid interface is to the porous matrix. Between every invasion of a pore neck, the displacement front represented by $\mathcal{H}$ can be seen as a support populated with probabilities p_i which gives the probability that the interface $i = 1, 2, ..., N$ in $\mathcal{H}$ will invade the pore neck presented to it. These probabilities depend on parameters defining the flow such as the pore neck size and the pressure gradient, as well as on the same parameters at all other interfaces in $\mathcal{H}$. After each invasion, $\mathcal{H}$ will consist of a new set of interfaces assigned with a new distribution of invasion probabilities. Note that $\sum_{i=1}^{N} p_i = 1$ always holds, since during an invasion experiment it is certain that a pore will be invaded.

Consider a subset $\mathcal{N}$ of $\mathcal{H}$ which is the set of interfaces from where growth was observed in a time interval dt. The number of points N_I in $\mathcal{N}$ is the number of areas with observed growth, called *growth islands*. Each of the growth islands has a "mass" m_i that can be associated with a point i in $\mathcal{N}$, and the total "mass" of the observed growth is $m_0 = \sum_i m_i$. The set $\mathcal{N}$ is the support of the *new-growth* measure, where the growth islands has increments in the measure given by [6]

$$\mu_i = \frac{m_i}{m_0}. \tag{2.47}$$

To let the new-growth measure be distributed over many new-growth sites, dt should be chosen somewhere between a multiple of the time of one pore invasion and a fraction of the breakthrough time of the experiment t_0.

For a fractal structure it is expected that [6]

$$N_I = a\left(\frac{R_g}{\delta}\right)^{D_I}, \tag{2.48}$$

where R_g is the radius of gyration of the growth island stucture, a is an amplitude, δ is the pixel size at which the structure is observed and D_I is the dimension of the growing set of growth islands. D_I can be found by fitting eq. (2.48) to a plot of $log(N_I)$ vs. $log(Rg)$ for a fixed δ, or by finding the box counting dimension for a fixed R_g.

We see that the support of the new-growth measure, $\mu_i > 0$, is the fractal set $\mathcal{N}$ of N_I points. The μ_i values observed at different growth islands are different, so if we now divide $\mathcal{N}$ into subsets $\mathcal{N}_\mu$ which are the sets of points that has μ_i is in a range of $[\mu, \mu + \Delta\mu]$, we may find that such subsets are fractal if we specify μ in a scale independent way [6].

Direct analysis of $f(\alpha)$

To estimate the $f(\alpha)$ curve using the observed values of μ_i, we can specify subsets with a Lipschitz-Hölder exponent [6]

$$\mu = \left(\frac{\delta}{R_g}\right)^{\alpha} \quad \Rightarrow \quad \alpha = \frac{log(\mu)}{log(\delta/R_g)}. \tag{2.49}$$

If we choose the range for α as $\alpha + \Delta\alpha$, equation (2.49) gives us the corresponding range of μ_i for a structure having radius R_g observed at a resolution δ. The set of growth sites giving μ_i forms a subset $\mathcal{N}_\alpha$ of the set $\mathcal{N}$ containing all the growth sites, which can be written as

$$\mathcal{N} = \bigcup_{\alpha} \mathcal{N}_\alpha. \tag{2.50}$$

If $\mathcal{N}_\alpha$ is a fractal set, the number of points in the set is expected to have a scaling relation similar to eq. (2.48) as [6]

$$N_\alpha(\delta, R_g) = \Delta\alpha\rho_\alpha(\delta, R_g) = \Delta\alpha b_\alpha \left(\frac{R_g}{\delta}\right)^{f(\alpha)}. \tag{2.51}$$

$N_\alpha(\delta, R_g)$ is proportional to $\Delta\alpha$, so the density $\rho_\alpha(\delta, R_g)$ is introduced since it is independent on $\Delta\alpha$.

This could in theory be used to find the fractal dimensions $f(\alpha)$, but when we look at experimental data with a finite resolution we can only find estimates of $f(\alpha)$ for descrete values of α [6].

A set of $\{\alpha_i\}$ are calculated from the set of measured $\{\mu_i\}$ using eq. (2.49). The density $\rho(\alpha)$ is found from a histogram plot of $\{\alpha_i\}$, and according to eq. (2.51) we have

$$f(\alpha) = \frac{log(\rho(\alpha)) - log(b_0)}{\log(R_g/\delta)}. \tag{2.52}$$

Here, b_0 is the scale-independent part of b_α which is chosen such that $f_{max}(\alpha) = D_I$. Note that b_α may depend strongly on α, and by using b_0 instead implies that we get an effective exponent for $f(\alpha)$. This sets the maximum value of $f(\alpha) = 1$.

The Moments of the measure

The fractal measure defined on the growth sites can be studied by considering the moments of the observed measure, defined by [6]

$$M(q, \delta, R_g) = \sum_{i=1}^{N_I} \mu_i^q = N(q) \left(\frac{R_g}{\delta}\right)^{\tau(q)}. \tag{2.53}$$

For $q = 0$, it is found that $M(0, R_g) = N_I(R_g)$, and by comparing eq. (2.53) with eq. (2.48) we see that $\tau(0) = D_I$, and $N(0) = a$.

The mass exponents $\tau(q)$ can be found by fitting eq. (2.53) to experimental values of μ_i and R_g. Once the sequence of mass exponents is known, α and $f(\alpha)$ can be determined from equations (2.45) and (2.46).

Chapter 3

Experimental setup and methods

Transparent samples are essential when researching two phase flow in porous media since the main characterization of the flow is visual. The experimental raw data is in the form of digital images, and in order to get the best possible results there are certain aspects to consider: The choice of light source, contrast between the two fluids, framerate of image capturing, and how to process the raw data. Other non-trivial aspects when conducting experiments is the sample preparation and procedures during experiments. This chapter is meant to describe the details of the experimental methods so they can be reproduced and possibly improved.

3.1 General setup

The equipment necessary for the general experimental setup can be divided into 6 groups as shown in the diagram in fig. 3.1.

Particles and a viscous fluid are used to create a saturated 2 dimensional porous media sample inside the sample structure. During experiments, an inviscid fluid invades the saturated sample from the center until it breaks through at the sample edge. The particles are either introduced directly or through tubing, while the fluids are always introduced through tubing. The fluids and particles interact inside the sample structure, which provides the environment and support for the sample. Further, the transparent sample structure rests on top of a lightbox which has a uniform luminating surface, yielding a well contrasted image of the sample to the data capturing equipment. During the experiments the data capturing equipment records data which is saved to a connected computer.

In the following sections, this quick overview will be explained in detail part by part.

3.2 Fluid transfer

Tubing, connectors, stopcocks and syringes are needed for proper transport of fluids in experiments. This section will describe the various items used for fluid transport in the sample preparations and experiments.

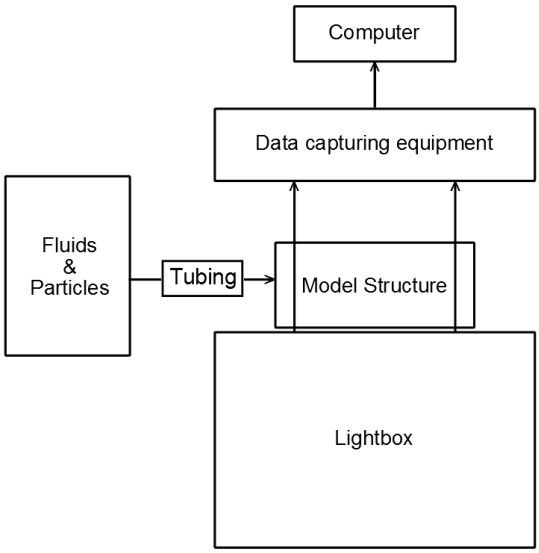

Figure 3.1: Diagram of the general experimental setup

3.2.1 Tubing

The tubing used is Tygon R-3603 Laboratory and Vacuum Tubing. It is a clear, transparent and flexible tubing, see fig. 3.2. Some of its features are among others good chemical resistance, the ability to be slipped over fittings and grip securely, a smooth inner wall which prevents buildup tubcite.

The R-3603 tubing comes in a wide range of cross sections, however in our experiments we have used tubing with three different cross sections, which we refer to as:

- *Small tubing* with I.D=3mm and O.D = 5mm.
- *Medium tubing* with I.D=5mm and O.D=8mm.
- *Large tubing* with I.D=6mm and O.D=9mm.

3.2.2 Connectors and stopcocks

Connectors

Connectors are components used to connect two or more pieces of tubing together. They come in different sizes and shapes depending on their function. We have used polypropylene connectors from Kartell Labware plastilab [concite]. Two-way connectors are used for joining two pieces of tubing and three-way connectors are used for joining three pieces of tubing. The connectors are available in many outer diameter dimensions.

The two-way connectors are straight tubes with tapered and serrated outsides to suit a range of tubing sizes with a tight and good grip. The three-way connectors are either "Y" shaped or "T"

Figure 3.2: A piece of "large tubing".

shaped. They are untapered but have serrations for a tight and good grip. Some examples are shown in fig. 3.3.

Stopcocks

At some tubing connections, it is necessary to control whether a fluid may flow through or not. In these cases a stopcock is used as the connector. All the stopcocks used are two-way Nalgene (6460-0004) stopcocks [stopcite]. The connectors are made of polypropylene and the TFE plug is made of Teflon. The stopcock connectors are serrated and tapered with O.D=6mm at the tip, O.D=10mm at the plug and I.D=4mm. Figure 3.4 shows a stopcock.

3.2.3 Syringes

All the syringes used are "BD Plastipak (300865)" 50ml syringes with Luer-Lok tips, see fig. 3.5 [syrcite]. The features of this syringe includes a clear barrel for visualization of syringe contents, silicon lubrication for smooth and even plunger movement and a Luer-Lok tip which ensures that it is leak tight even at high pressures. The syringe barrel and plunger rod are made of polypropylene, and the plunger tip is made of synthetic isoprene.

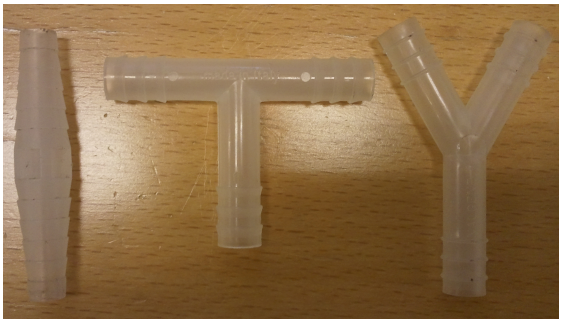

Figure 3.3: From left to right: a two-way connector, a "T" shaped three-way connector, and a "Y" shaped three-way connector.

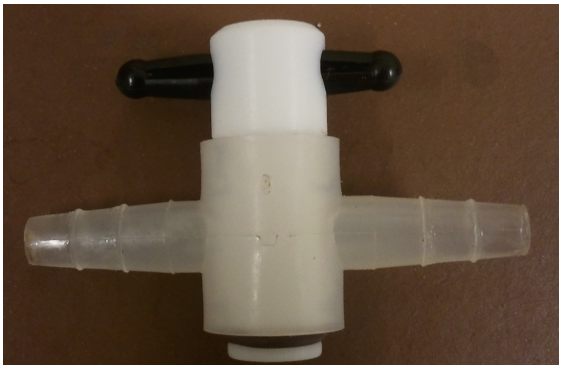

Figure 3.4: A "Nalgene (6460-0004)" stopcock.

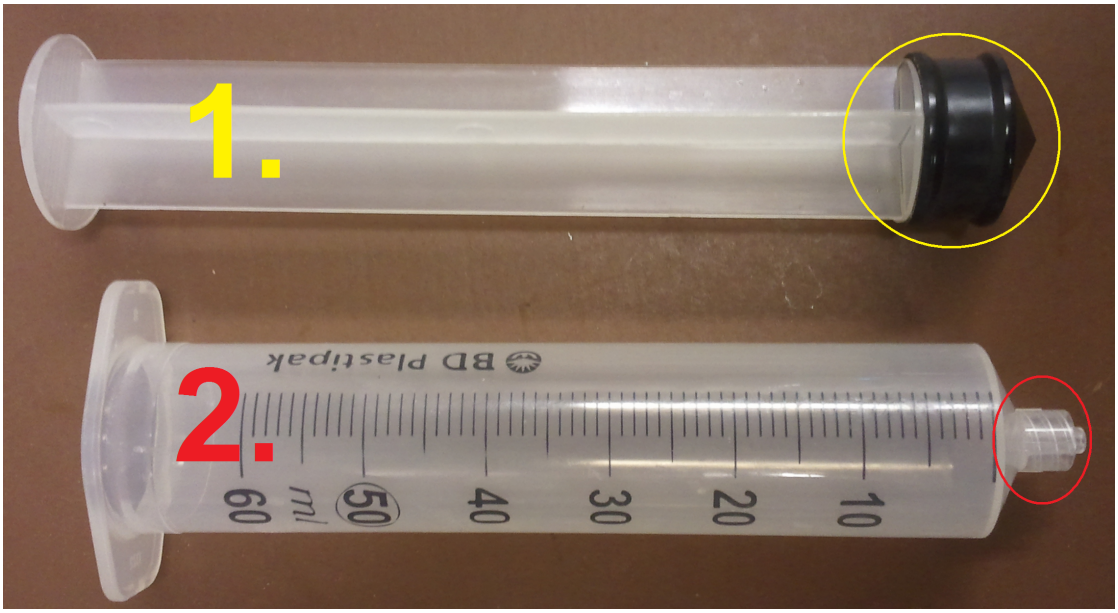

Figure 3.5: A "BD Plastipak (300865)" 50ml syringe. The parts are indicated by color and numbers. 1: Plunger with plunger tip indicated by the yellow circle. 2: Syringe barrel with Luer-Lok syringe tip indicated by red circle.

Extension tube

The syringe is compatible with the BD Connecta (397509) extension tube, which is a 50cm long PVC tubing with I.D=2mm and O.D=4mm. At one end is a male Luer-Lok connection and at the other end is a female Luer-Lok connection. The connections are made of polypropylene coated with ABS and polycarbonate.

3.3 Fluids and particles

In the experiments we use air as the invading fluid, an aqueous glycerine solution as the defending fluid and glass beads to create the porous media matrices.

3.3.1 Air supply and pressure control

Air supply

The air source is pressurised air supplied to the lab. The source pressure is controlled with a wall mounted pressure regulator set to 2bar. Connected to the source regulator is a 3m hose with a gun shaped valve at the end. The gun shaped valve is normally shut, but is opened when the trigger is pulled. A small clamp on the trigger can be used to keep the air flowing, which will be referred to as *triggering the air*. A 3m piece of tubing connects this valve to the inlet of a second pressure regulator. This regulator is used to control the air supply pressure in experiments, and

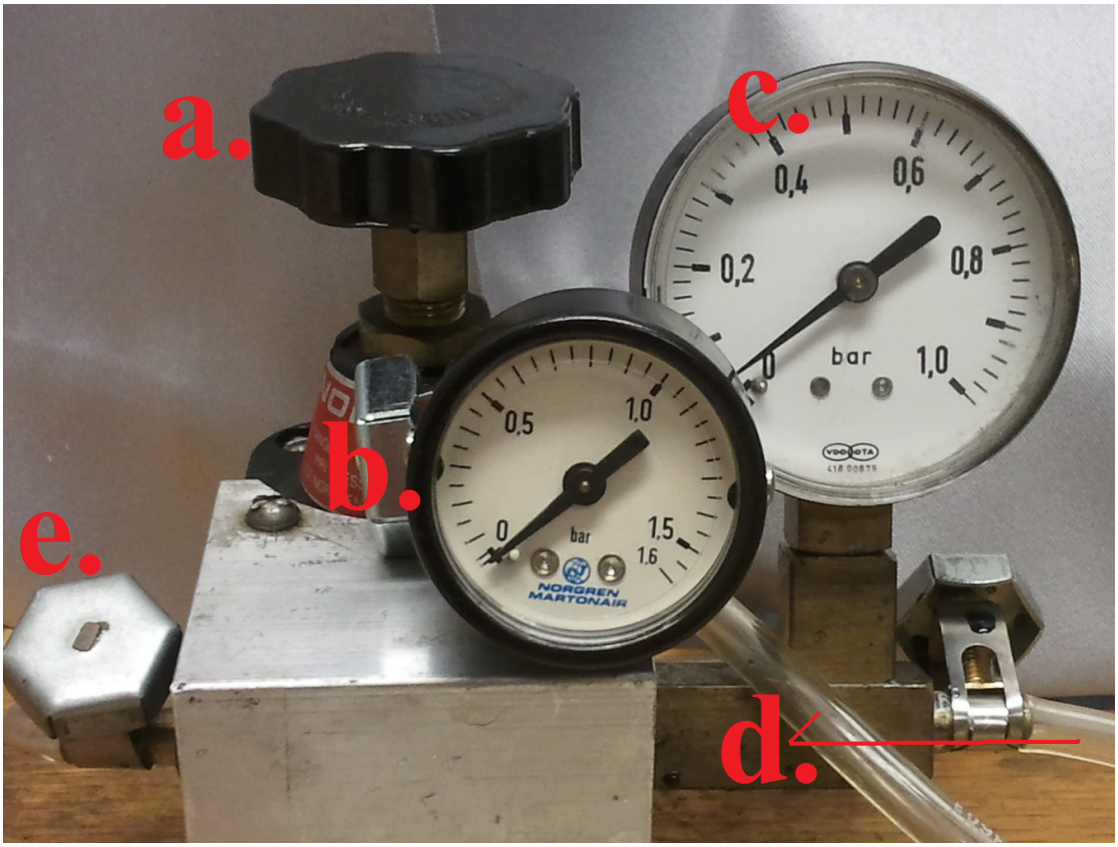

Figure 3.6: Both pressure gauges are checked when regulating the pressure. Regulation of the pressure is done by turning the knob (a) while the inlet (e) air flow is triggered. The first (c) and second (b) pressure gauges indicates the overpressure with respect to the atmosphere. The outlet air supply (d) is connected to the second gauge which blocks the air flow.

it has an analog pressure gauge attached. The pressure gauge ranges from 0 to 1bar with 0.25bar increments, 3.6. A 1.2m piece of tubing is connected to the outlet of the regulator, and this tube will be referred to as the *air supply*.

Air pressure configuration

The desired air supply pressure may change from experiment to experiment, and can be adjusted with the pressure regulator. A second pressure gauge is connected to the air supply, blocking it as well as double checking the air supply pressure. When the airflow is triggered, we can adjust the air supply pressure while looking at the two pressure gauges. The airflow is cut when the desired air pressure is reading on both of the pressure gauges as seen in fig. 3.6. After about 10 seconds the airflow is triggered again to double check the air pressure, and eventual corrections are made. When the regulator setting is satisfying, the blocking pressure gauge is removed and the air supply is ready for use.

Figure 3.7: Left: The vacuum excitator containing a sample and connected to the vacuum pump. Right: An "acid black 2" sample of aqueous glycerol.

3.3.2 Liquid preparation

The liquid fluid preparation is performed in three steps, the water dying, the mixing of water with glycerine and the extraction of unwanted air bubbles from the liquid mixture.

Water dying is necessary in order to achieve good visible contrast between air and the liquid. The dye used for this is water soluble Nigrosine. It gives the water a blue-black color commercially called "acid black 2". While nigrosine is easily soluted in water, it is a coarse grained powder, so the water must be dyed before it is mixed with glycerine for the liquid to be properly and evenly dyed.

Glycerine is more viscous than water, but the two liquids mix. So in order to make a more viscous liquid we make a mixture of 80% glycerine and 20% dyed water. The ratio is by weight, so the liquid parts are weighed on a Mettler PE3600 Deltarange, a sensitive scale with an accuracy of 10^{-1} grams mettcite. When the weight ratio of the fluids is correct they are mixed into an even mixture, stirring for about 1-2 minutes with a glass rod.

The mixing and stirring creates air bubbles in the liquid mixture. These are unwanted and have to be removed. Therefore the container with the liquid is put into a vacuum excitator, which is a vacuum proof glass tank from which the containing air can be pumped out, showed in fig. 3.7. The air is pumped out by a vacuum pump, and the fluid is left in medium vacuum for about 10-15 minutes. This treatment causes the air bubbles to "boil" out of the liquid mixture.

After the liquid is prepared, it is stored in a capped bottle marked with the date and content. The liquid is ready for use in experiments, and a specimen of approximately 100ml is stored for later use, e.g. to determine fluid properties such as viscosity.

3.3.3 Glass beads

The particles used to create the porous media samples are spherical glass beads of diameters ranging from 1mm to 1.18mm. Glass beads are used because of their transparency and similar wetting properties as the sample walls.

3.4 Sample structure

3.4.1 Sample plate

The sample plate is a circular plexiglass disc with a 40cm diameter and a thickness of 2.5cm. Through the center of the disc there is a circular hole of 0.9cm in diameter. We distinguish the two plane surfaces of the sample plate as the *top side* and the *bottom* side.

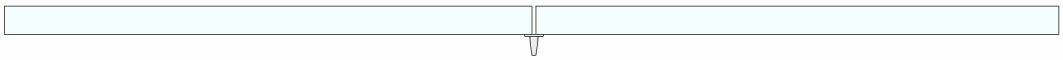

Figure 3.8: Cross section of sample plate without sample.

The top side is where the porous media sample is built. The bottom side has a removable nipple where the fluid injection tubing can be connected. The purpose of the sample plate is to provide a transparent, rigid and circular plane that can support a 2 dimensional porous media sample as well as it allows us to perform a central fluid injection in that sample.

3.4.2 Non-deformable porous media sample holder

The non-deformable porous media sample holder consists of a circular aluminum frame with inner diameter of 41.2cm, outer diameter of 48.8cm and height 2.2cm. There is a 1cm indent from the top along the inner 1.9cm of the frame. A transparent mylar film with larger diameter than the frame is placed over it, and the center of the film is pushed slightly down such that it dips about 1 cm in the center. Now, a 1cm thick plexiglass disc with diameter of 45cm is put over the mylar film and fitted inside the indent in the frame. To keep it all assembled, another 0.8cm thick aluminum frame with the same circular dimensions as the bottom frame is fastened on the top with eight evenly spaced screws.

Eight holding brackets evenly distributed around the frame bottom are designed to hold the sample plate. The holding brackets are able to rotate around their attachment for easy insertion/removal of the samples. The brackets also have adjustable screws allowing the holding distance under the plexiglass plate to be adjusted.

The non-deformable porous media sample holder has two important support functions. The first is to carry the sample plate and the second is to add pressure to the sample top to maintain the quasi 2-D geometry of the sample during injection. A cross section of the frame is illustrated in figure 3.9.

Pressure is applied to the sample plate top by inflating the pressure cushion. The inflatable air cushion consists of the air tight, non-streching mylar film which confines air between it and the plexiglass top of the sample holder. The plexiglass plate has two air inlets/outlets. One of them

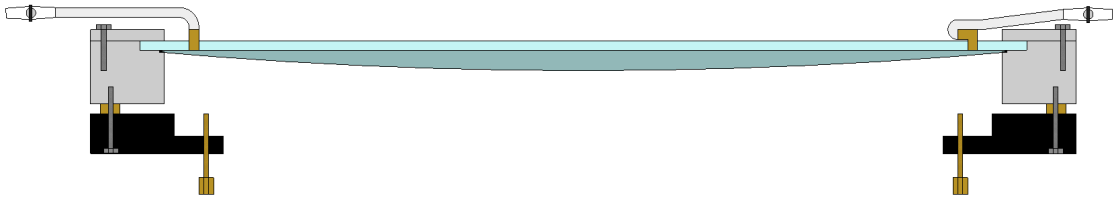

Figure 3.9: Illustrative cross section of the non deformable porous sample holder

is sealed and can be ignored, while the other is in use as both air inlet and outlet for the cushion. A stopcock must be used to keep the cushion inflated.

3.4.3 Deformable porous media sample holder

The deformable porous sample holder consists of a circular metal frame as in section 3.4.2, a 1cm thick 50x50cm glass pane, a syringe with extension line, 4 clamps and a 136cm long piece of large tubing. There is a radial groove at the bottom surface of the circular frame. It goes all the way from the inner diameter to the outer diameter of the frame and is about 5mm deep and 3mm wide. A syringe extension line is glued into this groove with Scotch gel glue, with as much as possible of the length of the extension line kept on the outside of the frame. The excess extension line at the inner edge of the frame is cut off. Some gel glue is also put on top of the extension line to seal the groove. Next, the ends of the 136cm piece of large tubing are put together, one tucked inside the other, enabling it to be formed as a circle of somewhat larger radius than the inner radius of the frame. The circle made of tubing is centered on the glass plate and the metal frame is placed centered on top of it. The circular frame is clamped to the glass pane with 4 clamps, one at each edge of the glass pane. The tubing circle has the role of forming a liquid-proof seal between the glass and metal interfaces.

3.4.4 Injection tubing and support blocks

Support blocks

The support blocks are 4 equal brass blocks with a square cross section of 2.5x2.5cm and a height of 10cm. They are placed standing on the lightbox so that the frame of the sample holder can rest on them. The purpose of the support blocks is merely to elevate the sample structure to make room for the injection tubing underneath.

Injection tubing

The injection tubing is designed to control the injection of up to two different fluids into the center of the sample plate. It allows us to inject two fluids separately in a desired order without having to change the tubing connected to the sample plate. Note that the injection tubing may also be used to control the injection of just one fluid. The injection tubing consists of three pieces of medium tubing connected together in a T shaped three-way junction, the sample connection tubing, the air injection tubing and the liquid injection tubing, see fig. 3.10.

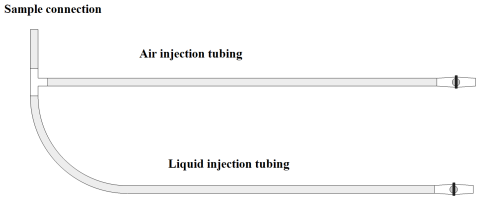

Figure 3.10: Illustration of the injection tubing

The sample connection tubing is 1cm in length from the junction connection to its end. It is used for attaching the T-junction to the sample plate nipple. When connected to the sample plate, the junction is oriented such that there is one branch perpendicular to the nipple and one parallell to it.

The air injection tubing is connected to the perpendicular branch of the junction, and its length is 50cm measured from the junction to the stopcock at the other end where the air supply can be connected. The stopcock is closed during liquid injection, preventing liquid from entering the air supply.

The liquid injection tubing is 40cm long, measured from the parallell branch of the junction to the stopcock connected at its other end. The liquid supply can be attached to the stopcock, which should be kept closed during air injection.

3.4.5 The assembled sample structures

Assembly of the non-deformable porous media sample structure

1. The sample plate is placed on the support blocks on the lightbox.
2. The non-deformable porous media sample holder is lowered onto and centered on the sample plate.
3. The holding brackets of the sample holder is rotated towards the center of the sample, and the adjustment screws are adjusted if necessary.
4. The support blocks are moved out to the frame of the sample holder, where they can now support the entire sample structure.
5. The injection tubing is connected.

The cross section of the assembled non-deformable porous media sample structure is shown in fig. 3.11

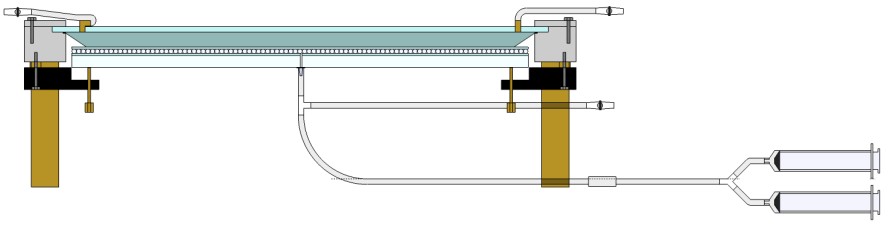

Figure 3.11: Illustration of the assembled non-deformable sample structure.

Assembly of the deformable porous media sample structure

1. The sample plate is placed on the support blocks on the lightbox.
2. The deformable porous media sample holder is lowered onto and centered on the sample plate.
3. The sample plate and sample holder are clamped together with 4 clamps which should be separated no more than 1cm from a sample holder clamp each.
4. The support blocks are moved out to the frame of the sample holder, where they can now support the entire sample structure.
5. The injection tubing is connected and both its stopcocks are closed.

The assembled deformable porous media sample structure is shown in fig. 3.40

3.5 Lightbox

The lightbox is an experiment platform with background lighting through a transparent surface. Background lighting is a good way to luminate a sample without getting glare, as we would get by using reflective lighting. For the best possible raw data results, i.e. digital images with good contrast, the lightbox is constructed to yield a uniform white light with an even intensity distribution over its surface. In addition, the lighting must be bright enough to provide good contrast between air and dyed liquid in the sample.

The lightbox can be divided into three parts: The box, the surface and the light system, fig. 3.12. The box itself is a wooden 81x71cm box with height of 25cm. The top side is open and equipped with a frame of height 2.5cm, inner dimensions of 81cm by 71cm and outer dimensions of 85cm by 75cm. The 75cm sides of the box are referred to as the front and the back sides. There is a maintenance door at the front side, and there are vent holes with cooling fans on both the front and the back sides.

The light system is inside the box. The interior walls and floor are coated with a reflective film of aluminum foil. Ten Osram Lumilux HO 24W/830 fluorescent light tubes are placed centered on the floor, evenly spaced between the front and back walls oriented parallell to them. The light tubes yields a warm white light of 3000K [osramcite]. The lightbox is powered by the AC electric grid with voltage of 230V and frequency of 50Hz. 5 Quicktronic intelligent ballasts (QTI 2x14/21/24/39 GII) control the current through 2 light tubes each [balcite]. On the front side of the lightbox is a lightswitch mounted as the power switch.

Figure 3.12: The lightbox is displayed with its interior. The surface is placed as a lid on the top of the box.

The surface consists of a 2cm thick glass pane covered with a 0.5cm thick, opaque white plexiglass sheet. The combination is a rigid 80cm by 70cm rectangular surface which fits within the frame on the top of the lightbox and sits on top of the walls. When the lightbox is turned on the surface luminates with a uniform white light.

3.5.1 Flicker issue with high speed camera

Fluorescent lights have a periodically oscillating light intensity. The frequency ω of this oscillation depends on the frequency f of the supplied AC current. Typically $\omega = 2f$ oscite, which gives 100 oscillations per second for our AC current supplied from the electric grid. For a highspeed camera recording images at framerates $\geq \omega$, this intensity fluctuation creates obvious frame to frame contrast and intensity differences. This is a problem which makes it difficult to treat raw data frames equally during image processing, and may led to loss of information.

We have examples and analysis of this problem because the light system of our lightbox had to be modified and improved to address the flicker issue.

Intensity fluctuation analysis

For simplicity we will refer to the lightbox as the *old lightbox* when it contained the old light system, and as the *new lightbox* after it got the new light system installed. Two 250fps footages of saturated samples were selected for analysis, one with the old lightbox and the other with the new lightbox. Two analytic methods were used to evaluate flicker: visual and qualitative.

The visual analysis of the footages was done by visually comparing the 12 first frames to see if the flicker was observable.

The qualitative analysis was performed in Matlab on the first 100 frames of the footages, corresponding to the first 0.4s. The time dependent mean pixel intensity $I_m(t)$ and time t in seconds is calculated for each frame. The period p of the intensity oscillation can be visually evaluated from flicker plots of $I_m(t)$ vs. t. The amplitude A of the oscillations can be found by calculating the time averaged mean intensity $\bar{I}_m$, assuming a minimum I_{min} or a maximum I_{max} of $I_m(t)$ and use either

$$A = \bar{I}_m - I_{min} \tag{3.1}$$

or,

$$A = I_{max} - \bar{I}_m. \tag{3.2}$$

As a periodic function, $cos(x)$ was selected (we could equally well use $sin(x)$), and a test function

$$g(t) = Acos(2\pi t/p) + \bar{I}_m \tag{3.3}$$

was plotted together with the datapoints of $I_m(t)$ vs. t . Finally, the phase ϕ can be found from the offset t_{offset} of the test function extremum from the assumed I_{min} or I_{max} as

$$\phi = -t_{offset}. \tag{3.4}$$

Now, we have all the values we need to create a fitted periodic function $f(t)$ to the data points of $I_m(t)$,

$$f(t) = Acos(2\pi t/p + \phi) + \bar{I}_m. \tag{3.5}$$

Old lightbox results

The first 12 frames of the old lightbox are tiled in fig. 3.13, they clearly shows flicker.

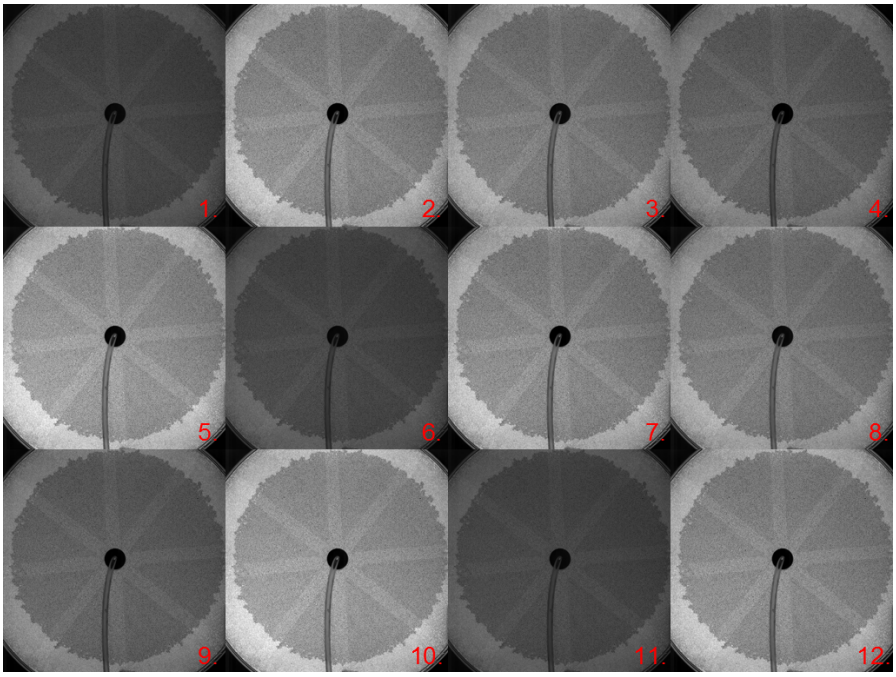

Figure 3.13: The first 12 frames of the old lightbox

The first 100 frames were processed in Matlab as described and the resulting $I_m(t)$ vs. t is plotted in fig. 3.14. A periodic function was fitted to the flicker data as explained. The minimum of $I_m(t)$ was assumed to be $I_{min} = 69.54$, and the time averaged mean intensity was calculated to be $\bar{I}_m = 111.288$. Putting these values into (3.1) gives the flicker amplitude $A = 41.7488$. The period was evaluated and assumed to be $p = 0.01s$.

These parameters are put into the test function (3.3) which is plotted together with the data points. A phase jump at $t = 0.08s$ was discovered, with $t_{offset1} = -0.001$ before the phase jump and $t_{offset2} = 0.005$ after. Eq. (3.4) gives us the phases $\phi_1 = 0.001$ and $\phi_2 = -0.005$.

Using (3.5) we find that the flicker fit function for the analyzed frames of the old lightbox is $f_1(t) = 41.7488 \cdot cos(200\pi t + 0.001) + 111.288$ for $t < 0.08s$, and $f_2(t) = 41.7488 \cdot cos(200\pi t - 0.005) + 111.288$ for $t \geq 0.08$. Note that the phase jump is unrelevant when evaluating the flicker, and that the flicker amplitude and period are constant. The first 0.15 seconds of the flicker fit function is plotted in fig. 3.15.

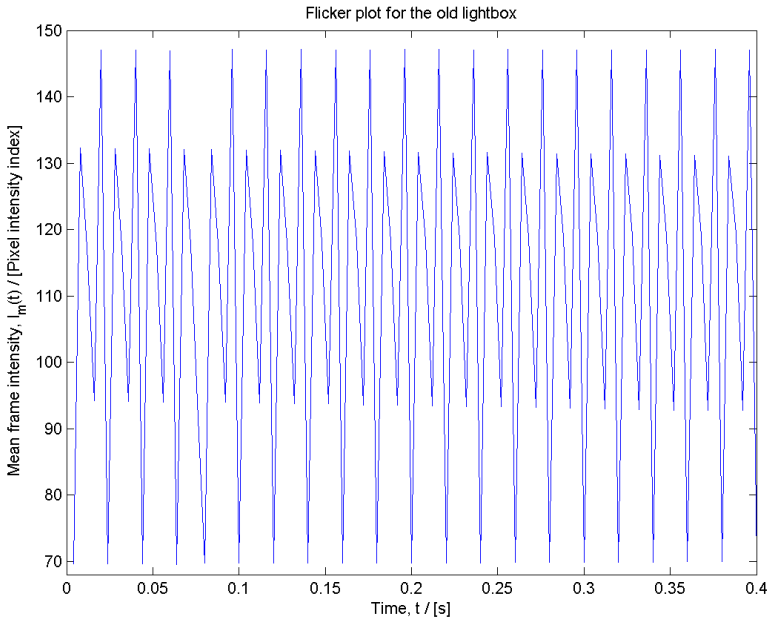

Figure 3.14: The mean frame intensity fluctuations of the old lightbox

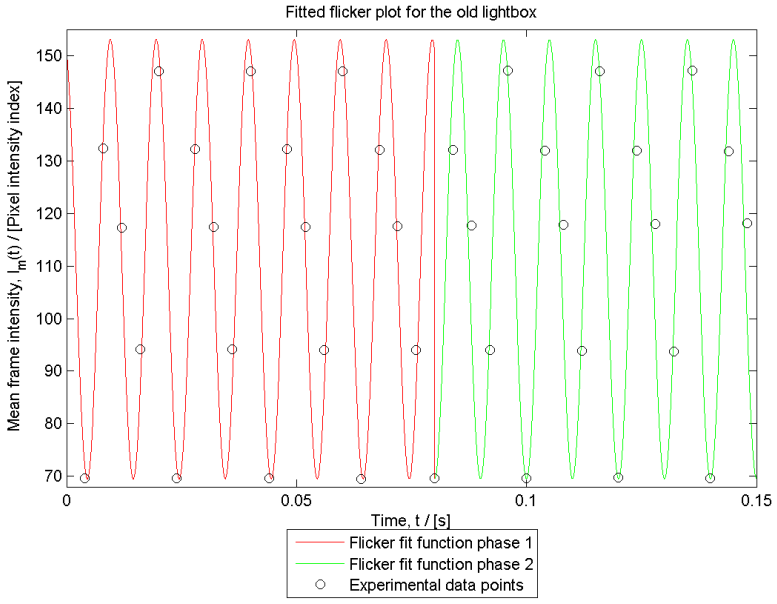

Figure 3.15: The first 0.15s of the fitted flicker function for the old lightbox

New lightbox results

The first 12 frames of the new lightbox show apparantly no intensity fluctuations, fig. 3.16.

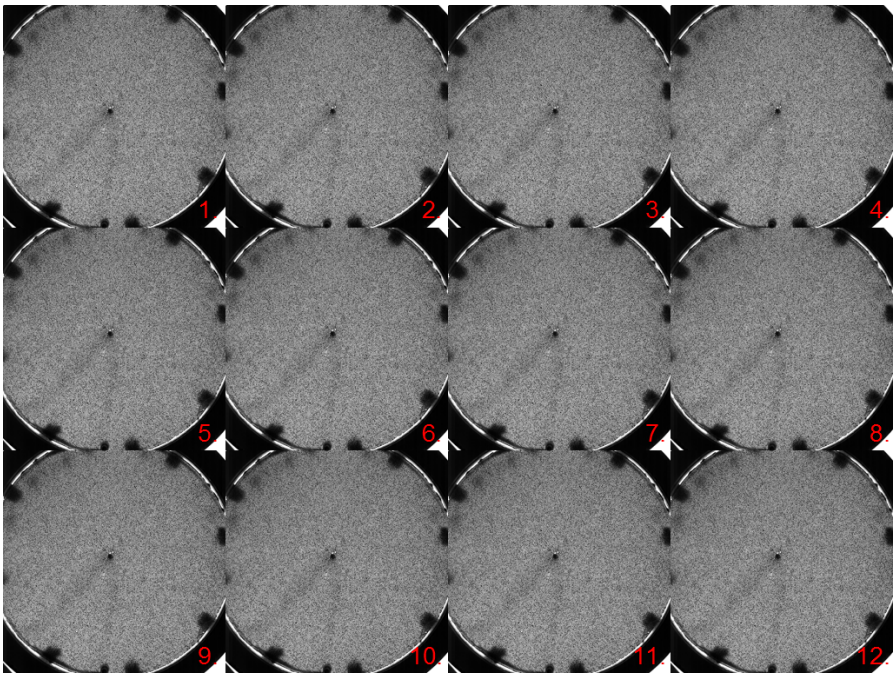

Figure 3.16: The first 12 frames of the new lightbox

For the qualitative analysis, the first 100 frames of the new lightbox are processed in Matlab. The flicker plot is plotted (fig. 3.17) and the parameters are determined. The assumed maximum of $I_m(t)$ was $I_{max} = 113.76$. The time averaged mean frame intensity was calculated to $\bar{I}_m = 113.0997$, and by inserting the values into (3.2) we get the flicker amplitude $A = 0.6603$. The period was evaluated as $p = 0.01$ from the flicker plot. The parameters are put into the test function $g(t)$ which is plotted together with the data points. The offset is found from the plot as $t_{offset} = -0.00436$, which gives the phase $\phi = 0.00436$. The flicker fit function for the analyzed frames for the new lightbox is found to be $f(t) = 0.6603 \cdot cos(200\pi t + 0.00436) + 113.0997$. The first 0.15 seconds of $f(t)$ vs. t is plotted together with the experimental data points in fig. 3.18.

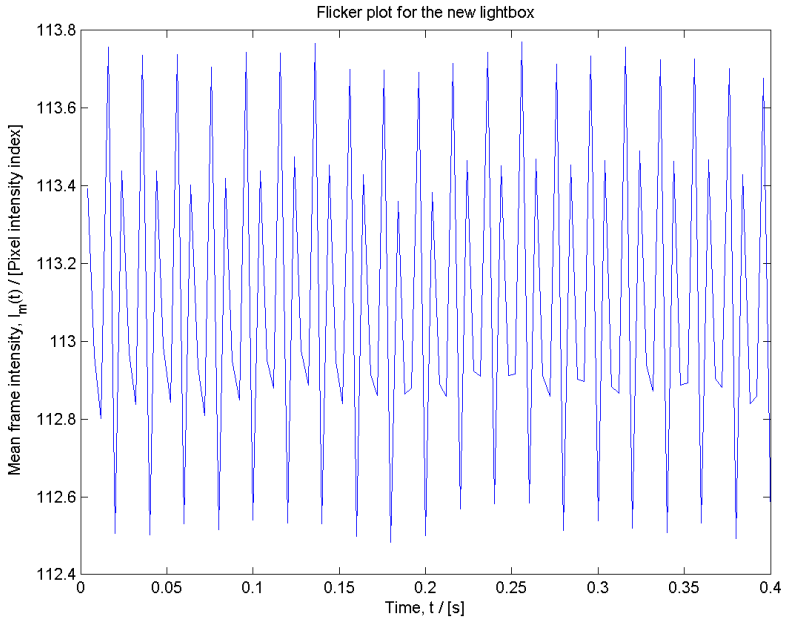

Figure 3.17: The flicker of the new lightbox system

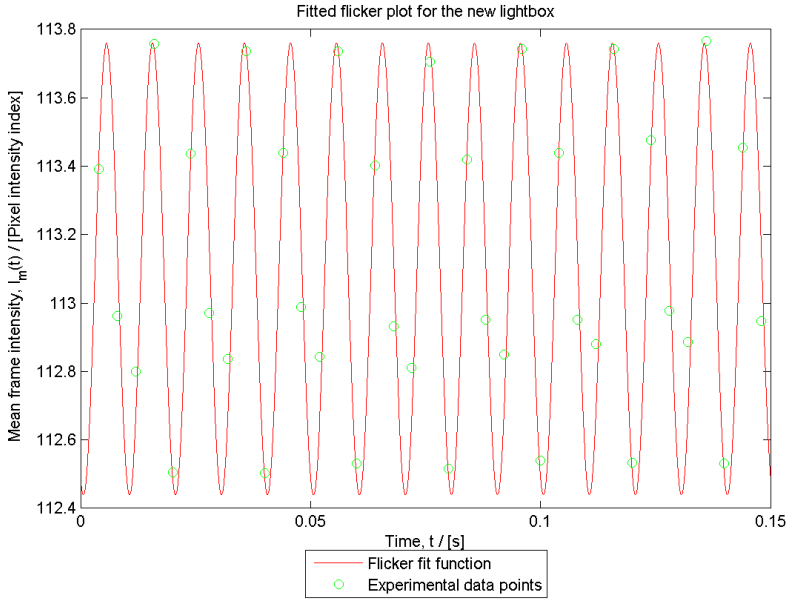

Figure 3.18: The fitted flicker function of the new lightbox

A conclusion on the flicker problem

The fitted flicker functions found in the qualitative analyses carries information about flicker amplitude, average mean frame intensity, flicker oscillation frequency and phase. Note that the phase is arbitrary depending on when the recording is started, and not relevant in this discussion. The oscillation frequency $1/p$ of the flicker is the same for the old lightbox and the new lightbox, and it satisfies the relation $\omega = 2f$ since $1/p = 100\text{Hz} = 2 \cdot 50\text{Hz}$.

The ratio of the flicker amplitude to the average mean frame intensity $A/\bar{I}_m$ gives us the relative amplitude of the oscillations. Calculations of the relative amplitudes tell us that the old lightbox had flicker with an amplitude of about 37.5% around its averaged mean intensity while the new lightbox only had flicker with an amplitude of about 0.6%. The flicker fit functions for the old lightbox and the new ligthbox are plotted together in fig. 3.19, showing the difference. This result fits well with the initial visual analyses.

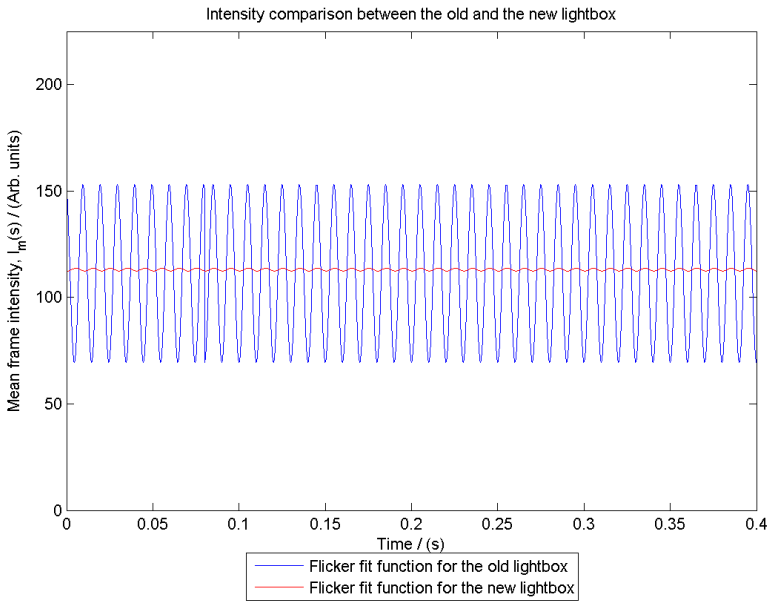

Figure 3.19: Intensity fluctuations of the old and new lightbox compared to eachother.

From the analyses, it appears that we can not get rid of the oscillation frequency ω of the flicker, but it may however be modulated by the frequency f of the driving current as $\omega = 2f$. However with better performing light systems, the relative flicker amplitude can be reduced to under 0.6%. According to the visual analysis, flicker with a relative amplitude of $< 0.6\%$ is unsignificant and we do not have to consider the flicker frequency at all.

3.6 Data capturing equipment and computer

3.6.1 High speed camera

The high speed camera used is a Photron FASTCAM SA5 775K-M2 [hcite]. The Fastcam features a 12-bit ADC (analog-to-digital converter) image sensor with 20μm pixels returning monochrome images, Nikon F-mount for attachement of a selection of lenses, 16GB of internal memory and a Gigabit Ethernet 1000BASE-T interface for connection to a computer. The Fastcam delivers a megapixel resolution up to 7500fps, a maximum framerate of 775000fps and has a variety of trigger methods to start and end a recording session.

The Fastcam is connected to a 1000BASE-T compatible computer via a category 5e UTP cable. The computer has the program "Photron Fastcam Viewer v.3" (PFV) installed, which is used to control the Fastcam. During a recording session the Fastcam records images to its internal memory, so PFV is also used to download the recorded frames to the computer. The Fastcam is physically mounted to a stable tripod which is able to pan and rotate the camera, making it easier to align samples into the field of view. Relative to the lightbox, the Fastcam is positioned about 1m directly above the center of its surface facing straight down.

Fastcam preparation

Most of the pre-recording preparations of the high speed camera is done in the camera control software, PFV, which has a user interface as shown in fig. 3.20. Several parameters such as framerate, trigger method, contrast, spatial resolution, etc. can be configured. Only the relevant settings will be discussed here. When a certain configuration is going to be used several times, the settings can be saved to a camera setup file which can be loaded at later times. This saves time as well as creating a default experimental configuration, eliminating the possibility of mistakes and differences between experiments.

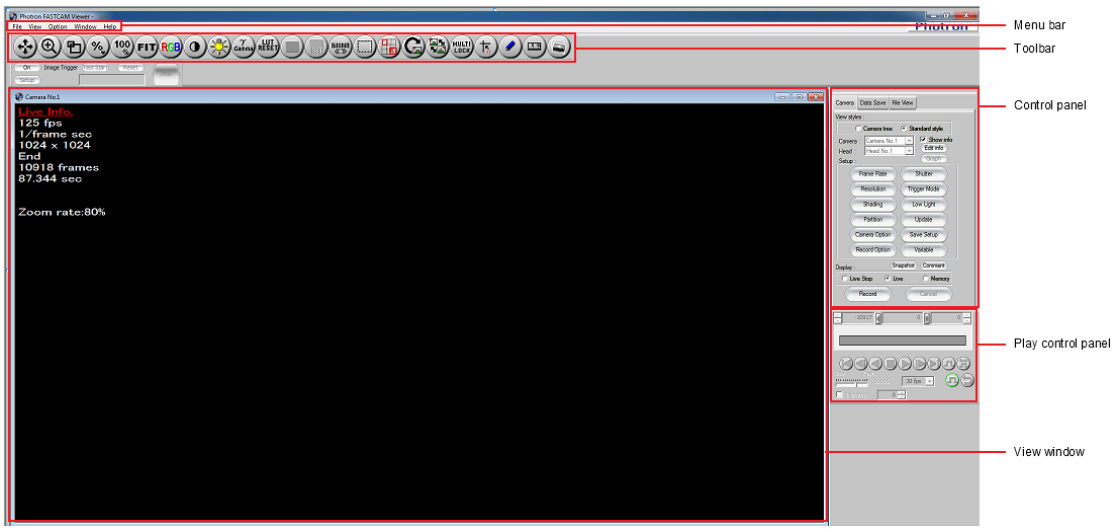

Figure 3.20: The user interface window of the Photron Fastcam Viewer is divided into 5 sections: Menu bar, toolbar, control panel, play control panel and view window.

The adjusted settings are the resolution, framerate and trigger method. The spatial resolution is configured by clicking the "Resolution" button in the control panel, fig. 3.21. A list of choices shows up, but we will always use the maximum resolution of 1024x1024 pixels. The recording framerate is configured by clicking the "Frame Rate" button in the control panel, fig. 3.21. A suitable framerate can be selected from the list. Note that the maximum resolution only supports framerates up to 7000fps. The trigger method is configured by clicking the "Trigger Mode" button in the control panel, fig. 3.22. A list of methods appear, but we will always use the "End" method. The "trigger end" function ensures the recording of an event we know will happen, but not exactly *when* it happens. The method works by starting a continuous recording session before the event. When the memory gets full, new frames overwrite the oldest, making the Fastcam "remember" the 10918 most recent frames there is room for in the memory. After the experimental event has occurred, the continuous recording is stopped by the trigger.

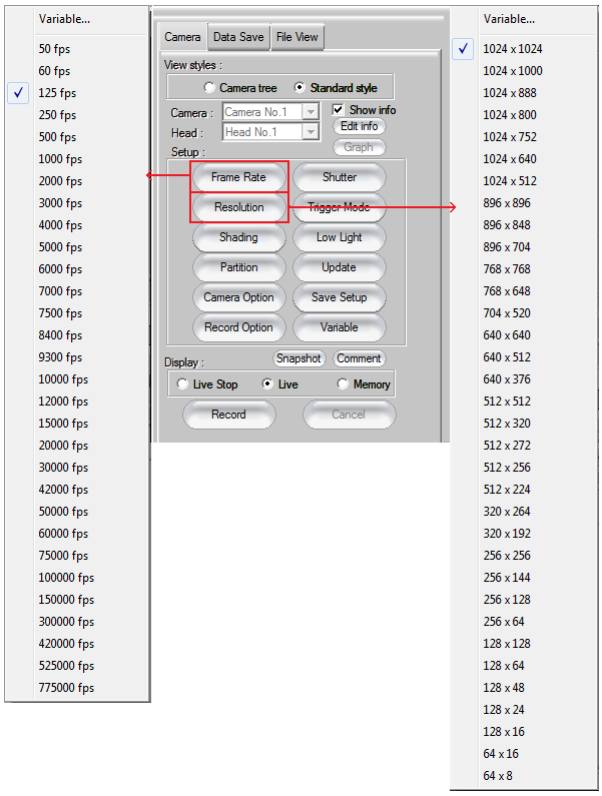

Figure 3.21: The "Resolution" and "Frame Rate" options in the control panel.

Saving these configurations to a camera setup file is done by clicking the "Save Setup" button in the control panel, fig. 3.23. Click "Save" in the pop-up window and choose a suitable name and location. To load these configurations at later times, click the "Save Setup" button and "Load" in the pop-up window. Here we can select a camera setup file we have saved earlier.

Whenever the framerate settings are adjusted or a camera setup file is loaded, it is important to calibrate the camera shading. Shading calibration is a correction of the non-uniformity of the pixels in the image sensor [shadcite]. Using a black image as a standard, the system uses a correction function to zero the dark signal for all pixels. This is done by clicking the "Shading"

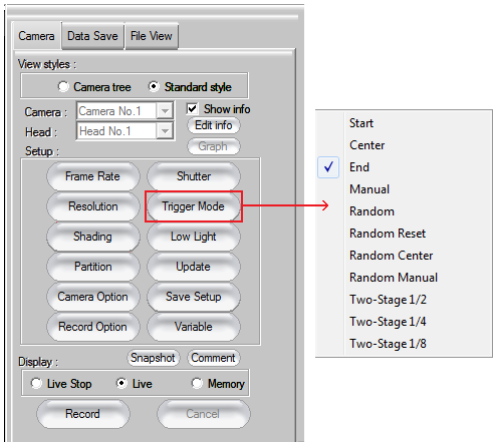

Figure 3.22: The "Trigger" options in the control panel.

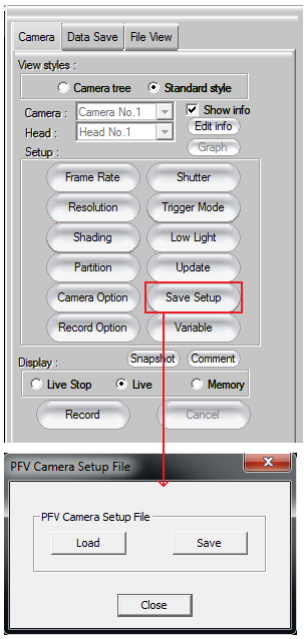

Figure 3.23: The "Save Setup" option in the control panel.

button in the control panel, fig. 3.24. With the lens cap attached on the camera, click the "Calibrate" option that appears.

The lens cap can be removed after the shading calibration is complete. The sample and camera positions are adjusted to align the entire sample within the picture frame. This is achieved while looking at the live feed in the view window, fig. 3.20. The lens is focused if necessary. If the image is too dark, brightness can be adjusted by selecting a smaller shutter opening on the lens. Other image enhancements may be performed by using options in the PFV toolbar, fig. 3.20.

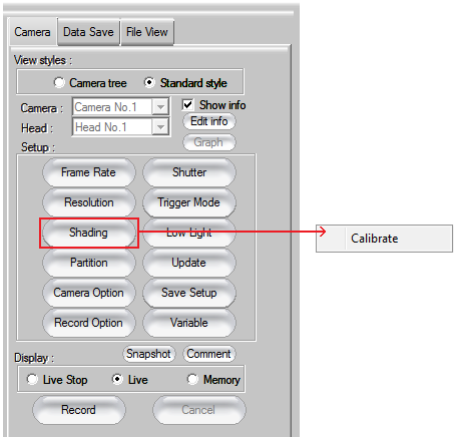

Figure 3.24: The "Shading" option in the control panel.

Starting and stopping recording sessions

A record mode called "Direct start" is used. To select this mode click "Option" in the menu bar and click "Configuration". In the configuration window, go to "Record Option" and select "Direct Start" as type of record mode, fig. 3.25. In the "direct start" mode, the recording session starts immediately after the user clicks the "Record" button in the control panel 3.26. When clicked, the "Record" button turns green and says "Endless Rec" to indicate active recording. To stop the recording session, the green "Endless Rec" button can be clicked, as PFV inteprets this as a stop trigger.

Saving recorded frames from memory

After a recording session is stopped, the display mode in the control panel automatically goes into "Memory" mode, fig. 3.27, and the play control panel, fig. 3.20, becomes active. This means that the captured frames in the Fastcam memory can be viewed in the view window.

By reviewing the footage, we reveal the position and time interval of the interesting event. By using the play control panel to specify the start and end frames to fit this interesting interval as shown in fig. 3.28, many uninteresting frames before and after the experimental event are excluded from playback. Only frames within the specified playback sequence will be saved to the computer disk when the save function is used.

When we are satisfied with our specified playback sequence, it is time to save the frames to the computer disk. This is done by clicking the "Data Save" tab of the control panel, fig. 3.29. Then, a save path and a suitable name are typed in. The file save format is selected as png-images from the drop-down box. Make sure that the "Skip save" box is unchecked, e.g. if "Skip save=2" is enabled, a 2 second sequence of 1000 frames at 500 fps will be saved as a 2 second sequence of 500 frames at 250fps. This can be confusing and lead to errors during analysis. After eventually unchecking the "Skip save" box, the "Save" button is clicked. A data folder with the suitable name will be created in the selected save path. The frames from the playback sequence are saved as PNG-files, with the specified name plus a frame number, inside the data folder. In addition

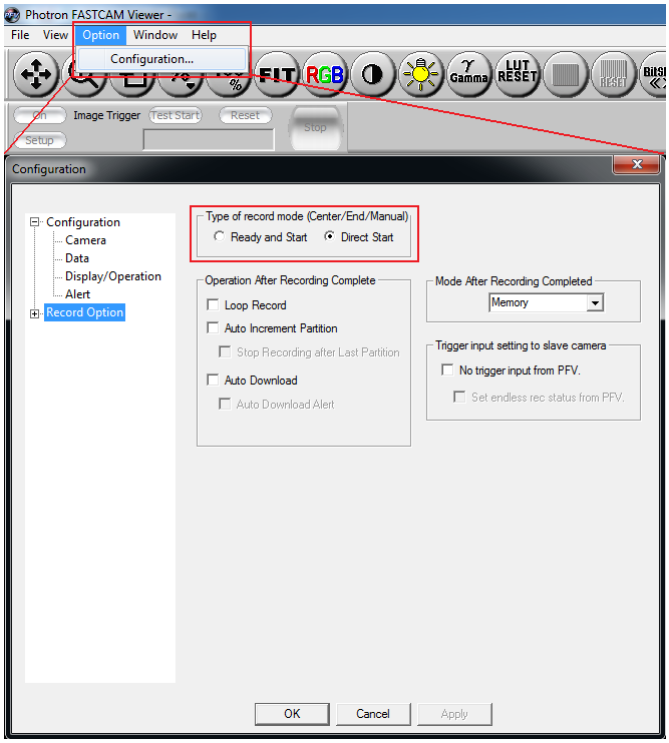

Figure 3.25: The selection of record mode from the menu bar.

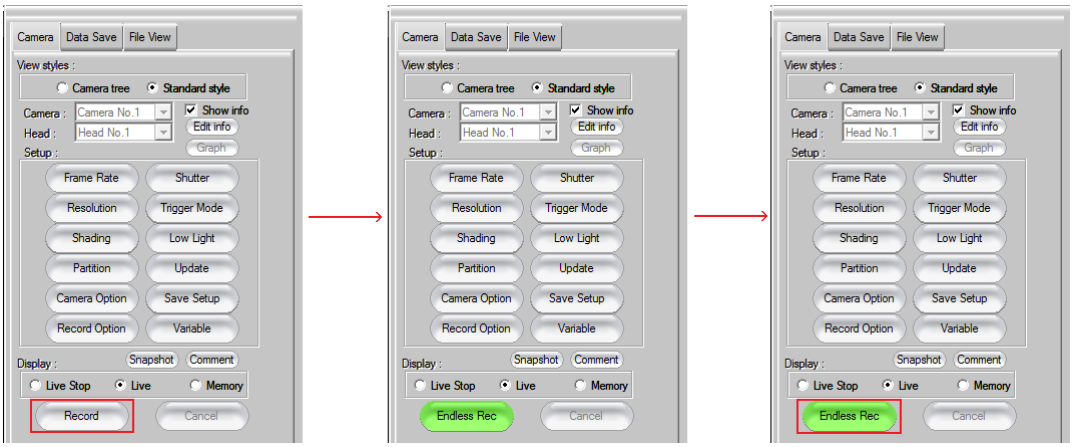

Figure 3.26: The starting and stopping of a record session from the control panel.

to the images, a CIH-file for the playback sequence is also saved in the data folder. The CIH-file can be used to load the image sequence into PFV for later reviews, or opened in a document reader to show a list of caption properties, e.g. framerate and date.

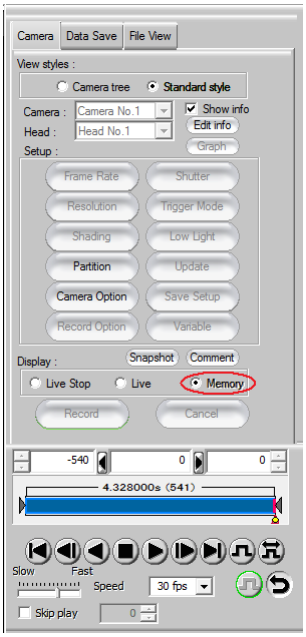

Figure 3.27: The "Memory" mode of the display shown in the control panel.

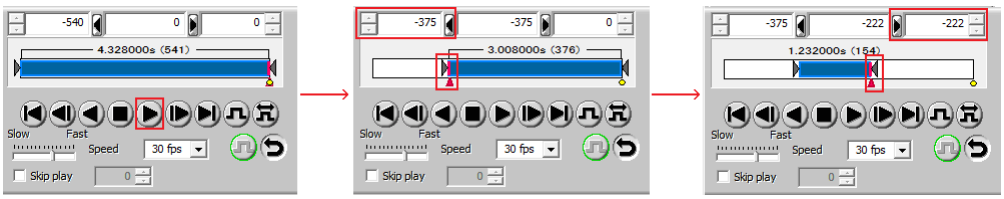

Figure 3.28: Specifying the playback sequence by dragging the start and end frame handles, or by specifying start and end frame numbers directly.

3.6.2 Digital camera and stopwatch

In some experiments, a digital camera is used to obtain some images with greater spatial resolution than obtainable with the fastcam. These images can be used to explore eventual details not observable in the fastcam frames. The camera is also used to document sample preparations by taking time lapse images.

The digital camera used is a Nikon D200 equipped with a Nikon AF Nikkor 20mm 2.8/f lens D200cite. It is a 10.2 megapixel camera with a 23.6x15.8mm RGB CCD image sensor. The D200 is capable of taking JPG images with a resolution up to 3872x2592 pixels, and set at its "fast continuous" shooting mode it is able to capture 37 images with maximum resolution at a rate of 5 fps. The D200 can be connected to a computer through a USB 2.0 interface. If connected to a computer with the program "Camera Control Pro 2" installed and running, captured images will be downloaded directly to the computer disk instead of being stored on a memory card in the camera.

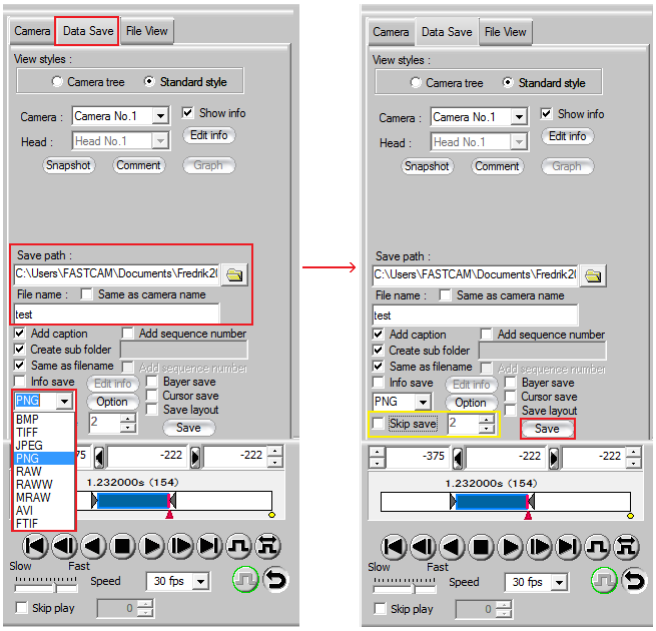

Figure 3.29: The saving process of the captured data.

D200 preparation

The D200 is mounted to a tripod where its platform can tilt, pan and rotate. To position the camera, the lens cap is removed and while looking through the viewfinder, the camera position is adjusted to include the entire sample in the picture frame. The D200 is positioned as directly above the sample as possible without blocking the view of the Fastcam. When the camera is in place, it is connected to the computer through a 2.0 USB "mini to type A" wire. The computer has "Camera Control Pro 2" installed. The camera shooting mode can be selected with a dial on the top left of the D200 3.30, and it is set to "CH" meaning high-speed continuous. The D200 is powered by a power supply and switched on. "Camera Control Pro 2" is started on the computer and the main window, fig. 3.31, shows up. Note that it should be run in "compability mode for Windows XP" if the camera is not detected.

Configurations of image format and size, image optimization and download settings are made. The image format is set to "JPEG (8-bit)" and the size is set to "Large" (3872x2592 pixels) as shown in fig. 3.32, and the image optimization is set to "black-and-white" as shown in fig. 3.33 to download the images as grayscale. The image settings can be saved to a setup file and loaded at later times as shown in fig. 3.34. The download settings however, fig. 3.35, must be configured each time: A suitable download folder is selected or created, a name is chosen for the images and sequential numbering is selected with 4 digits, starting on 0001.

D200 high speed continuous image capturing

The high speed continuous image capturing during experiments is done by manually pressing and holding the shutter release button on the camera 3.30. Increased control is achieved when manually controlling the camera as well as a larger image buffer: 37 images can be taken at

Figure 3.30: The D200 with the shutter release button indicated with a red circle and the mode dial indicated by a yellow circle.

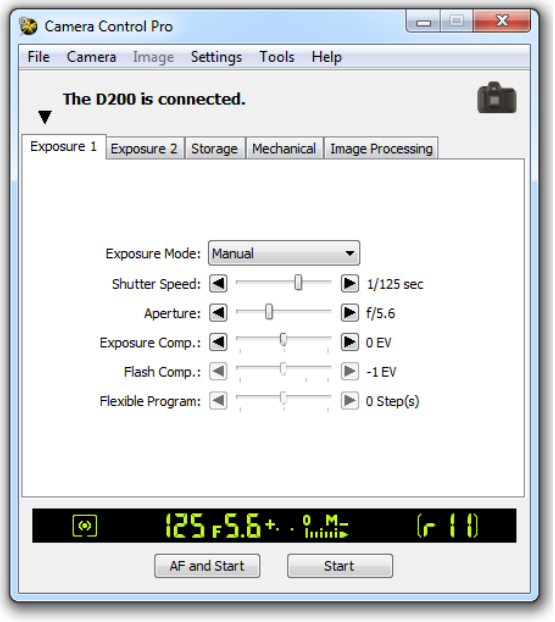

Figure 3.31: The main window in Camera Control Pro. The camera type and some settings are displayed.

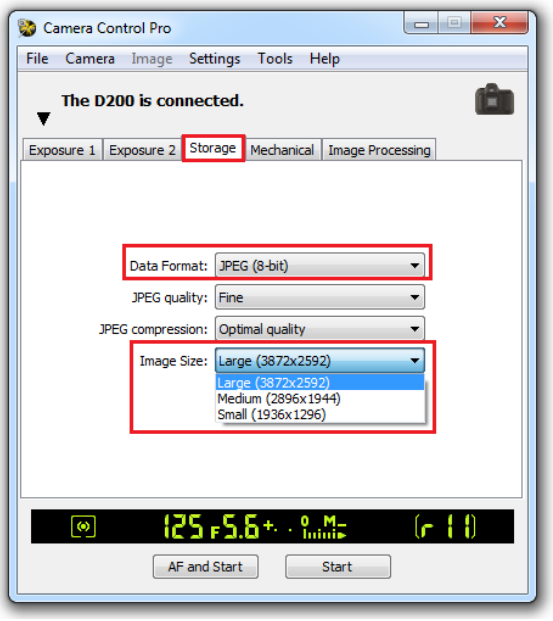

Figure 3.32: The image size is changed by choosing from the drop down box. The same is done for the image file type in the "Data Format" drop down box.

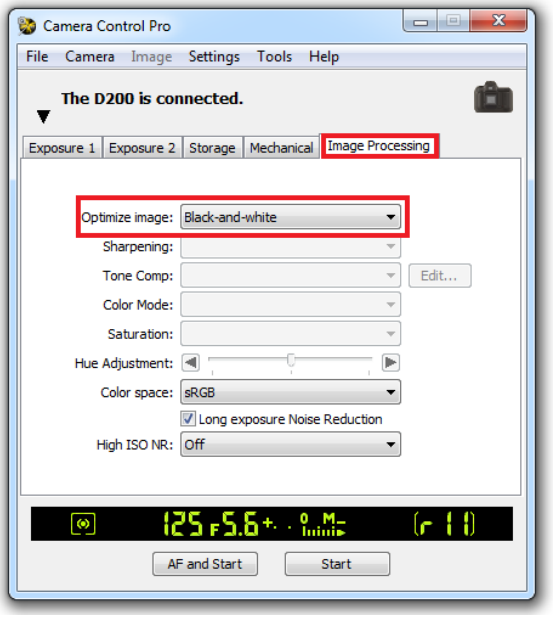

Figure 3.33: The "Optimize image" drop down box is set to "Black-and-white".

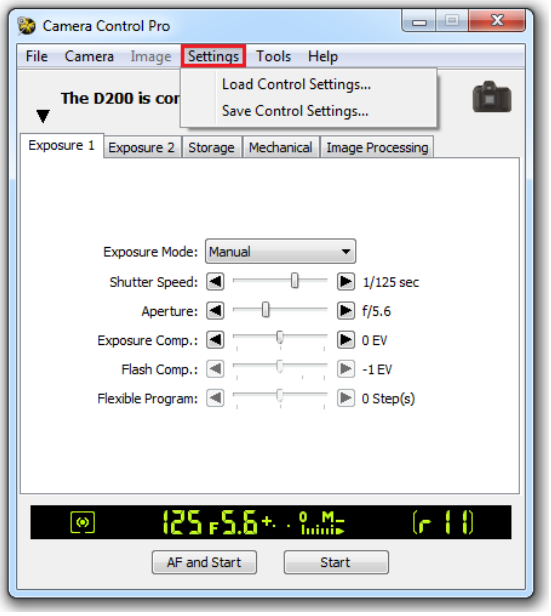

Figure 3.34: Saving and loading of image settings.

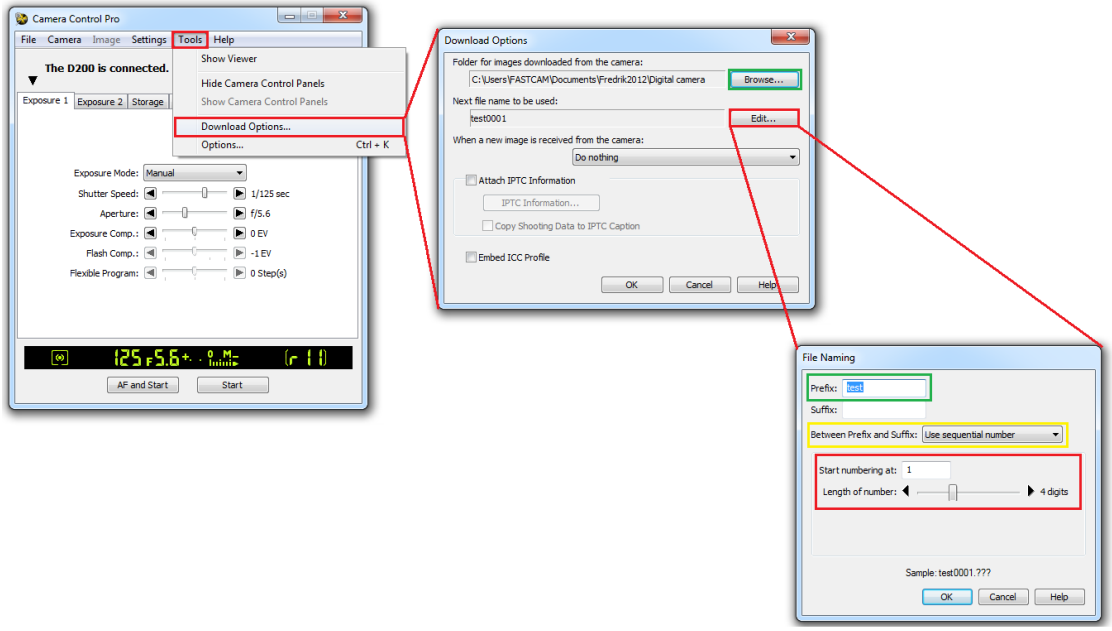

Figure 3.35: Configuration of naming and directory for downloaded images. In the "Download Options" window, the folder is selected by clicking "Browse" (green) and the naming is configured by clicking "Edit.." (red). In the "File Naming" window, the sequence name is defined in the "Prefix" box (green), sequential numbering is selected in the drop down box inside the yellow indicator, and configured with options indicated by the red rectangle.

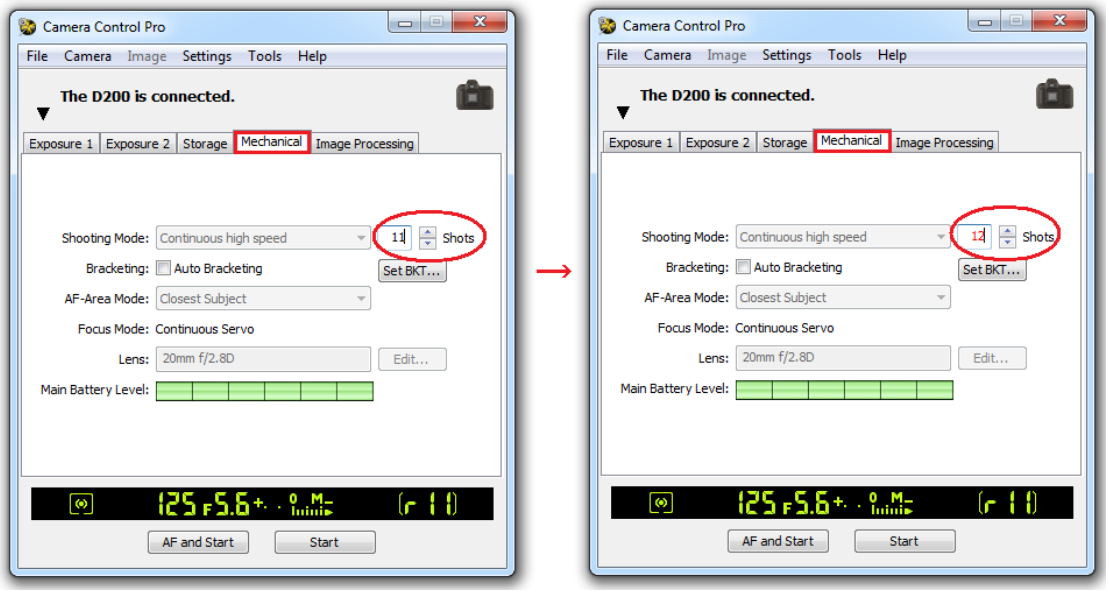

Figure 3.36: When changing predefined number of continuous shot frames from 11 to 12, the program indicates the number 12 in red. This means that the maximum number of high speed photographs possible to download is exceeded.

5fps as opposed to 11 images at 5fps when controlling with "Camera Control Pro 2" D200CITE. Figure 3.36 shows that the maximum length of a computer controlled sequence is 11 photos. Note that the camera must be allowed by the program to be controlled from its body, see fig. 3.37.

D200 time lapse image capturing

The time lapse image capturing is controlled and configured in "Camera Control Pro 2". The time lapse photography function is used for the documentation of a sample preparation process. "Time Lapse Photography" is selected from the "Camera" menu as shown in figure 3.38. "Autofocus before each shot" and "Keep shooting until cancelled" are checked. The delay interval is set to 30 seconds. When the "Start" button is clicked, the camera will take a picture every 30 seconds until the "Stop shooting" button is pressed.

Stopwatch

To link experimental photographs taken with the D200 to frames captured with the Fastcam, a stopwatch is placed in view of both cameras. Before experiments the stopwatch is started to get a timestamp on each frame and photograph captured.

Any digital stopwatch with a display of times down to 1/100 seconds may be used. In addition, the display should be luminating so that the digits are clearly visible by both cameras. The stopwatch function on most smartphones actually satisfy these requirements.

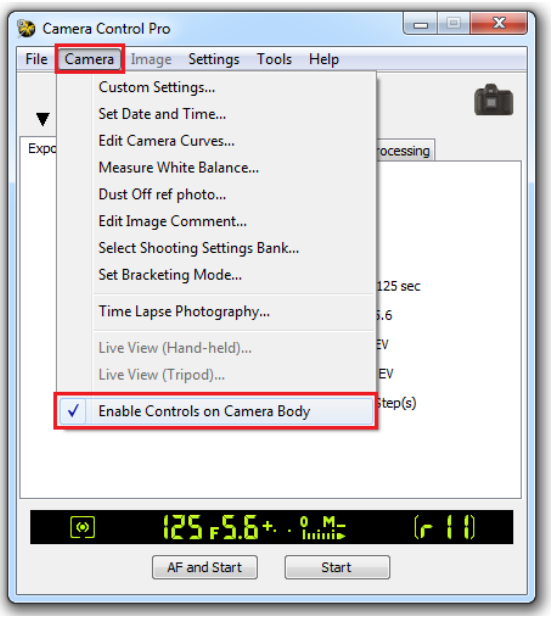

Figure 3.37: Allowing camera body controls.

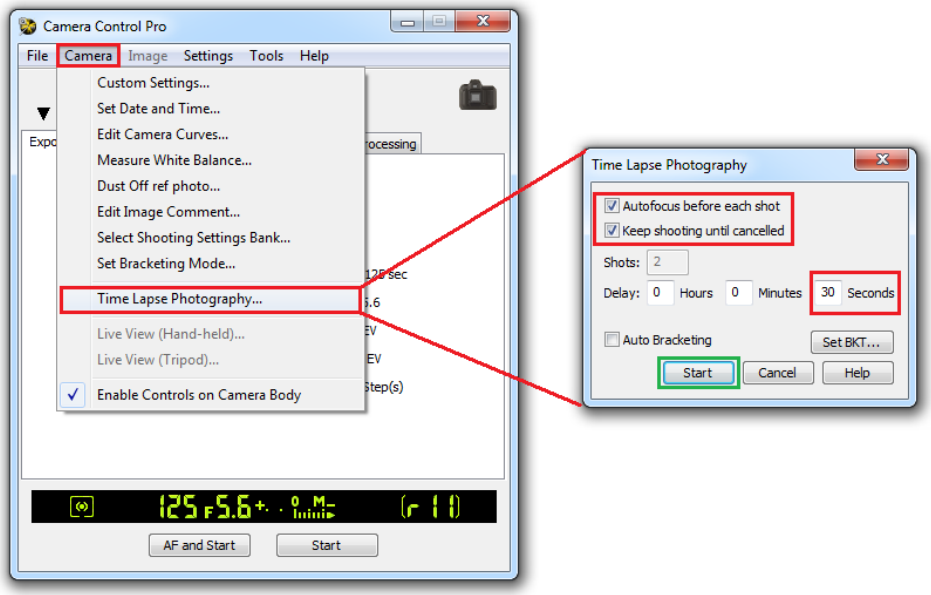

Figure 3.38: Configuring (red) and starting (green) the time lapse image capturing function. After pressing start a window with image information pops up, where a "Stop shooting" button can also be found.

Figure 3.39: The stopwatch as seen with the D200.

The stopwatch used is the stopwatch function on a Samsung Galaxy S I-9000 smartphone. The digits are bright white on a black background, clearly visible for the cameras and shows times down to 1/100 seconds 3.39.

The stopwatch is placed over the frame of the sample holder at a position where it is in view by both cameras.

3.6.3 Computer

The computer used in the experiments is a "Dell Latitude E6510" laptop computer. It features an internal memory of 8GB, an "Intel core i5" 2.67GHz processor and a 250GB hard drive. The installed operation system on the computer is a 64-bit version of "Windows 7 Professional". The laptop has a 10/100/1000 Gigabit Ethernet network card and four USB 2.0 ports.

No relevant application errors or other issues between the computer and cameras have been experienced with this computer setup.

3.7 Sample preparations

3.7.1 The non-deformable porous media sample

The sample of a quasi 2 dimensional non-deformable porous media is built on the sample plate before it is assembled into the sample holder.

Sample plate

The top side of the sample plate is fitted with clear double coated tape. Four tape pieces with lengths of the sample plate diameter are fastened radially across the sample plate, with approximately 45° angle between eachother. Each of the resulting circle segments get 3 tape pieces of about 2cm in length placed evenly along the rim. A sheet of clear contact paper, slightly larger than the sample plate, is fastened to the tape coated surface with the adhesive side facing up. It is important to the 2 dimensional geometry that the contact paper is streched to be wrinkle free. When the contact paper is properly attached, it is trimmed around the sample plate edge. A hole is poked through the contact paper at the hole in the center of the sample plate. The hole can be made with a nail.

Filling of beads

Glass beads are sprinkled over the adhesive surface of the sample plate and are consequently adhering at random positions on the surface. When the entire sample plate surface is covered by beads, the excess beads are shaken off by tilting the sample plate vertically and shaking it. This leaves the sample plate with a monolayer of disorderly placed beads. A second contact paper is fastened on top of the monolayer with the adhesive side down on the beads. This contact paper should also be wrinkle free and trimmed around the sample plate edge, but no hole must be made through it.

The result is a transparent, circular sample of a quasi 2 dimensional disordered and non-deformable porous media with an injection hole in the center. The sample structure can now be assembled as described in section 3.4.5. The sample structure with a non-deformable porous media sample is finished, fig. [figure needed].

Saturation of defending fluid

Two syringes are combined into a 100ml double syringe by the use of small tubing and a "Y" shaped three-way junction. The syringes are connected to the top of the "Y" junction with 3.5cm pieces of small tubing, while the bottom of the junction is connected to a 20cm piece of small tubing. The double syringe is filled with liquid and provides sufficient amount of liquid to saturate the sample. The end of the tubing attached at the bottom of the three-way junction will be referred to as the *liquid supply*.

The liquid supply is connected to the liquid injection tubing of the sample structure. Having made sure that the air injection stopcock is closed, the liquid injection stopcock is opened and the liquid is injected with a careful but steady pressure on the double syringe plungers. The injection is stopped when the sample is saturated, and the liquid injection stopcock is closed.

The non-deformable porous media sample is now saturated by defending fluid and ready for a two phase flow experiment.

Figure 3.40: The assembled deformable porous sample structure. There is a trench between the sample plate and the sample holder frame, which is called the fill trench

3.7.2 The constricted deformable porous media sample

The sample of a quasi 2 dimensional disordered and constricted deformable porous media is built within the assembled sample structure. The particles will be constricted within the model perimeter by an elastic edge on the rim, which is permeable for fluids.

Sample plate

The rim on the top side surface of the sample plate is coated with a belt of polyurethane foam rubber. This belt is the elastic constriction edge, which has an approximate width of 0.8cm and a height of 0.4cm. To control the plate separation, four 1.4mm thick metal spacers are equally separated along the inside of the belt and fastened with double coated tape.

The sample plate is ready and the deformable porous media sample structure is assembled as described in section 3.4.5. Note that the sample plate is oriented such that each assembly clamp is situated at a spacer. The assembled sample structure is shown in fig. 3.40

Filling of beads

To obtain an even monolayer of 1mm glass beads on a smooth surface is a difficult task. This task simplifies greatly if a *beadinjector* is used. The principle of the beadinjector is simple: It uses pressurized air to inject beads through the center hole of the sample plate and into the quasi 2 dimensional sample volume of the assembled sample structure. Due to the plate separation in the sample volume the injected beads will form an approximate monolayer.

The beadinjector is created from a syringe, some tubing and connectors: The plunger tip is removed from the plunger and a hole is poked through its center with a knife. A suitable two-way connector is inserted halfway through the hole in the plunger tip. This makes the removable air inlet of the beadinjector. At the other end of the syringe, the original syringe tip is cut off and replaced by a two-way connector which is cut in half and has larger internal diameter than the syringe tip. This is the bead outlet of the beadinjector, which is connected to a large tubing

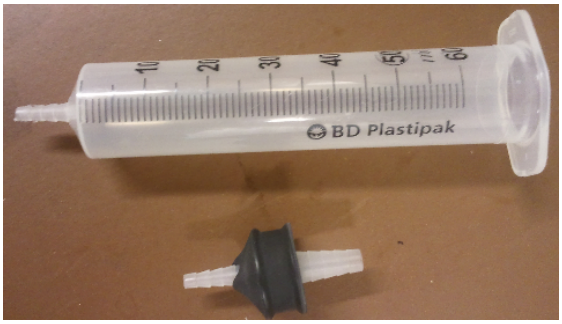

Figure 3.41: The beadinjector shown with its removable air inlet, the replaced syringe tip is a two-way connector which is cut in half.

piece of length 1.2m. The barrel of the syringe is called the beadchamber. The beadinjector is shown in fig. 3.41.

To inject beads, the nipple is removed from the sample plate hole and the beadinjector outlet tube is inserted. Due to the outer diameter of the large tubing, it holds itself in place within the hole. The beadchamber is filled with about 50ml of beads before the removable air inlet is attached by pushing the plunger tip just inside the beadchamber. The air supply is set to about 0.5bar and connected to the air inlet. To avoid blocking the bead outlet when the beadchamber is full, the beadinjector should be held vertically with the bead outlet as the highest point and the air flow should be triggered in pulses. As the amount of beads within the chamber decreases, the blocking risk also decreases. This enables us to gradually apply more continuous air flow and eventually tilt the beadinjector.

The sample volume is between 3 to 4 times larger than the beadchamber, meaning that the filling of the beadinjector and subsequent procedures have to be performed 3 to 4 times. This is actually favorable considering recently injected beads, which are randomly distributed and loosely packed. Most of them are not fully injected to the rim of the available space on the sample plate. This is dealt with each time the beadchamber is empty: Leaving the airflow triggered while knocking gently on the bottom of the sample plate will make the beads "jump" towards the rim and pack together. To make the knocking more effective, a 7.9cm brass cylinder with diameter of 4.4cm is used to knock with. Note that if the knocking is not done, beads may pack together in a central cluster and eventually cause the beadinjector tube to clog up, even if it is available space for beads on the outside of that cluster.

When the sample plate is completely covered by a monolayer of beads, the beadinjector tube in the center hole is replaced by the nipple. This replacement results in a cavity in the center of the sample plate, which must be filled by beads. Knocking the bottom of the sample plate will make beads "jump" back into the cavity due to some slight horizontal "stacking". Filling thid cavity will approximate the wanted monolayer even further.

The constricted deformable porous media sample is created, and ready for the next step in the sample preparation.

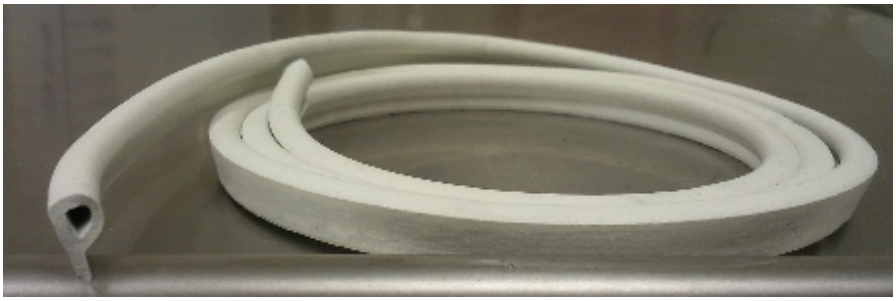

Figure 3.42: The p-seal used to seal the fill trench during saturation.

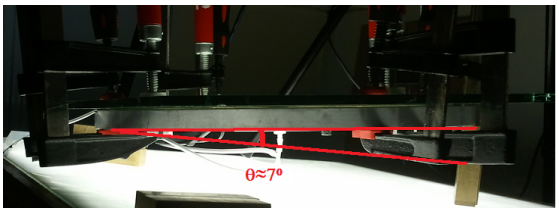

Figure 3.43: The sample structure is tilted $\approx 7^\circ$ during saturation.

Saturation of defending fluid

There are a number of ways to saturate a porous media sample with a fluid. On the other hand, it is difficult to saturate a deformable porous media sample with a viscous liquid without deforming it or get trapped air clusters. However, a successful method was found: Gravity stabilized imbibition. The process takes 30-80 minutes, so it is tedious and time consuming, but it is worth the patience.

First off, the bottom of the fill trench must be sealed. The seal is a p profile rubber seal, often used in doors and windows 3.42. With the help of a 7.5cm nail, it is tucked into the trench going around the entire sample holder frame, starting and ending at the opposite side of the rim injection point. A small separation of about 5mm should be left between the ends of the seal to avoid trapped air during saturation. As the liquid will enter the sample due to the plate separation, it must be made sure that the rubber seal is not tucked too far into the trench, sealing the fill trench from the sample. To avoid drainage through the center hole, it must be made sure the injection tubing is connected with its stopcocks shut.

To control the saturation process by gravity, the model structure must be tilted in a way so that the liquid injection point at the rim is the lowest point. This is achieved by rearranging the support blocks: The lowest point rests on two lying support blocks stacked on top of eachother, and the highest point rests on one standing support block. The result is an approximately 7° incline from the rim injection point to the 5mm gap in the trench seal on the opposite side, fig. 3.43.

Introduction of the liquid is done through the extended syringe connected to the rim injection point, fig. 3.44. The syringe, held above the tilted model structure, is filled with liquid which is injected due to gravity. Hence, without a plunger, the injection flow rate can be controlled by lowering (decreasing) or lifting (increasing) the extended syringe. During the saturation the

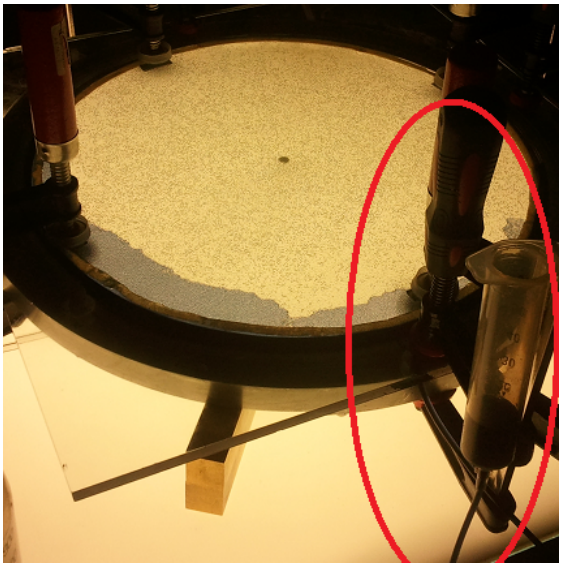

Figure 3.44: The method of saturation is through the extension line. Gravity is the only force to inject the fluid.

syringe barrel has to be refilled when neccesary and before it is drained. It has to be done about 4 times. To avoid trapped air clusters it is important to maintain a low injection flow rate, e.g. if 60 to 80 minutes were spent on saturating a sample with 200ml liquid, the injection flow rate would be 2.5-3.5 ml per minute. Too high injection flow rates will cause liquid to fill the trench, surround the sample plate and prevent air from escaping the sample.

When the sample is saturated, a plunger is carefully inserted as a lid on the injection syringe so it can be put down without spilling the remaining liquid. The sample structure is leveled, and the fill trench rubber seal is removed by picking it out with the nail. During removal of the rubber seal, liquid remaining in the fill trench will pour down on the lightbox surface. This is easily cleaned with a damp cloth.

The deformable constricted porous media sample is now saturated with defending fluid and ready for a two phase flow experiment.

3.7.3 The open deformable porous media sample

The sample preparation of the open deformable porous media sample is very similar to the procedure of the constricted deformable sample, so only the differences will be pointed out.

Sample plate

The sample plate is fitted with the same 1.4mm spacers as for the constricted deformable sample in section 3.7.2, but without the polyurethane constriction belt.

Filling of beads

The filling of beads is done with the beadinjector as in (section 3.7.2), but before the filling of beads it is important to tuck slices of polyurethane into the fill trench to surround the sample plate edge. These slices with about 1cm in height and a thickness of about 0.4cm are tucked in with the nail. Injected beads will escape from the sample plate if this is not done.

Saturation of defending fluid

The saturation of the defending fluid is done with the gravity stabilized imbibition method as in section 3.7.2. Note that when the fill trench seal is removed, the polyurethane slices surrounding the sample plate are picked out as well.

This makes the saturated sample an open deformable porous media sample.

3.8 General experimental procedure

A stepwise walkthrough is given as a short summary of the experimental procedure. The steps are listed in the correct order of the experimental procedure, which is considered to be everything from sample preparation to the stop of the recordings. The use of the D200 camera is optional and steps in parantheses can be ignored in cases without the D200.

The experimental procedure goes as follows:

1. Create the desired 2D porous media sample: Non-deformable, constricted deformable or open deformable.
2. Saturate the sample with liquid using the method required by the sample type, and clean the lightbox surface if necessary.
3. Regulate the air supply to the desired air pressure and connect the air supply to the air injection tubing on the sample structure.
4. Turn on the lightbox, shut off all other lighting in the lab and close the curtains on eventual windows.
5. Configure the high speed camera. (Configure the D200 and place the stopwatch).
6. (Start the stopwatch), Start the Fastcam continuous recording session and trigger the air supply.
7. (Take one reference image with the D200.)
8. (Manually trigger the D200 to shoot "high speed continuous" and immediately) Open the air injection stopcock.
9. Let the air break through the saturated sample.
10. Stop (all) the data capturing.
11. Close the air injection stopcock and cut off the air supply.
12. Save captured data from Fastcam memory to the computer disk (D200 images are directly downloaded to the computer).

3.9 Development of the experimental methods

This section describes the development of the methods used to create a 2 dimensional deformable porous media sample and will help to explain why the sample preparations are performed the way they are.

3.9.1 The development of non-deformable sample preparation

The sample preparation methods used to create a 2 dimensional non-deformable porous media sample have been developed before for similar experiments [4]. However, some trial and error with the sample saturation of defending fluid led to the construction of the double syringe and the injection tubing.

The double syringe was created after an attempt to saturate the sample with only one syringe. The liquid content of one syringe was not enough to fully saturate the sample, but the content of two syringes was. The double syringe was created to avoid injecting air into the sample, which may occur when we disconnect a syringe to refill it.

After liquid saturation of the sample, an attempt of switching the connected liquid supply tubing with the air supply tubing was made. Having to disconnect tubing from the nipple led to liquid drainage, and causing air injection from the rim towards the center of the sample. The injection tubing was made to avoid the need to switch between tubing connected to the sample plate.

3.9.2 The development of constricted deformable sample preparation

Sample preparation methods for the constricted deformable porous media were developed based on the sample preparation methods for the non-deformable porous media sample. Many steps of trial and error led to the final methods used, and these steps will mentioned here.

The sample needed to be a quasi 2 dimensional circular environment wherein beads could be free to move, but prevented to leave at the rim. The constriction on the rim should be permeable to fluids. The initial attempt to solve this was to attach a rubber foam belt to the sample plate rim, carefully pour beads on the sample plate surface and spread them out to an approximate monolayer. The quasi 2 dimensional environment was created by clamping the sample plate to a glass pane. The result is shown in fig. 3.45. Saturation of the defending fluid was done by central injection. Three issues were identified in this initial method: Many of the beads were stuck between the plates, the beads were too loosely packed and the injection of the liquid fluid deforms the sample, fig. 2.12. Solving these issues will lead to the sample preparation methods for the constricted deformable porous media sample.

Solution to the stuck beads problem

Spacers are the solution to the problem with the stuck beads since they are used to control the plate separation. The sample structure was half filled with beads, tilted and shaken to test bead movement for different spacer thicknesses. The ability of beads to move and the vertical stacking of them were evaluated. The 1.4 mm spacers were chosen as the best option due to the approximate monolayer and no stuck beads.

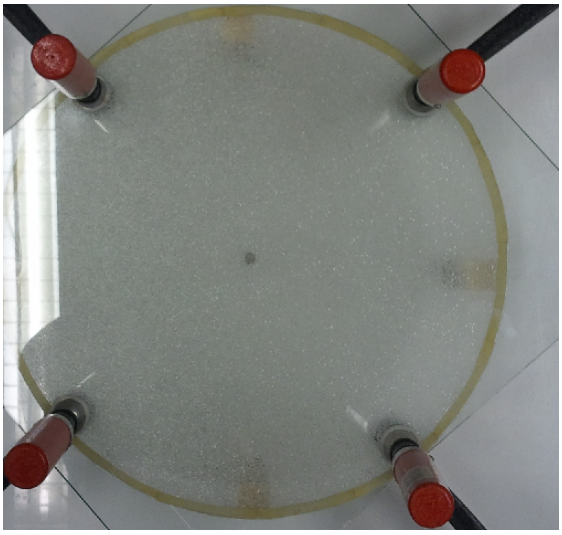

Figure 3.45: The initial method of the deformable constricted sample.

Solution to the beads placing and packing problem

The process of finding an easy and and effective way to place the beads on the sample plate and pack them together can be divided into 3 main attempts. In the first attempt, another circular plexiglass plate with a hole in the center was clamped onto the sample plate. Beads were carefully poured onto the sample plate through the hole in the plexiglass plate and then distributed by shaking and tilting the sample plate while blowing air through the hole with the air supply. The result was a more densely packed monolayer of beads, but it was too time consuming to manually pour beads through the hole. This led to attempt 2, where the beadinjector was developed. It made the bead filling process quick, but the change of plates from the plexiglass plate to the glass pane deformed the monolayer. The third attempt was the direct beadinjection method where the sample plate was clamped to the glass pane, the sample plate nipple removed and the beadinjector used through the center hole of the sample plate.

Solution to the sample deforming liquid saturation problem

The problem where the sample is deformed by the liquid saturation was solved through 4 main attempts. The first attempt was to inject the fluid very slow through the center while paying close attention to the sample. It failed and the injection still deformed the center of the sample. In the second attempt a circular frame was mounted on the sample holder glass pane before the sample plate was attached and filled with beads. With the sample structure upside down, this frame made it possible to pump liquid from the rim to the center of the sample plate. The liquid was filled into the fill trench between the sample plate and the frame, and pumped towards the sample center with the double syringe. When the sample was saturated, the entire sample structure was flipped quickly over. Unfortunately, the flipping caused air bubbles and sample deformation along the sample rim. The third attempt was to saturate the sample from the rim while it was inside the sample structure standing the right way. This was done by sealing the fill trench and filling it through the frame via the syringe extension. Imbibition of liquid from

the fill trench nearly saturated the sample, but some air was trapped. The solution was finally found in attempt 4, where the third attempt was reproduced with the sample structure slightly inclined to maintain a straight imbibition front, saturating the sample completely.

3.9.3 The development of open deformable sample preparation

The sample preparation method of the open deformable sample is basically the same as for the constricted deformable except for one important detail: the sample plate is without constriction on the rim.

Knowing that the beads had to be prevented from leaving the sample plate during the filling of beads and saturation of liquid, the idea of tucking foam rubber pieces into the fill trench as described in was tested. It proved to be successful.

3.10 Image processing and analysis of raw data

The raw data from experiments is in the form of PNG and JPG images. Before these data can be analyzed properly, some image processing has to be performed. The image processing may include operations like removal of background noise, conversion to binary images, trimming of edges and resizing of images. After image processing, the data is saved and may be analyzed.

The program used for this is Matlab. This powerful program is suitable for image processing, saving and analyzing data alltogether. Matlab has features such as commands for image processing that are easy to learn and use, it can perform a large variety of calculations on images, it reads and writes many file types and we can make our own standard programs for repeated use.

The specific commands and scripts used in data analysis of the experiments are explained further in appendix A.

Chapter 4

Analytical methods

4.1 Estimation of fluid properties and flow parameters

4.1.1 Density

A BLAUBRAND density bottle is used for fluid density estimations. The bottle has a specified volume which is printed on the side of the bottle with a precicion of 10^{-3} cm^3. At the top it has a glass stopper with a capillary along its axis.

The measurement process is as follows:

1. The empty density bottle with the glass stopper is weighed, and the scale is zeroed at that weight.
2. The glass stopper is removed, and the density bottle is filled with the fluid in question.
3. The glass stopper is inserted. Excess fluid will be ejected through the capillary.
4. The outside of the density bottle and glass stopper is wiped clean.
5. The full density bottle is weighed on the scale, giving the weight of its fluid contents in grams.

Knowing both the volume and the weight of the fluid, estimation of the fluid density is performed using eq. (2.4).

4.1.2 Viscosity

Viscosity is estimated by the help of an Ubbelohde capillary viscometer [figure needed]. The viscometer used is manufactured by Schott Geräte with Type No. 52520 and Capillary No. II. The capillary I.D is 1.03mm and the viscometer has a kinematic viscosity measurement range of 20mm^2/s to 100mm^2/s [8].

The process of the viscosity measurement is as follows, fig. 4.1 shows the numbered parts of the viscometer:

includegraphics[scale=0.5, keepaspectratio=true]viscometer.png

Figure 4.1: Schematics of the Ubbelohde Viscosimeter [8].

1. Fluid is filled into the reservoir (4) through the filling tube (3). Filling capacity is indicated by minimum and maximum marks (10) on the reservoir.
2. The venting tube (1) is covered with a finger.
3. Suction is applied to the capillary tube (2) by a syringe connected via large tubing. This will cause the successive filling of the reference level vessel (6), the capillary (7), the measuring sphere (8) and the pre-run sphere (9).
4. Suction is discontinued, the syringe is disconnected and the venting tube (1) is opened again.
5. The flow time is measured as the time it takes for the fluid meniscus to descend from the upper timing mark (M1) to the lower timing mark (M2). Note that it is important that the capillary is vertically aligned.
6. Steps 1-5 are repeated several times to get an average flow time $\bar{t}$.

The kinematic viscosity ν is found by the equation

$$\nu = K \cdot (\bar{t} - \vartheta), \tag{4.1}$$

where K is a constant of the viscometer and ϑ is the Hagenbach-Couette (HC) correction time [8].

When matching a viscosimeter to the viscosity of a fluid, the minimum flow time should be $t = 200$s. For long flow times, $\bar{t} > 200s$, the HC correction time has so small values that it can be neglected and eq. (4.1) reduces to

$$\nu = K \cdot \bar{t}. \tag{4.2}$$

The constant K is posted on the viscometer and is $K = 0.09149$.

4.1.3 Surface tension

Surface tension values of different fluids can be found from tabulated measurements [9]. The surface tensions γ for aqueous glycerol solutions to air are listed in table 4.1. The measurements were made at room temperature, 25°C.

4.1.4 Wettability

The wettability of the liquids on the materials in the sample can be determined visually. By placing a small liquid droplet of radius $r \sim 1$mm on a smooth surface of a solid, its wetting properties can be observed visually. An approximation to the contact angle between the solid and the liquid is made by taking a picture along the surface of the solid, and use that photo to determine the contact angle as shown in fig. 2.6.

Glycerol by weight [%]	Surface tension, γ [mN/m]
0	72.0
10	70.5
20	69.5
30	68.5
40	67.9
50	67.4
60	66.9
70	66.5
80	65.7
90	64.5
100	62.5

Table 4.1: Surface tensions of various aqueous glycerol concentrations to air at 25°C.

4.1.5 Compressibility

To determine whether the compressibillity of a fluid should be considered or not, one can start with considering if the fluid is subject to external pressure changes uniformly over its surface that may change its density. If it is not, the compressibility can be neglected simply because there are no compression or decompression. If it is, eq. 2.7 can be used to check the significance of the compression/decompression, and to decide if the fluid can be rendered compressible or incompressible.

4.1.6 Volume flow rate

The volume flow rate Q of an invasion is estimated by evaluating the sequence of N flow pattern images with Matlab. The program asks for user input of timestep of the frames and plate separation. The program counts the number of pixels that adds to the cluster between each frame, which corresponds to a increment in a volume of air per timestep as

$$\frac{dV}{dt} = Q_k = \frac{a_0 b(N_i - N_{i-1})}{dt}, \tag{4.3}$$

where the intervals $k = 1, 2, ..., N-2$ between the frames $i = k+2$ are chosen in order to avoid a spike in Q which appears between the first and second frame which are not separated by the same timestep as the other frames. Here, a_0 is the pixel area, dt is the duration of the intervals between the frames, N_i is the number of pixels in frame i and b is the plate separation.

The program uses the calculated information and the user input to approximate the actual volume flow rate in units [cm^3/s] at the precision of the pixel size and framerate.

4.1.7 Darcy velocity

The Darcy velocity is estimated as the volume flow per area of the average front as

$$v_k = \frac{Q_k}{A_k}, \tag{4.4}$$

where Q_k is the volume flow rate from eq. (4.3) and A_k is the area of the average displacement front in the interval k.

Since the porous media sample is circular and the flow origins from the center, the average displacement front is assumed to be at a circle of radius $R_{g,k}$ centered at the injection point. Here, $R_{g,k}$ is the radius of gyration of the observed growth in the interval k. Then, the area of the average displacement front in the k-th interval is given by

$$A_k = 2\pi R_{g,k} b, \tag{4.5}$$

where b is the plate separation. From eq. (4.4), we have the Darcy velocity on the k-th interval as

$$v_k = \frac{Q_k}{2\pi R_{g,k} b}. \tag{4.6}$$

It is found that Q_k has a linear relationship to A_k, such that the average Darcy velocity can be found in regression analysis of a plot of Q vs. A.

The Matlab program which calculates the volume flow rate in the previous section is modified to also calculate A_k. Then, the Darcy velocity is estimated from a regression analysis of the results.

4.2 Sample characterization

4.2.1 Porosity

An estimate of the porosity of the two dimensional samples can be obtained visually with Matlab. Some areas of the samples are out of sight or has poor contrast, so to make the estimate as accurate as possible, a clearly visible area of interest is selected as a sample area of the porous media which is assumed to have similar overall properties. The area of interest is selected in Matlab, and should be as large as possible.

To estimate the porosity of a porous media sample based on the area of interest, the program listed in [appendix] enhances the contrast of the beads in order to define the pore space, as in fig. 4.2, which it then divides with the total area of interest to get the porosity given by eq. (2.1). The porosity given for the sample is considered a rough approximation to indicate the ratio of pore space to the total volume of the actual porous media.

4.2.2 Randomness

The randomness of the pore neck widths in the sample can be indicated by the distribution of nearest (and next nearest) neighbor distances as shown in figures 2.3 and 2.4. To estimate the distribution of nearest neighbor distances and thus the pore neck width distribution, a Matlab program is used where it enhances the beads to obtain nearly all of their "mass centers" as seen

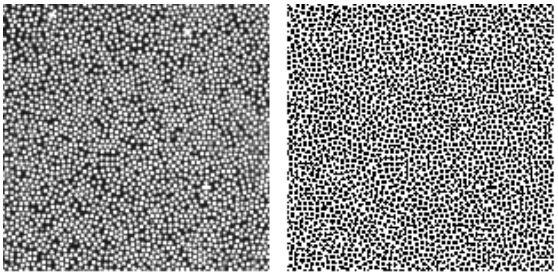

Figure 4.2: A portion of a porous media sample (left) and the corresponding estimated pore space (right) shown in white.

in fig. 4.3. When the positions of most of the bead centers are known, the program makes a list of the 10 nearest neighbor distances between every known point and plots the result in a histogram. The fundamentals of the counting at each point is explained in fig. 4.3. The resulting histogram has two peaks, see fig. 5.4, where the left peak indicates the nearest surrounding particles and the right peak the second nearest surrounding particles. The top of the left peak indicates the typical pore neck size, and the width of the left peak indicates the spread of pore neck widths. Another indication of organization is the sharpness of the left and right peaks, i.e. the more distinct they are the more organized is the particle distribution.

4.2.3 The sample and pore sizes

Sample size is fixed at 40cm in diameter for ND and DO and 39cm for DC, i.e. on the order of 10^{-1}m. Typical pore size is assumed from the left peak of the bead distribution plot and assigned a with a metric value corresponding to the pixel size, on the order of 10^{-3}m. The metric value corresponding to a pixel in the frames is found to be $d_p = 0.4mm$. The value d_p was found by comparing the radius of all samples in pixels and divide it by the metric radius of the samples.

4.3 Experimental analysis

4.3.1 Flow pattern and fractal dimension

Initial characterization of the growth pattern can be done visually, by looking at certain characteristics such as finger thickness and amount of trapped clusters of defending fluid.

The fractal box counting dimension of the growth pattern can be used to quantitatively describe its spatial occupation in the plane of the image. The box counting dimension is found in Matlab by counting the number of boxes necessary to cover all the points of the pattern at different box sizes, and solve eq. (2.28).

The fractal box counting dimension is also counted for the perimeter of the pattern, to estimate how "wiggly" it is on the resolution of the experiments.

To describe the arrangement of mass distribution (fingering) versus distance from injection center of the invasion patterns, the fractal mass dimension is calculated. This is done by calculating eq. (2.36) for $r_{min} < r < R_g$ with Matlab. The program is listed in [appendix] , and determination

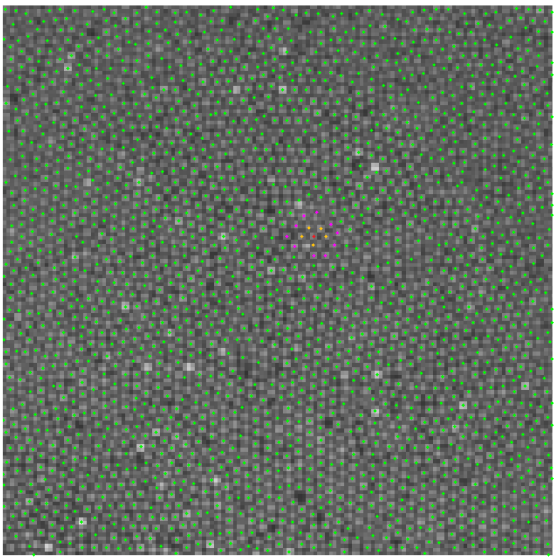

Figure 4.3: A portion of a porous media sample with most of the "mass centers" of the beads indicated by green points. The red point shows what happens when its ten closest neighbor distances are counted: All the distances of the points forming the closest ring (orange) around the red point are counted. Then some of the distances of the points forming the second closest ring (magenta) are counted.

of $r_{min} > R_0$, where the pixels (monomers) forms smooth shapes, was done by creating filled circles of increasing pixel radius r, and by comparing the area A_N given by the number of pixels and the area $A_r = \pi r^2$, a radius $r_{min} = 2^4$ was selected as where the areas $A_N \approx A_r$ [figure needed].

The program which calculates the number-radius relation for the patterns is actually calculating the mass dimension of multiple growing patterns in each experiment. The patterns are instants of the growing cluster at different times $t_i \leq t_0$, separated by equal time intervals dt. Since the radii are $r_{min} < r < R_{g,i}$ for each investigated pattern, we can use that $f(r/R_{g,i}) = f_{c,i}$ is constant in this region and collapse the data from all clusters i in a plot as $log(N(r)/N_{0,i}f_{c,i})$ vs. $log(r/R_g)$ If the resulting plot shows a definite linear relationship with slope D, the clusters are scale invariant with mass dimension D.

If it is discovered that the patterns are not scale invariant over all cluster sizes in the experiment, the number-radius relation of the breakthrough pattern is plotted. From this plot it is possible to identify separate regions between given $log(r/R_g)$ where the number-radius relation may be linear or not linear, and from this get a conclusion.

4.3.2 Growth statistics and multifractal growth

To determine if the growth of flow patterns in the experiments has multifractal behavior, a program written in Matlab subtracts subsequent frames of a growing cluster taken at instants t_i and t_{i-1} separated by a time interval dt. The subtracted frames reveals the observed growth in time intervals $[0 < t_i - dt, t_i \leq t_0]$.

From the sequence of i frames containing the observed growth on the corresponding time intervals, we obtain the gyration radii of the observed growth clusters $R_{g,i}$, the number of growth islands $N_{I,i}$ and the masses of the growth islands $\mu_{j,i}$. The time interval dt is chosen as a fraction of the breakthrough time, $dt = xt_0, \quad x < 1$. With the same relative time interval, observations in different experiments of the same category can be though of as similar sets of observations. This enables us to consider the common growth properties at different time intervals for the different categories of experiments, i.e non-deformable, constricted deformable and open deformable.

To evaluate if the new growth measure is fractal, partially fractal or fractal at all at a given time interval, a plot of $log(N_i)$ vs. $log(r/R_{g,max})$ is evaluated where $R_{g,max}$ is the gyration radius of the largest growth island structure. As for the mass dimension, eventual linear or non-linear regions can be identified.

When the evaluation of the new growth measure is complete, $\tau(q)$ is found by inserting the observed values $\{\mu_j, i\}$ into equation (2.53) for each set of observations from each frame i. Having $\tau(q)$, $\alpha(q)$ and $f(\alpha)$ is found by equations ([equations]). Plots for the different relations, $\tau(q)$ vs.q, $\alpha(q)$ vs.q and $f(\alpha)$ vs.α, are plotted with different time intervals to investigate the effect of time resolution on observations.

4.3.3 Particle motion

All, or many of the beads forming the deformable porous media samples are displaced during the invasion of air. It is of interest to analyze the dynamics of the particle motion. One of the ways to perform such analysis is to look at the sequence of frames manually and compare the frames to find trends of the particle movement. Another way to analyze the motion of the particles is to process the experimental image sequence in a PIV program.

PIV is short for *Particle Image Velocimetry*. The principle is to track particle movements over a sequence of images to obtain a velocity field of the particles between every frame. PIV is used to analyze the flow of fluids seeded with tracer particles. The method can also be used to track the particles in the deformable porous media experiments, so that the bead displacement dynamics can be analyzed.

The basic operation method of PIV is:

1. The current and previous images are split into small squares called interrogation areas.
2. Each interrogation area of the current image is cross-correlated pixel by pixel with the corresponding interrogation area in the previous image. The correlation peaks indicate particle displacement vectors.
3. Accurate measures of the displacement vectors are found with sub-pixel interpolation.
4. A full velocity field is mapped over the image area as displacement in all interrogation areas are calculated.

4.4 Statistics and evaluation of experimental measurements

This section is a short reminder on how experimental data should be handled, estimated and presented.

4.4.1 Significant figures and uncertainty

Every experimental measurement has an uncertainty associated with it. The uncertainty arises from the measuring device and the skills of the observer. The uncertainty of a measurement is reflected by its number of significant figures, which are all the digits we know for sure plus a last digit which contains some uncertainty. Some rules to identify significant figures are:

- Non-zero digits are always significant figures.
- All zeros between significant figures are also significant.
- The leftmost non-zero digit is called the most significant figure.
- The rightmost digit of a decimal number, or the rightmost non-zero digit of an integer, is called the least significant figure.

The number of significant figures of a measurement is the number of digits counted from and including the most significant figure to and including the least significant figure.

Uncertainty in calculations

The result of a calculation involving measurements with uncertainties will inherit an uncertainty in some way depending on the calculation [10]. Some common rules are:

- Addition or subtraction: The uncertainty of the result is determined by the precision of the least precise measurement, i.e. the result should have the same number of digits after the decimal point as the measurement with the least amount of digits after the decimal point (if any).
- Multiplication or division: The result should have the same number of significant figures as the measurement with the lowest number of significant figures.

The calculations themselves can be carried out with the original numbers as long as the result is rounded to and presented with the amount of significant figures required by these rules.

Significant figures can be lost in certain calculations, e.g. $70.063 - 70.002 = 0.061$. Both numbers involved in the subtraction have 5 significant figures, but the difference has only 2. However, the precision stays the same.

Sometimes, numbers involved in calcuations are exact rather than approximate. They do not have an associated uncertainty and can be thought of as a numbers with an infinite number of significant figures (infinite precision). This is true for defined quantities or pure numbers. As an example, if we perform a measurement n times, n is a pure number.

4.4.2 Experimental measurements and representation of uncertainty

Assume the quantity x, which we want to estimate, is measured n times in n independent and equal measurements. To represent an estimate of the true x-value, the following is a common method [11]:

The mean value of the measurements is assumed to be close to the true value, and is estimated as

$$\bar{x} = (1/n) \sum_{i=1}^{n} x_i. \tag{4.7}$$

Then, we calculate the standard deviation from the mean value

$$\sigma = \sqrt{\frac{\sum_{i=1}^{n} (x_i - \bar{x})^2}{n-1}}, \tag{4.8}$$

which roughly tells us about the spread of x-values around $\bar{x}$. If the probability distribution for x is normal, which is reasonable for large n, it is approximately 62.3% probable that an x-measurement falls within $x \pm \sigma$. Therefore, an estimate of the expected x-value is written as

$$x = \bar{x} \pm \sigma. \tag{4.9}$$

Now, consider the equation

$$\sigma_m = \sigma/\sqrt{n}, \tag{4.10}$$

which gives the standard error σ_m. The standard error is the standard deviation of $\bar{x}$, and roughly indicates how the $\bar{x}$-value will fluctuate around the actual true value x_t,

$$\bar{x} = x_t \pm \sigma_m. \tag{4.11}$$

Note that the accuracy of the estimates increases as the number of measurements n increases, so that when $n \to \infty$, $\bar{x} \to x_t$.

Based on this, we represent parameters estimated from measurements on the form

$$x = \bar{x} \pm \sigma_m, \tag{4.12}$$

where the precision of the uncertainty σ_m is rounded to the precision of $\bar{x}$. However, the probability of measuring an $\bar{x}$-value in the interval given by (4.12) is about 68.3%. It is said that the equation has a 68% confidence interval.

In science, it is common to express an estimated value within a 95% confidence interval [11]. This is done by multiplying the standard deviation (or the standard error) with a number c corresponding to the desired confidence interval, giving the probable error

$$PE = c \cdot \sigma. \tag{4.13}$$

The number c is independent of the values of $\bar{x}$ and σ and is the same for all normal distributions. Hence, the values of c for given confidence intervals can be found in tables, which states $c = 1.95996$ for a 95% confidence interval.

Combining the probable error of a 95% confidence interval with eq. (4.12), we have the estimate of a parameter x to be

$$x = \bar{x} \pm 1.95996 \cdot \sigma_m, \tag{4.14}$$

with the probability of 95% to be a correct estimate.

4.4.3 Regression analysis

A common task in science is to identify and analyze relationships between quantities that vary. Experimental measurements often produces points $(x_1, y_1), ..., (x_n, y_n)$ which seem to lie on a line when plotted in a graph. By regression analysis of such sets of points we want to define a line which lies as close to these points as possible in order to characterize their linear relationship [12].

The linear equation

$$y(x) = \beta_0 + \beta_1 \cdot x \tag{4.15}$$

produces a line with slope β_1 which intersects the y-axis at $y = \beta_0$.

Assume we have fitted eq. (4.15) to a set of data points which lie approximately on a line as in figure [figure needed]. Then $y(x_j)$ gives the predicted value of y for a certain point x_j, while y_j is the actual observed value of y for x_j. The residual at a point is defined as the difference between its observed value and its predicted value,

$$\epsilon_j = y_j - y(x_j). \tag{4.16}$$

The sum of the squares of the residuals of a set of points is considered a way of measuring how close the fitted line lies to the observations. To make the line produced by eq. (4.15) to be as close to the observed measurements as possible, a method called *least-squares* are used to determine the best regression coefficients β_0 and β_1. In other words, the least-squares line is the line with the regression coefficients that minimizes the sum of the squares of the residuals.

Because the measurements are considered to only have errors in the y-coordinates, this line is also referred to as the line of regression of y on x.

An easy way to obtain the regression coefficients of the least-squares line is to use linear algebra [12]. First, assume a set of points which lie exactly on a line such that $(x_1, y_1), ..., (x_n, y_n) = (x_1, \beta_0 + \beta_1 \cdot x_1), ..., (x_n, \beta_0 + \beta_1 \cdot x_n)$. This system can be written as

$$X\vec{\beta} = \vec{y}, \qquad \text{where } X = \begin{pmatrix} 1 & x_1 \\ 1 & x_2 \\ \vdots & \vdots \\ 1 & x_n \end{pmatrix}, \quad \vec{\beta} = \begin{pmatrix} \beta_0 \\ \beta_1 \end{pmatrix}, \quad \vec{y} = \begin{pmatrix} y_1 \\ y_2 \\ \vdots \\ y_n \end{pmatrix}. \tag{4.17}$$

Usually, as we know, experimental measurements do not lie on an exact line, which means eq. (4.17) has no solution and becomes a least-squares problem. The square of the distance between the vectors $X\vec{\beta}$ and $\vec{y}$ is precisely the sum of the squares of the residuals, hence computing the least-squares solution of eq. (4.17) will yield the regression coefficients of the least-squares line for the measured points.

The least-squares solution of eq. (4.17) is computed by finding the normal equations

$$X^T X\vec{\beta} = X^T\vec{y}, \tag{4.18}$$

and rearrange them to find

$$\vec{\beta} = (X^T X)^{-1}X^T\vec{y}. \tag{4.19}$$

The regression coefficients are given by $\vec{\beta} = \begin{pmatrix} \beta_0 \\ \beta_1 \end{pmatrix}$, and by inserting them into eq. (4.15) we get the least-squares line.

4.4.4 Evaluation of the regression line

As mentioned above, the least-squares regression coefficients gives information about the intersection of the y-axis (β_0) and the slope of the line (β_1). When these values are of interest in analysis, it should be taken into account that they are associated with some uncertainty.

The standard deviation of n measured y-values about their least squares line is given by

$$\sigma_{ls} = \sqrt{\frac{\sum_{i=1}^{n}(y_i - y(x_i))^2}{(n-2)}} = \sqrt{\frac{\sum_{i=1}^{n}\epsilon_i^2}{(n-2)}}. \tag{4.20}$$

When knowing the standard deviation about the line, the standard error of the slope can be found as

$$\sigma_{le} = \frac{\sigma_{ls}}{\sqrt{\sum_{i=1}^{n}(x_i - \bar{x})^2}}. \tag{4.21}$$

Assume we have computed a least-squares line and want to estimate a quantity b_0 from β_0 and a quantity b_1 from β_1. Then, equations (4.20) and (4.21) are calculated in order to represent the results with 95% confidence intervals:

$$b_0 = \beta_0 \pm 1.95996 \cdot \sigma_{ls}, \tag{4.22}$$

and

$$b_1 = \beta_1 \pm 1.95996 \cdot \sigma_{le}. \tag{4.23}$$

Coefficient of determination and the Pearson correlation coefficient

The coefficient of determination r^2 and the Pearson correlation coefficient r can be calculated as indications of how good the linear equation explains the variance of experimental measurements [13]. The coefficient of determination indicates how much of the original variance of the points $(x_1, y_1), ...(x_n, y_n)$ that are explained by the least-squares line. It is given by

$$r^2 = \frac{\sum_{i=1}^{n}(y_i - \bar{y})^2 - \sum_{i=1}^{n}\epsilon_i^2}{\sum_{i=1}^{n}(y_i - \bar{y})^2}, \tag{4.24}$$

and gives the fraction of the original variance that is explained by the linear behavior. The remaining fraction of the original variance accounts for variations due to other unexplained factors.

The Pearson correlation coefficient is given by

$$r = +\sqrt{r^2} \quad \text{or} \quad r = -\sqrt{r^2}, \tag{4.25}$$

where its sign is determined by the slope of the regression line. If the slope is positive, we have direct correlation and r is positive. If the slope is negative, we have inverse correlation and r is negative. For $|r| > 0.8$ the correlation is considered strong, while for $|r| < 0.5$ the correlation is considered weak. A perfect correlation of $r = \pm 1$ only happens if all the data points lie on the regression line.

Chapter 5

Experimental data and analytic results

A total of 41 experiments were performed. Most of them were trial and error attempts and led to 10 experiments considered successful. Of the 10 successful experiments 2 are with a non-deformable porous sample, 4 are with a constricted deformable porous sample and 4 are with an open deformable porous sample. The successful experiments and their parameters are listed in table 5.1. Results of analyses will be presented in this chapter, starting with fluid analysis followed by sample characterization, flow parameter derivations, presentation of the particle image velocimetry results and an initial presentation of pattern and growth fractal dimensions.

Experiment	Air pressure [mbar]	Framerate [fps]	D200 used	No. of frames	Breakthrough time, t_0 [s]
ND1	25	250	No	2430	9.72
ND2	25	250	No	2267	9.07
CD25	25	125	Yes	962	7.70
CD50	50	125	Yes	323	2.58
CD75	75	125	Yes	169	1.30
CD100	100	125	Yes	114	0.91
OD25	25	125	Yes	516	4.13
OD50	50	125	Yes	221	1.77
OD75	75	125	Yes	119	0.95
OD100	100	125	Yes	160	1.28

Table 5.1: Parameters for the successful experiments. The non-deformable experiments are referred to as ND1 and ND2. The constricted deformable experiments are referred to as CD25, CD50, CD75 and CD100, where their numbering indicates the injection pressure in mbar. The same numbering is used for the open deformable experiments: OD25, OD50, OD75 and OD100.

5.1 Fluid characterization

Four different batches of defending fluid was used in the successful experiments. They will be referred to as *L1*, *L2*, *L3* and *L4*. The various fluid properties are estimated as described in section 4.1 and presented in this section. Table 5.2 summarizes the results.

Fluid	*L1*	*L2*	*L3*	*L4*
Density, ρ [g/cm^3]	1.124	1.125	1.126	1.126
Kinematic viscosity, ν [mm^2/s]	37.74±0.50	40.08±0.34	41.37±0.32	40.90±0.32
Surface tension, γ [mN/m]	65.7	65.7	65.7	65.7
Wettability with sample, θ [degrees]	< 90	< 90	< 90	< 90

Table 5.2: Summary of the properties of the defending fluids.

Density

Results of the density measurements are shown in table 5.3

Fluid	Mass, m [g]	Volume, V [cm^3]	Density, ρ [g/cm^3]
L1	57.35	51.017	1.124
L2	57.41	51.017	1.125
L3	57.44	51.017	1.126
L4	57.43	51.017	1.126

Table 5.3: Density measurements of the four defending fluids.

Kinematic viscosity

Ten flow time measurements was done for each fluid shown in table 5.4.

Fluid: *L1*										
Measurement	t_1	t_2	t_3	t_4	t_5	t_6	t_7	t_8	t_9	t_{10}
Flow time [s]	423	424	428	405	404	408	409	412	407	405
Fluid: *L2*										
Measurement	t_1	t_2	t_3	t_4	t_5	t_6	t_7	t_8	t_9	t_{10}
Flow time [s]	431	434	446	430	435	439	439	439	439	449
Fluid: *L3*										
Measurement	t_1	t_2	t_3	t_4	t_5	t_6	t_7	t_8	t_9	t_{10}
Flow time [s]	439	450	452	449	451	459	458	454	455	455
Fluid: *L4*										
Measurement	t_1	t_2	t_3	t_4	t_5	t_6	t_7	t_8	t_9	t_{10}
Flow time [s]	440	450	451	436	445	449	449	451	454	445

Table 5.4: Ten flow time measurements for the liquids

Statistics of the flow times for the different fluids are calculated as described in section 4.4, shown in table 5.5.

As seen in table 5.5, all the average flow times are much longer than 200 seconds. Hence we will use eq. (4.2) to calculate the kinematic viscosity from the average flow times. The results are shown in table 5.6.

Fluid	Avg. flow time, $\bar{t}$ [s]	Standard deviation, σ [s]	Standard error, σ_m [s]	Prob. error, PE [s]
L1	412.5	9.0	2.8	5.5
L2	438.1	6.0	1.9	3.7
L3	452.2	5.7	1.8	3.5
L4	447.0	5.5	1.8	3.5

Table 5.5: Statistics of the measured flow times for the viscosity estimation of the four fluids.

Fluid	Avg. flow time, $\bar{t}$ [s]	Viscosimeter constant, K [mm^2/s^2]	Kinematic viscosity, ν [mm^2/s]
L1	412.5±5.5	0.09149	37.74±0.50
L2	438.1±3.7	0.09149	40.08±0.34
L3	452.2±3.5	0.09149	41.37±0.32
L4	447.0±3.5	0.09149	40.90±0.32

Table 5.6: Results of the kinematic viscosity estimations for the four fluids.

Surface tension

The liquid fluids used in our experiments are all mixtures of close to 80% glycerol and 20% water. By looking at table 4.1 we can assume that all our fluids have a surface tension of γ=65.7mN/m.

Wettability

The materials used in samples are plexiglass (sample plate), glass (beads and deformable porous media sample holder plate) and plastic (contact paper in the non-deformable porous media samples). It was found that the liquids (L_1,L_2,L_3,L_4) were wetting on all such surfaces. Since the wetting properties of all liquids seemed similar, it was assumed that an approximation of the contact angles of one liquid would be sufficient to describe the wetting properties of all the liquids. Figure 5.1 shows the wetting properties of three droplets on a glass surface, plastic surface and a plexi glass surface. From fig. 5.1 it is approximated that the contact angle between the liquid and glass is $\theta_g \approx 30°$, the contact angle between the liquid and plastic contact paper is $\theta_c \approx 68°$ and the contact angle between the liquid and plexiglass is $\theta_p \approx 52°$.

Compressibility

The air supply can be considered as a reservoir of air with constant pressure $p > p_0$, where p_0 is the pressure of the atmosphere outside the sample. The temperature T is considered to be constant. As the air reservoir is connected to the sample center, the defending fluid experiences a pressure gradient and starts flowing radially outwards according to Darcy's law. Consequently,

Figure 5.1: The contact angles between aqueous glycerol in air and: Plexiglass (left), plastic (middle), glass (right).

it leaves a void behind where air invades from the reservoir due to the constant internal pressure p. In other words, the volume of the invading air cluster depends on the number of air molecules N needed inside the sample to maintain the constant air pressure of the reservoir. It can be seen by considering the ideal gas law with constant pressure and temperature,

$$pV = Nk_BT \quad \rightarrow \quad V \sim N, \tag{5.1}$$

where k_B is the Bolzmann constant. Since the air supply exchanges particles with the air cluster, it follows that the air is not subject to compression or decompression during experiments with a constant pressure air supply. At breakthrough however, the surface of the air cluster breaks and there is a decompression as $p \rightarrow p_0$.

Being a liquid, the defending fluid can be considered to be incompressible as mentioned in section 2.1.2. In addition, it is not confined and would probably not be subject to any compression or decompression anyways.

5.2 Characterization of the samples

The porosities, typical pore neck sizes and the spread of pore neck sizes of the different samples is estimated as described in section 4.2. Note that in the case of the deformable porous samples, this charaterization is only valid prior to the invasion of air. Estimates for all samples are listed in table 5.7, figure 5.2 shows the nearest neighbor histograms for the non-deformable samples, figure 5.4 shows the nearest neighbor distance histograms for the constricted deformable samples and figure 5.6 shows the nearest neighbor distance histograms for the open deformable samples.

Sample	Porosity, ϕ	Typical pore size, a [mm]	Spread of pore sizes [mm]
ND1	0.55	1.26	$\pm$0.25
ND2	0.55	1.27	$\pm$0.25
CD25	0.54	1.13	$\pm$0.13
CD50	0.54	1.26	$\pm$0.25
CD75	0.54	1.26	$\pm$0.25
CD100	0.54	1.26	$\pm$0.25
OD25	0.54	1.27	$\pm$0.25
OD50	0.54	1.27	$\pm$0.25
OD75	0.54	1.27	$\pm$0.25
OD100	0.54	1.27	$\pm$0.25

Table 5.7: These estimated parameters for the porous media samples are based on raw data images.

The indication of randomness in the non-deformable samples is confirmed visually, see fig 5.3, there is no apparent organization of the particles.

The figure 5.5 shows a region of the sample used in CD25 and a region of the sample used in CD75. The indications of pore neck organization for the constricted deformable samples seems to be confirmed.

As seen in fig. 5.7, the indications of some degree of organized particle distribution in the open deformable samples is confirmed visually.

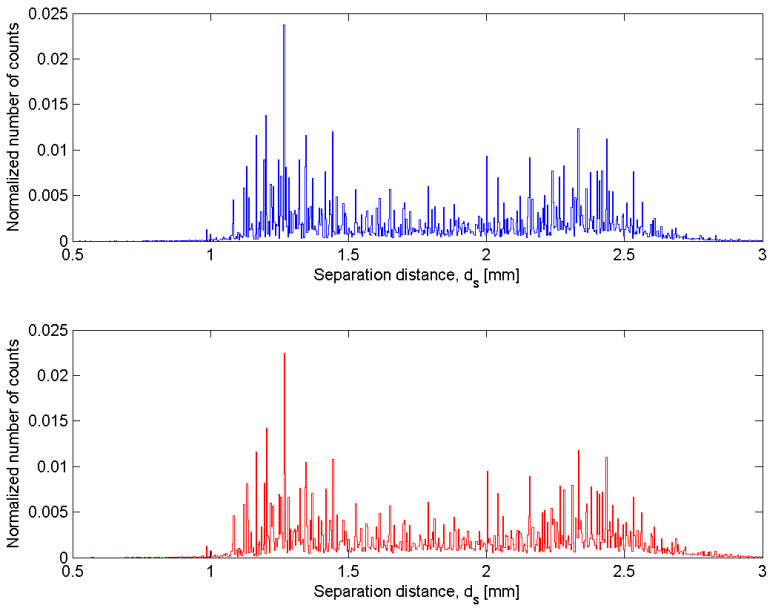

Figure 5.2: Histogram of the 10 nearest neighbor distances for ND1 (blue) and ND2 (red). The left peaks indicate the typical pore neck size and the spread of distances around them indicate the pore neck size distribution. Note how diffuse the right peaks are, they are almost blending in with the left peaks. This indicates disorder of particle positions in the sample.

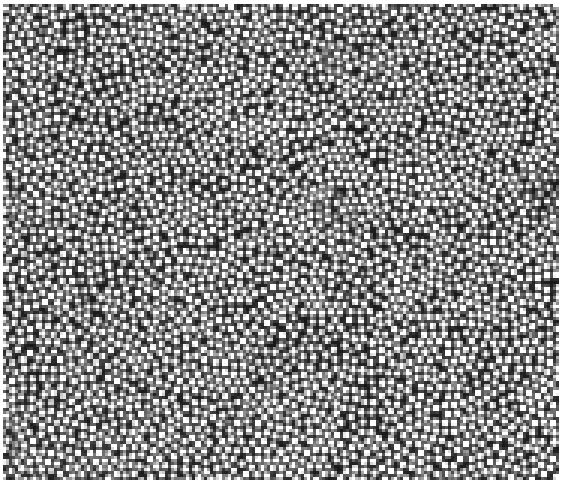

Figure 5.3: An area from the porous media used in experiment ND1. The indications of randomness seems to be well supported by this image.

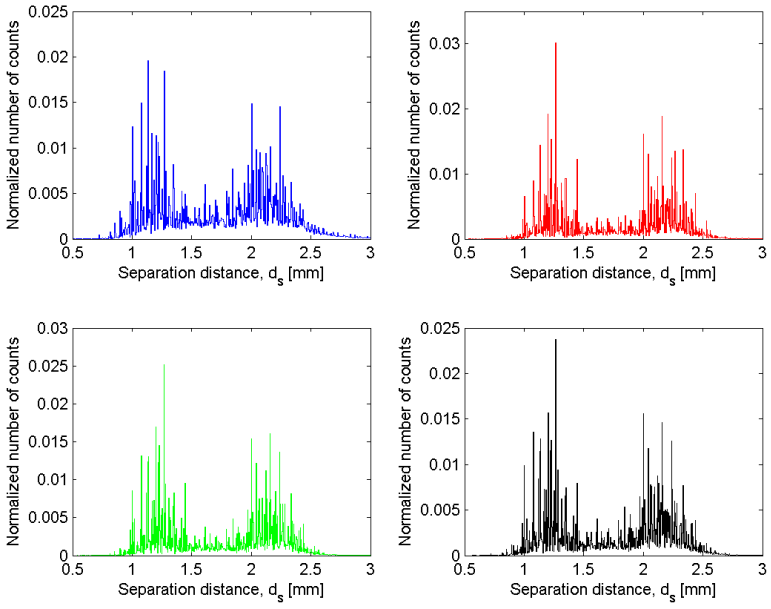

Figure 5.4: Histograms of the initial 10 nearest neighbor distances in the area of interest for the constricted deformable porous media samples: CD25 (blue), CD50 (red), CD75 (green) and CD100 (black). The typical pore size is indicated by the left peaks and the distribution of pore sizes are indicated by their widths. Note how distinct the left and right peaks are, indicating some degree of order between the particle positions. The sample in CD25 is indicated to be more close packed, but more disordered than the other constricted deformable samples.

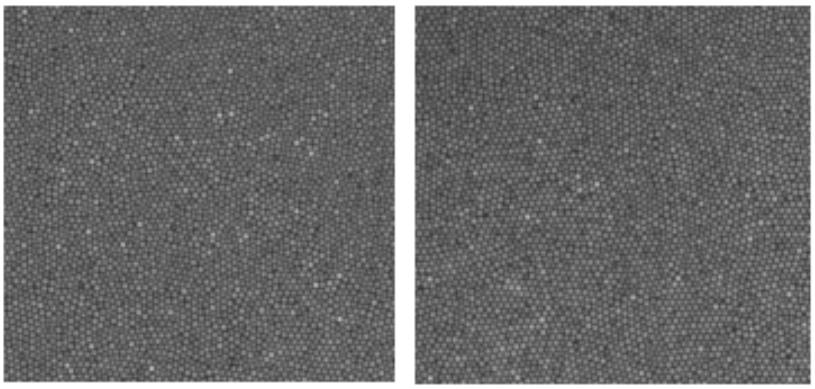

Figure 5.5: Areas from the porous media used in experiments CD25 (left) and CD75 (right). The particle positions seems more organized than for the non-deformable porous media, as the particles tend to form hexagonal close packed clusters. If we look closely, even the indication that the CD25 sample is more disordered than the other can be seen as it looks more like an amorphous pack of particles while the CD75 sample looks like a polycrystal with hexagonal close packed domains.

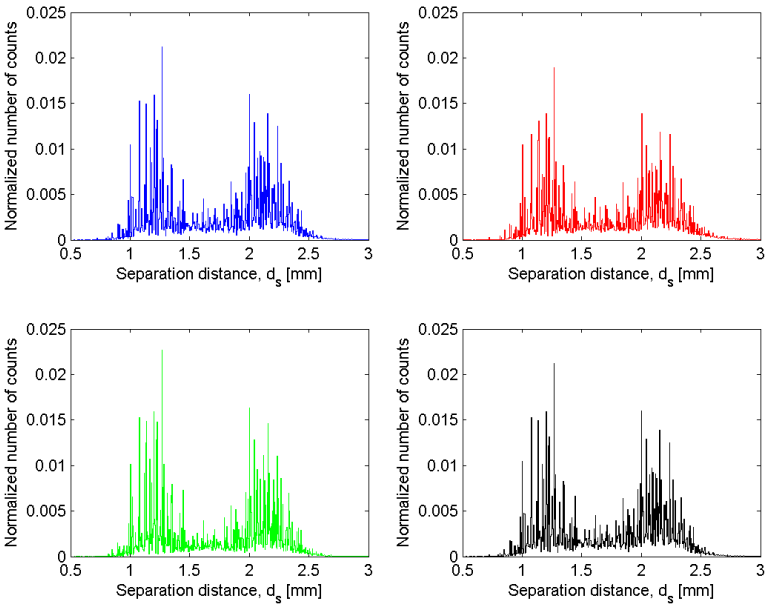

Figure 5.6: Histograms of the initial 10 nearest neighbor distances in the area of interest for the open deformable porous media samples: OD20 (blue), OD50 (red), OD75 (green) and OD100 (black). The left peaks indicate the typical pore neck size of the samples, and their widths indicate the spread of pore neck sizes. The left and right peaks are distinct, indicating some degree of organization of the particles.

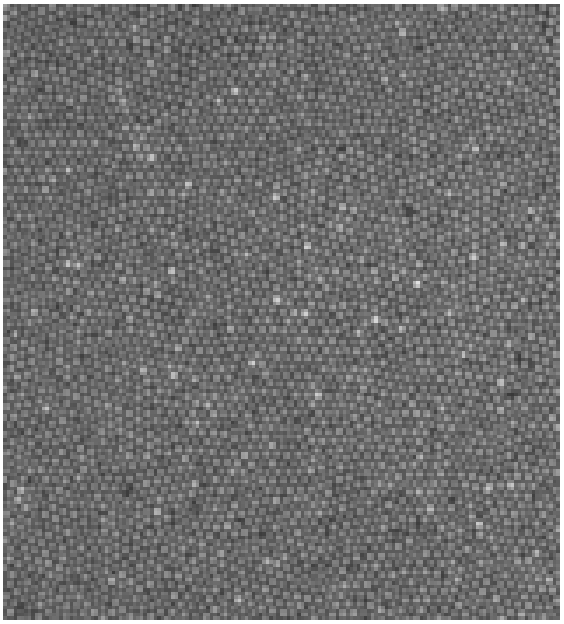

Figure 5.7: Area from the porous media used in OD100. The particle positions seems similarly organized as in a polycrystal with hexagonal close packed domains.

5.3 Estimation of flow parameters

Volume flow rate

The volume flow rate is estimated as explained in section 4.1. An example plot of the results is found in figure 5.8, which shows that the volume flow rate Q increases as the gyration radius of the average front increases.

Since the volume flow rate is increasing, it will be described in terms of the Darcy velocity and radius of gyration as shown in table 5.8.

Darcy velocity of the average front

The Darcy velocity is estimated for the average front as described in section 4.1. The calculated results are listed in table 5.8. An example of the plots of Q vs. A used to estimate v is shown in fig. 5.9.

5.4 Obtained velocity fields of particles in deformable porous media samples

The PIV program was used to process all frame sequences of deformable porous media experiments as described in section 4.3.3. The frames was analyzed at their framerate of 125fps, giving

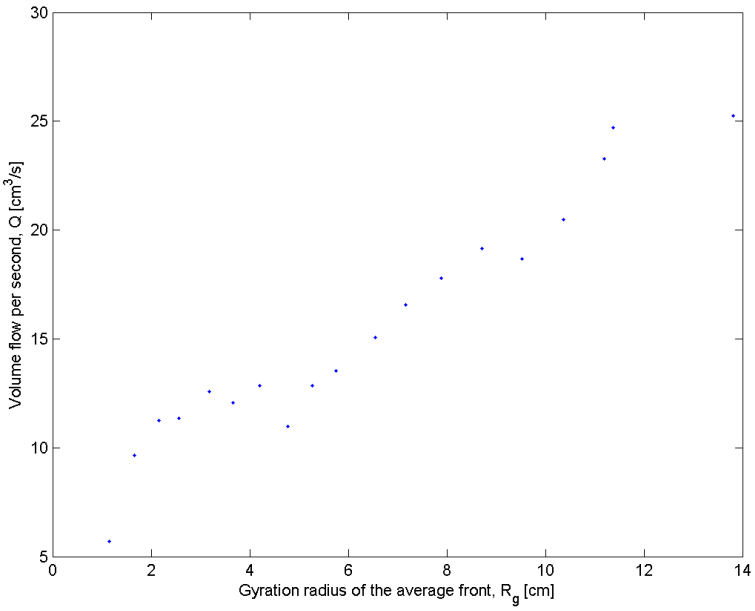

Figure 5.8: An example taken from observations in OD75 with intervals of 48ms between the frames. Note how the volume flow rate increases with the increasing gyration radius of the growing cluster.

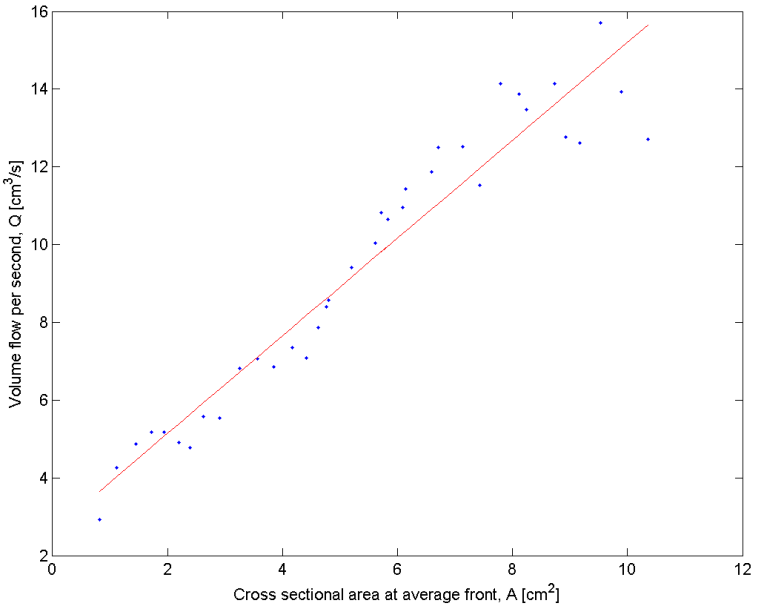

Figure 5.9: This plot of Q vs. $A = 2b\pi R_g$ is taken from observations in OD50 (blue) with frames separated by 48ms. The slope (red) of the fit is estimated as the Darcy velocity of the average displacement front, as $v = Q/A$.

Exp.	$c\sigma_{ls}$, [cm^3/s]	$c\sigma_{le}$, [cm/s]	r^2	r	Darcy vel., v [cm/s]	Vol. flow rate, Q [cm^3/s]
ND1	0.14	0.01	0.968	0.984	0.16±0.01	$2b\pi rv + 0.12$
ND2	0.25	0.02	0.931	0.965	0.19±0.02	$2b\pi rv + 0.11$
CD25	0.48	0.04	0.761	0.872	0.14±0.04	$2b\pi rv + 1.51$
CD50	1.46	0.13	0.830	0.911	0.55±0.13	$2b\pi rv + 4.17$
CD75	2.06	0.23	0.936	0.968	1.14±0.23	$2b\pi rv + 7.31$
CD100	6.07	0.56	0.850	0.922	2.07±0.56	$2b\pi rv + 6.61$
OD25	1.36	0.12	0.778	0.882	0.34±0.12	$2b\pi rv + 2.20$
OD50	1.88	0.23	0.929	0.964	1.26±0.23	$2b\pi rv + 2.63$
OD75	2.60	0.37	0.942	0.971	1.60±0.37	$2b\pi rv + 6.48$
OD100	5.37	0.41	0.918	0.958	2.50±0.41	$2b\pi rv + 3.64$

Table 5.8: Results for the regression analyses on Q vs. A, giving the Darcy velocities of the average fronts in the experiments. Due to the relationship between Q and A, the linear trend of the volume flow rate is given in terms of v, radius of the average front r and the plate separation b.

a detailed time resolution of bead velocity fields during an experiment. Limiting factors creating uncertainty are the image resolution and contrast.

As mentioned, the PIV method is primarily designed for flow analyses on seeded fluids, but some of the extracted data of the program may be useful such as the area average of the velocity magnitude per frame, the velocity field per frame and velocity magnitude plot per frame, see figure 5.10.

5.5 Initial dimension characterization of flow patterns

As described in section 4.3.1, we calculate the mass dimension of the patterns, as well as the box counting dimension for the patterns and their perimeters.

5.5.1 Flow patterns in non-deformable porous media

Tables 5.9 and 5.10 shows the results of the regression analyses on the number-radius relation for ND1 and ND2. The number-radius relations for growing clusters at different times are also plotted together to check for scale invariance, as in figure 5.11.

Timestep, dt [s]	$c\sigma_{ls}$	$c\sigma_{le}$	r^2	r	Mass dimension, D
1	0.06	0.02	0.994	0.997	1.57
0.5	0.06	0.01	0.994	0.997	1.57
0.1	0.06	0.01	0.994	0.997	1.57

Table 5.9: Results of the mass dimension regression analysis for the observations in ND1 for different time resolutions, where smaller timestep between frames leads to more datapoints.

The fractal box dimensions are calculated for intermediate box sizes with the results posted in tables 5.11 and 5.12.

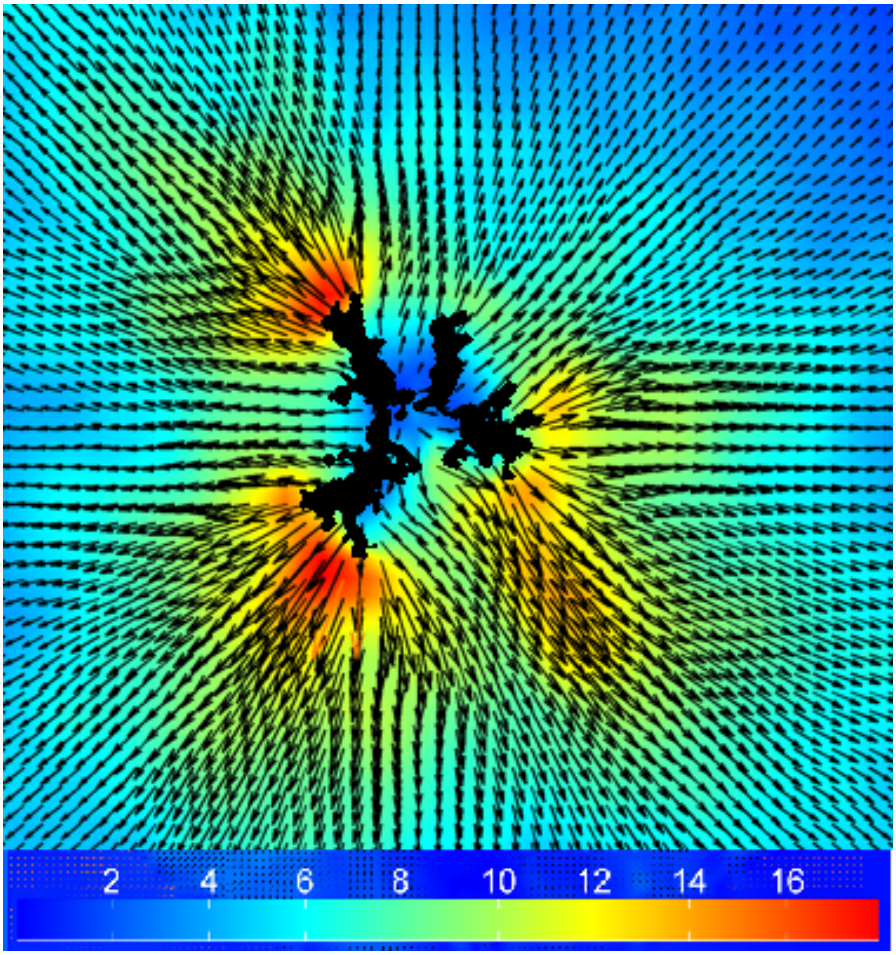

Figure 5.10: The velocity magnitude [mm/s] indicated in colors and exaggerated black arrows is indicating the velocity field of the beads in frame 26 of OD50. The invading air cluster is shown in black, and the time interval is $dt = 0.008$s.

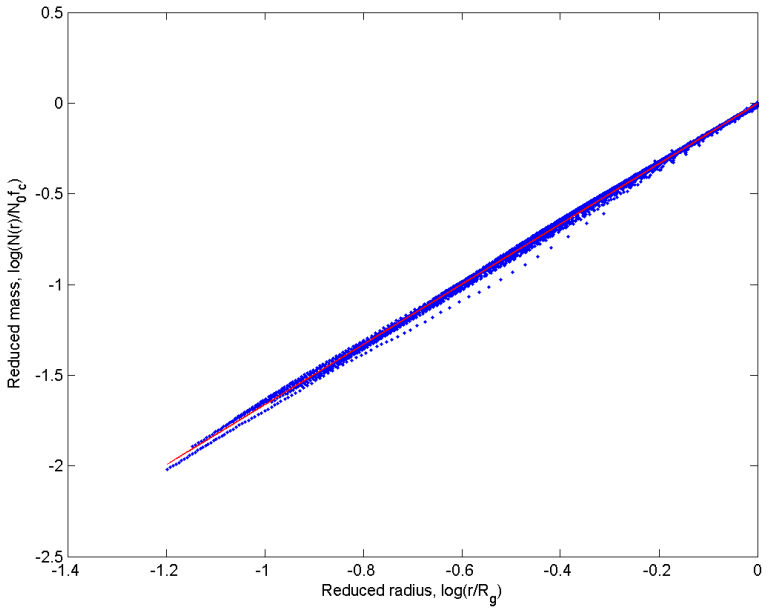

Figure 5.11: Plot of $log(N(r)/N_0 f_c)$ vs. $log(r/R_g)$ for observations in ND2. The timestep is 0.1s, and the datapoints (blue) are collapsed data from 85 subsequent frames of the growing structure. The least squares line (red) is also plotted with the fractal mass dimension $D = 1.66$ for the growing clusters. The clean, straight line is evidence of scale invariance.

Timestep, dt [s]	$c\sigma_{ls}$	$c\sigma_{le}$	r^2	r	Mass dimension, D
1	0.03	0.01	0.999	≈ 1	1.66
0.5	0.03	0.01	0.999	≈ 1	1.66
0.1	0.03	0.01 >	0.999	≈ 1	1.66

Table 5.10: Results of the mass dimension regression analysis for the observations in ND2, where smaller timestep between frames leads to more datapoints.

Structure	$c\sigma_{ls}$	$c\sigma_{le}$	r^2	r	Box dimension, D
Perimeter	0.02	0.02	0.999	≈ -1	1.53
Pattern	0.03	0.02	0.999	-0.999	1.53

Table 5.11: Results from box counting of the breakthrough pattern as well as its perimeter for ND1.

Structure	$c\sigma_{ls}$	$c\sigma_{le}$	r^2	r	Box dimension, D
Perimeter	0.02	0.02	0.999	≈ -1	1.55
Pattern	0.02	0.02	0.999	≈ -1	1.56

Table 5.12: Results from box counting of the breakthrough pattern as well as its perimeter for ND2.

5.5.2 Flow patterns in constricted deformable porous media

The mass dimensions of growing clusters are calculated with results listed in tables 5.13, 5.14, 5.15 and 5.16. The number-radius relations for growing clusters at different times are also plotted together to check for scale invariance as in figure 5.12.

Timestep, dt [s]	$c\sigma_{ls}$	$c\sigma_{le}$	r^2	r	Mass dimension, D
1	0.12	0.04	0.982	0.991	1.66
0.5	0.12	0.03	0.982	0.991	1.66
0.1	0.12	0.01	0.981	0.991	1.66

Table 5.13: Results of the mass dimension regression analysis for the observations in CD25 for different time resolutions, where smaller timestep between frames leads to more datapoints.

Timestep, dt [s]	$c\sigma_{ls}$	$c\sigma_{le}$	r^2	r	Mass dimension, D
0.5	0.12	0.05	0.987	0.993	2.04
0.1	0.12	0.02	0.987	0.994	2.05
0.05	0.12	0.02	0.987	0.994	2.06

Table 5.14: Results of the mass dimension regression analysis for the observations in CD50, where smaller timestep between frames leads to more datapoints.

The fractal box dimensions for both the patterns and their perimeters are calculated for intermediate box sizes and posted in tables 5.17, 5.18, 5.19 and 5.20.

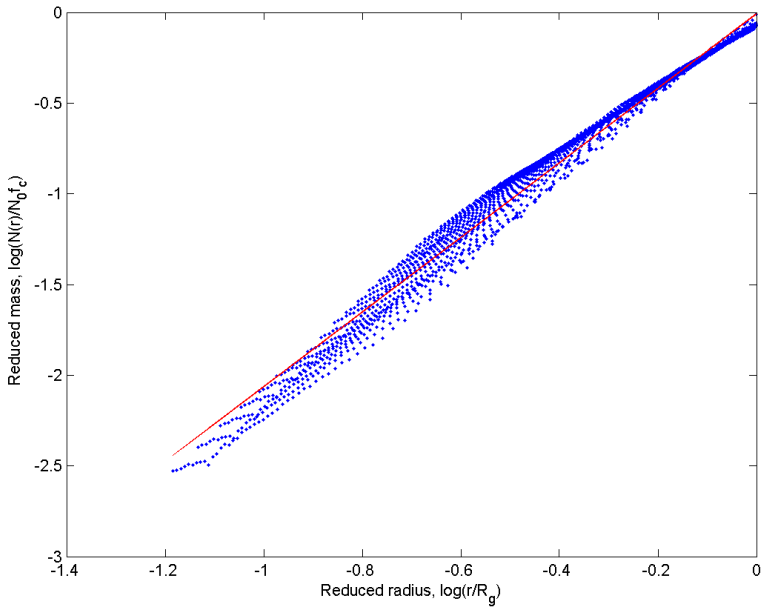

Figure 5.12: Plot of $log(N(r)/N_0 f_c)$ vs. $log(r/R_g)$ for observations in CD50. The timestep is 0.05s, and the datapoints (blue) are collapsed data from 52 subsequent frames of the growing structure. The least squares line (red) is also plotted with the a calculated fractal mass dimension $D = 2.05$ for the cluster. From the looks of this combination of number-radius relations for the growing cluster, the cluster is not scale invariant.

Timestep, dt [s]	$c\sigma_{ls}$	$c\sigma_{le}$	r^2	r	Mass dimension, D
0.5	0.18	0.09	0.967	0.983	1.80
0.1	0.18	0.04	0.968	0.984	1.82
0.05	0.17	0.03	0.968	0.984	1.82

Table 5.15: Results of the mass dimension regression analysis for the observations in CD75, where smaller timestep between frames leads to more datapoints.

Timestep, dt [s]	$c\sigma_{ls}$	$c\sigma_{le}$	r^2	r	Mass dimension, D
0.5	0.07	0.04	0.995	0.997	1.79
0.1	0.10	0.03	0.990	0.995	1.83
0.05	0.09	0.02	0.991	0.995	1.83

Table 5.16: Results of the mass dimension regression analysis for the observations in CD100, where smaller timestep between frames leads to more datapoints.

Structure	$c\sigma_{ls}$	$c\sigma_{le}$	r^2	r	Box dimension, D
Perimeter	0.02	0.02	0.999	≈ -1	1.59
Pattern	0.02	0.02	0.999	≈ -1	1.58

Table 5.17: Results from box counting of the breakthrough pattern as well as its perimeter for CD25.

Structure	$c\sigma_{ls}$	$c\sigma_{le}$	r^2	r	Box dimension, D
Perimeter	0.02	0.01	≈ -1	≈ -1	1.64
Pattern	0.02	0.01	≈ -1	≈ -1	1.64

Table 5.18: Results from box counting of the breakthrough pattern as well as its perimeter for CD50.

Structure	$c\sigma_{ls}$	$c\sigma_{le}$	r^2	r	Box dimension, D
Perimeter	0.02	0.02	0.999	≈ -1	1.61
Pattern	0.02	0.02	0.999	≈ -1	1.61

Table 5.19: Results from box counting of the breakthrough pattern as well as its perimeter for CD75.

Structure	$c\sigma_{ls}$	$c\sigma_{le}$	r^2	r	Box dimension, D
Perimeter	0.02	0.02	0.999	≈ -1	1.61
Pattern	0.02	0.02	0.999	≈ -1	1.61

Table 5.20: Results from box counting of the breakthrough pattern as well as its perimeter for CD100.

5.5.3 Flow patterns in open deformable porous media

The mass dimension of the growing flow patterns is calculated and listed in tables 5.21, 5.22, 5.23 and 5.24, and an example plot of the scale invariance check is shown in figure 5.13.

The fractal box dimensions for both the patterns and their perimeters are calculated for intermediate box sizes and the results are posted in tables 5.25, 5.26, 5.27 and 5.28.

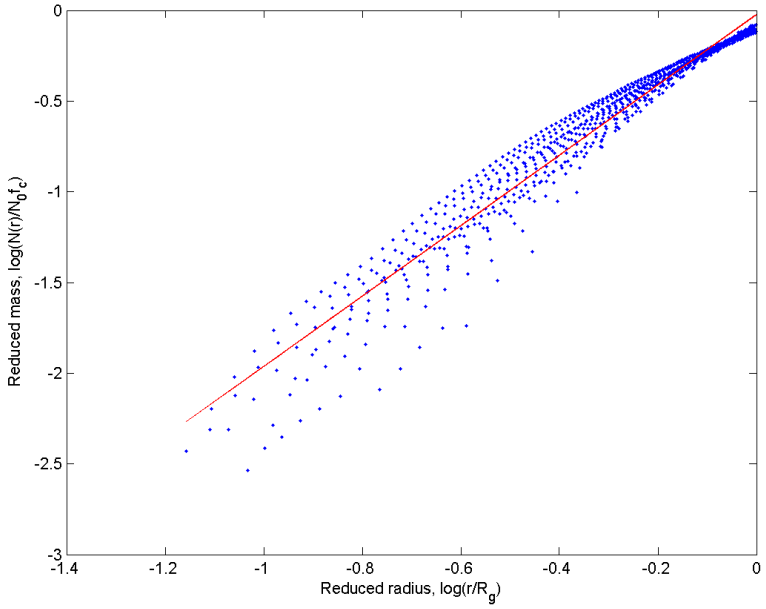

Figure 5.13: Plot of $log(N(r)/N_0 f_c)$ vs. $log(r/R_g)$ for observations in OD75. The timestep is 0.05s, and the datapoints (blue) are collapsed data from 18 subsequent frames of the growing structure. The least squares line (red) is also plotted with the a calculated fractal mass dimension $D = 1.94$ for the cluster. The pattern in OD75 does not seem to have scale invariant behavior for different cluster sizes.

Timestep, dt [s]	$c\sigma_{ls}$	$c\sigma_{le}$	r^2	r	Mass dimension, D
1	0.13	0.05	0.978	0.989	1.62
0.5	0.13	0.04	0.977	0.988	1.63
0.1	0.13	0.02	0.976	0.988	1.63

Table 5.21: Results of the mass dimension regression analysis for the observations in OD25 for different time resolutions, where smaller timestep between frames leads to more datapoints.

Timestep, dt [s]	$c\sigma_{ls}$	$c\sigma_{le}$	r^2	r	Mass dimension, D
0.5	0.13	0.06	0.982	0.991	1.81
0.1	0.15	0.04	0.977	0.988	1.88
0.05	0.15	0.03	0.976	0.988	1.90

Table 5.22: Results of the mass dimension regression analysis for the observations in OD50, where smaller timestep between frames leads to more datapoints.

Timestep, dt [s]	$c\sigma_{ls}$	$c\sigma_{le}$	r^2	r	Mass dimension, D
0.5	0.22	0.13	0.948	0.974	1.79
0.1	0.21	0.08	0.953	0.976	1.91
0.05	0.21	0.05	0.953	0.976	1.94

Table 5.23: Results of the mass dimension regression analysis for the observations in OD75, where smaller timestep between frames leads to more datapoints.

Timestep, dt [s]	$c\sigma_{ls}$	$c\sigma_{le}$	r^2	r	Mass dimension, D
0.5	0.15	0.07	0.977	0.989	1.77
0.1	0.17	0.04	0.971	0.986	1.79
0.05	0.17	0.03	0.967	0.983	1.79

Table 5.24: Results of the mass dimension regression analysis for the observations in OD100, where smaller timestep between frames leads to more datapoints.

Structure	$c\sigma_{ls}$	$c\sigma_{le}$	r^2	r	Box dimension, D
Perimeter	0.02	0.02	0.999	≈ -1	1.56
Pattern	0.03	0.02	0.998	-0.999	1.57

Table 5.25: Results from box counting of the breakthrough pattern as well as its perimeter for OD25.

Structure	$c\sigma_{ls}$	$c\sigma_{le}$	r^2	r	Box dimension, D
Perimeter	0.02	0.02	0.999	≈ -1	1.57
Pattern	0.03	0.02	0.999	-0.999	1.57

Table 5.26: Results from box counting of the breakthrough pattern as well as its perimeter for OD50.

5.6 Initial evaluation of the new growth measure

The growth of the flow patterns was decided to be investigated with four different time intervals $dt_1 = t_0/10$, $dt_2 = t_0/20$, $dt_3 = t_0/50$ and $dt_4 = t_0/100$. These time intervals are chosen

Structure	$c\sigma_{ls}$	$c\sigma_{le}$	r^2	r	Box dimension, D
Perimeter	0.03	0.02	0.999	-0.999	1.56
Pattern	0.04	0.03	0.998	-0.999	1.54

Table 5.27: Results from box counting of the breakthrough pattern as well as its perimeter for OD75.

Structure	$c\sigma_{ls}$	$c\sigma_{le}$	r^2	r	Box dimension, D
Perimeter	0.02	0.02	0.999	≈ -1	1.61
Pattern	0.03	0.02	0.999	-0.999	1.61

Table 5.28: Results from box counting of the breakthrough pattern as well as its perimeter for OD100.

considering the limitations of experimental duration and spatial resolution: on relative intervals $> dt_1$ the number of data points is low (> 10 per experiment) and on intervals $< dt_4$ the largest growth islands started to approach one pixel size, reducing the amount of observable growth.

As described in section 4.3.2 the relation between the number of growth sites N_I and the radius of gyration R_g were evaluated for all experiments and the relative timesteps chosen to investigate.

For equal relative timesteps, it was found that observations in the same porous media category had similar scaling behavior.

It was often found that for the timesteps dt_1 and dt_2 there was a "knee" separating two different slopes at $log(r/R_{g,max}) \approx -0.5$ corresponding to $R_{g,max}/3$, and for the timesteps dt_3 and dt_4 the "knee" was observed at $log(r/R_{g,max}) \approx -0.7$ corresponding to $R_{g,max}/5$. Figures 5.14 and 5.15 shows the observed characteristics which are similar for all the new growth measures.

Another unexplained behavior was noted for the observations in OD50: there was a substantial jump in N_i at $R_{g,max}/2$, see figure 5.16.

These initial evaluations of the results will be considered in the discussion of the new-growth measure in section 6.3.

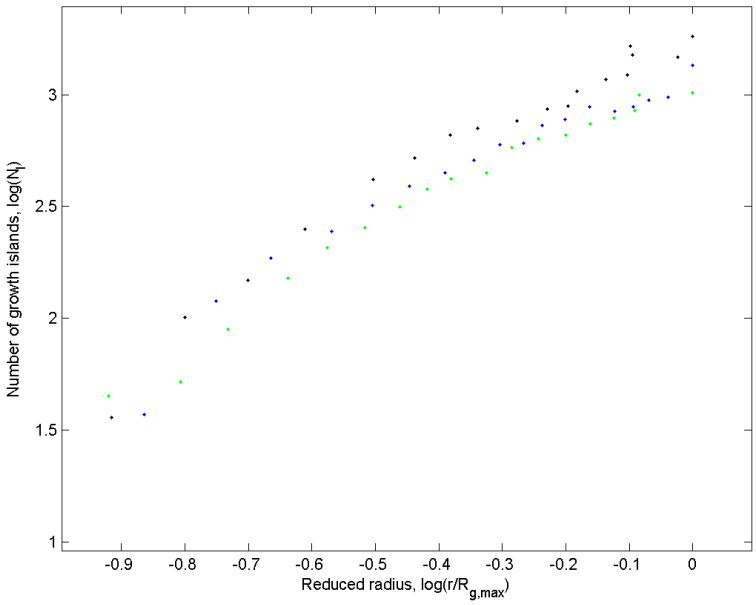

Figure 5.14: Here, $log(N_I)$ is plotted vs. $log(r/R_{g,max})$ for observations in open deformable porous media. The relative timestep is $dt_2 = t_0/20$. Note the "knee" at $log(r/R_{g,max}) \approx -0.5$

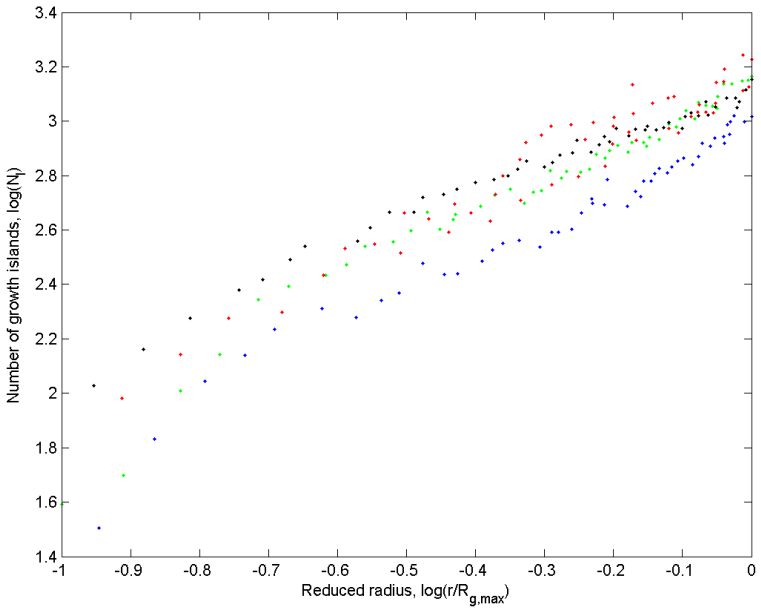

Figure 5.15: Here, $log(N_I)$ is plotted vs. $log(r/R_{g,max})$ for observations in constricted deformable porous media. The relative timestep is $dt_3 = t_0/50$. Note the "knee" at $log(r/R_{g,max}) \approx -0.7$

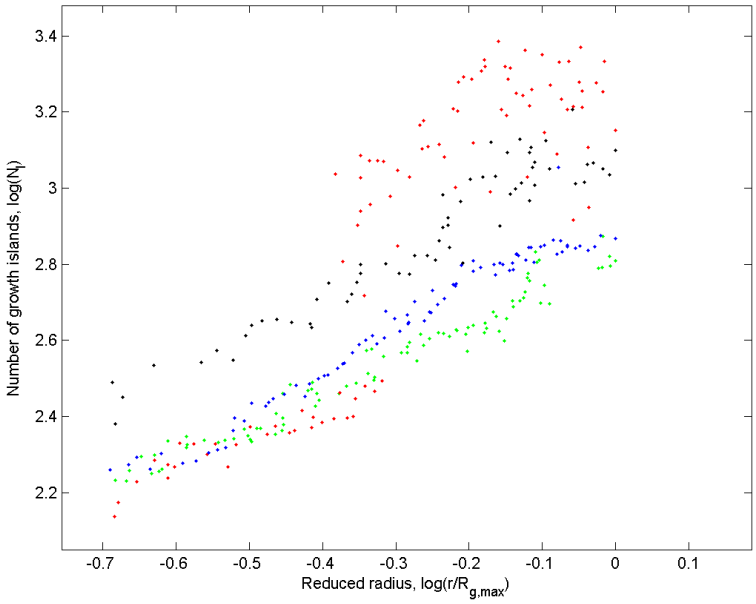

Figure 5.16: Plot of $log(N_I)$ vs. $log(r/R_{g,max})$ for open deformable porous media with a time interval $dt_4 = t_0/100$. Note the sudden jump in $log(N_I)$ at $log(r/R_{g,max}) \approx -0.3$ for OD50 (red)

Chapter 6

Discussion of results

6.1 Porous media samples, fluids and flow regimes

The estimated porosities of the samples are not to be taken too literarily, but they serve as qualitative indications that the samples within the same category have similar porosities. In fact, they indicate that all the samples used have similar porosities. The real porosity could be measured for the non-deformable samples as the ratio of the defending fluid volume necessary to saturate the pore space to the total sample volume, but this was unfortunately not performed. This direct measurement method is more complicated for the deformable samples due to the saturation method.

The nearest neighbor distance histograms are also only meant as an indicator of the organization of particles within the samples. The degree of randomness is indicated by the range of distances with high count values and is a good supplement to visual characteristics of the sample.

Characterizations of the fluids shows that all the two phase flow experiments are drainage processes where inviscid, non-wetting air invades a porous media saturated with a wetting, viscous glycerol/water mixture. We have the parameters necessary for finding the capillary and Reynolds numbers for the experiments by using equations (2.9), and (2.23) combined with (2.5). Results for all experiments and values used are posted in table 6.1. All capillary numbers are high, $Ca > 10^{-3}$, indicating that the flow is in the viscous fingering regime, while all Reynolds numbers are low, $Re < 1$, indicating that the flow is laminar.

6.2 Characterization of flow patterns using fractal dimension

Box dimensions obtained for the flow patterns

The box dimensions obtained for the flow patterns vary between $D = 1.53$ and $D = 1.64$, and it does not appear any significant different behavior of the box counting dimensions for the different flow patterns that can be used to distinguish them from eachother or characterize them. The values are around the determined fractal dimension of viscous fingering but they do not reveal

Experiment	ND1	ND2	CD25	CD50	CD75
Defending Fluid	L1	L1	L3	L4	L4
Darcy velocity, v [mm/s]	1.6	1.9	1.4	5.5	11.4
Typical length scale, l [mm]	1.26	1.27	1.13	1.26	1.26
Kinematic viscosity, ν [mm^2/s]	37.74	37.74	41.37	40.90	40.90
Density, ρ [mg/mm^3]	1.124	1.124	1.126	1.126	1.126
Surface tension, γ [μN/mm]	65.7	65.7	65.7	65.7	65.7
Capillary number, Ca	$1.0 \cdot 10^{-3}$	$1.2 \cdot 10^{-3}$	$1.0 \cdot 10^{-3}$	$3.9 \cdot 10^{-3}$	$7.99 \cdot 10^{-3}$
Reynolds number, Re	$5.3 \cdot 10^{-2}$	$6.4 \cdot 10^{-2}$	$3.8 \cdot 10^{-2}$	$1.7 \cdot 10^{-1}$	$3.5 \cdot 10^{-1}$
Experiment	CD100	OD25	OD50	OD75	OD100
Defending Fluid	L4	L3	L3	L2	L3
Darcy velocity, v [mm/s]	20.7	3.4	12.6	16.0	25.0
Typical length scale, l [mm]	1.26	1.4	1.4	1.4	1.4
Kinematic viscosity, ν [mm^2/s]	40.90	41.37	41.37	40.08	41.37
Density, ρ [mg/mm^3]	1.126	1.126	1.126	1.125	1.126
Surface tension, γ [μN/mm]	65.7	65.7	65.7	65.7	65.7
Capillary number, Ca	$1.45 \cdot 10^{-2}$	$2.4 \cdot 10^{-3}$	$8.93 \cdot 10^{-3}$	$1.10 \cdot 10^{-2}$	$1.77 \cdot 10^{-2}$
Reynolds number, Re	$6.4 \cdot 10^{-1}$	$1.2 \cdot 10^{-1}$	$4.3 \cdot 10^{-1}$	$5.6 \cdot 10^{-1}$	$8.8 \cdot 10^{-1}$

Table 6.1: The capillary and Reynolds numbers are estimated for the different experiments using these parameters. Note that the plate separation has been used as the characteristic length scale for the open deformable porous media.

any significant information about the differences in the flow patterns between non-deformable and deformable experiments. In addition, it has been found that the mass dimension is a more robust description of the clusters in two phase flow experiments [4].

Fractal dimension of flow patterns in non-deformable porous media

The results for the mass dimension were found to be $D = 1.57 \pm 0.01$ for the pattern in ND1, fig. 2.9, and $D = 1.66$ for the pattern in ND2, fig. 6.1. In both experiments, the linear correlation of the data points to the scaling relation [eq.] is very strong for growing clusters of various sizes R_g and over all ranges $r_0 < r < R_g$ as shown in fig. 5.11.

If the data points for $log(N(r)/N_0 f_c)$ vs. $log(r/R_g)$ for both ND1 and ND2 are combined as in figure 6.2, the calculated mass dimension is $D = 1.62$. Evaluation of the regression line is posted in table 6.2.

$c\sigma_{ls}$	$c\sigma_{le}$	r^2	r	Mass dimension, D
0.06	< 0.01	0.995	0.998	1.62

Table 6.2: Evaluation parameters for the regression line in fig. 6.2.

The fractal dimension for viscous fingering patterns in porous media has been established in earlier research [4] as $D = 1.62$.

The fact that the fractal dimensions obtained for the separate experiments ND1 and ND2 are close to the earlier established value and that the observations from both experiments results in

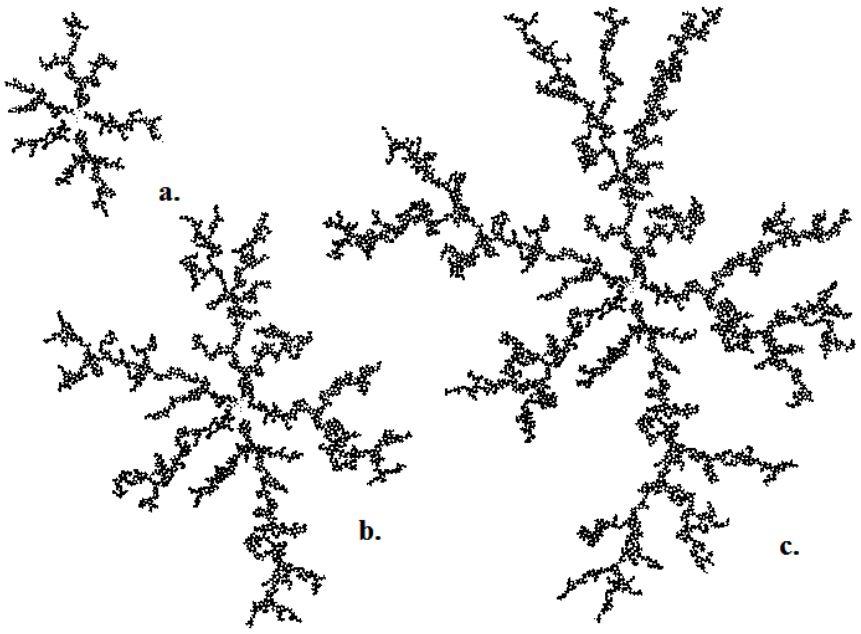

Figure 6.1: Some of the clusters involved in the calculation of the fractal dimension for ND2. The growing clusters (a-c) are separated by 2s intervals. The scaling is easy to spot: They all look the same, but with different sizes.

a fractal dimension equal to the established value is reassuring. It indicates that the calculations are performed correctly, as well as the results based on 10725 observations strengthen the earlier established value.

Fractal dimension of flow patterns in constricted deformable porous media

The number-radius plots for the observations in CD25, CD50, CD75 and CD100 has no definite scale invariant linear relationship, as shown in fig. 5.12. Based on that observation together with the calculation of $D = 2.06 \pm 0.02$ for CD50 we are motivated to take a closer look on the number-radius relation for the flow patterns in the constricted deformable porous media experiments. Even though the regression lines had strong correlation with the data points, the standard deviations of 95% confidence, $c\sigma_{ls}$ were about 2-6 times larger than for the non-deformable regression lines, indicating more spread of observations about the fitted lines.

To get a clearer view of the situation, the number-radius relations for the breakthrough clusters of CD25, CD50, CD75 and CD100 were combined into one plot of $log(N(r)/N_0 f_c)$ vs. $log(r/R_g)$. Figure 6.3 shows the observations.

The knee observed in the plot separates two regions in the number-radius relation for the experiments, where the regions have different slopes. Results of regression analyses on region 1 ($log(r/R_g) \in [-1, -0.5]$) and region 2 ($log(r/R_g) \in [-0.5, 1]$) are listed in table 6.3 and shown in figures 6.4 and 6.5.

It is found that the part of the clusters inside a radius $r/R_g \approx 1/3$ is not fractal since $D =$

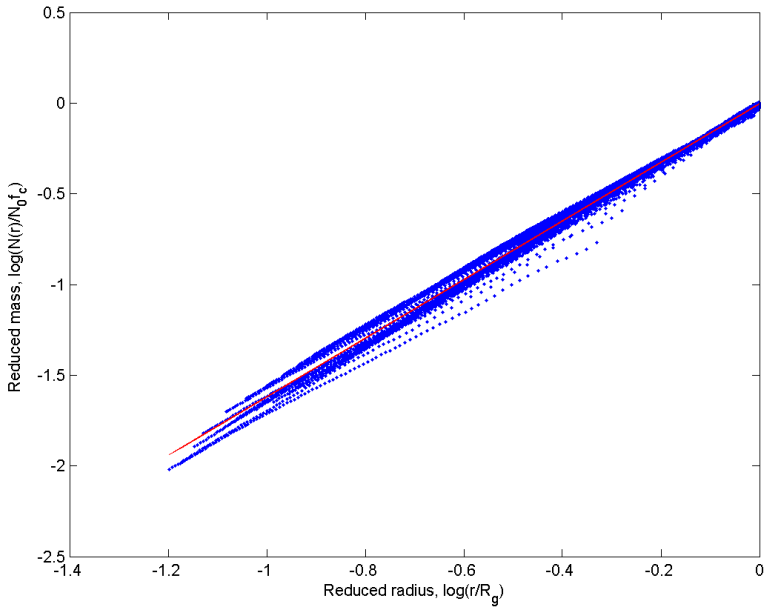

Figure 6.2: The combined set of datapoints (blue) from ND1 and ND2 evaluated at a time increment of 0.1s is used in estimation of the mass dimension for the flow pattern in non-deformable porous media. The least-squares line (red) is found from the 10725 observations, and has the slope $D = 1.62$.

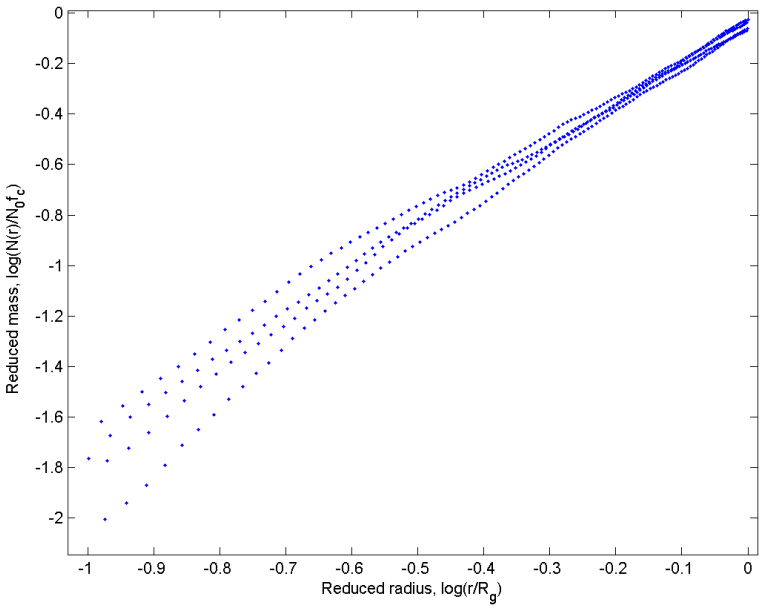

Figure 6.3: The combined number-radius relations for CD25, CD50, CD75 and CD100. Note that there is a "knee" in the slopes at $log(r/R_g) \approx -0.5$ corresponding to $r/R_g \approx 1/3$.

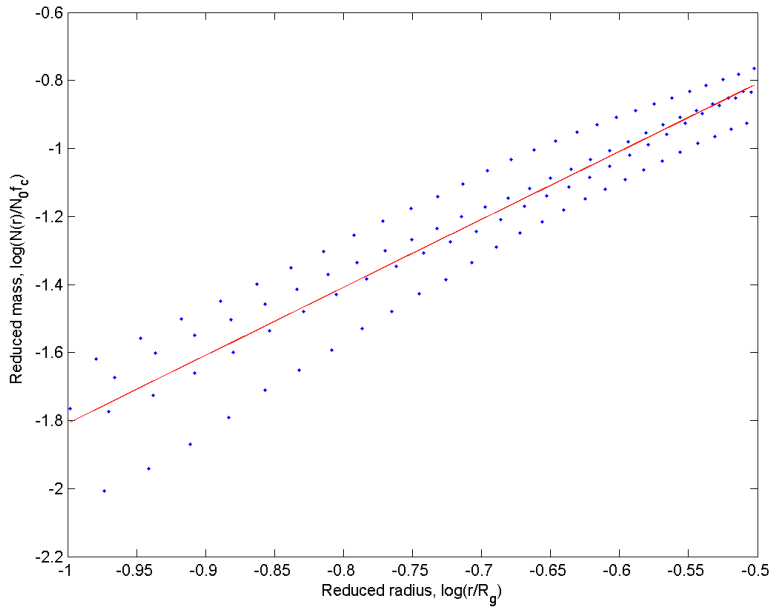

Figure 6.4: Plot of data points (blue) in region 1, below the "knee" at $log(r/R_g) \approx -0.5$ corresponding to $r/R_g \approx 1/3$. The linear regression line is shown in red.

Region	$c\sigma_{ls}$	$c\sigma_{le}$	r^2	r	Mass dimension, D
1	0.19	0.26	0.894	0.946	2.00 ±0.26
2	0.05	0.04	0.985	0.992	1.58 ±0.04

Table 6.3: Results of regression analysis on the regions in the number-radius relation for the observations of flow patterns in constricted deformable porous media.

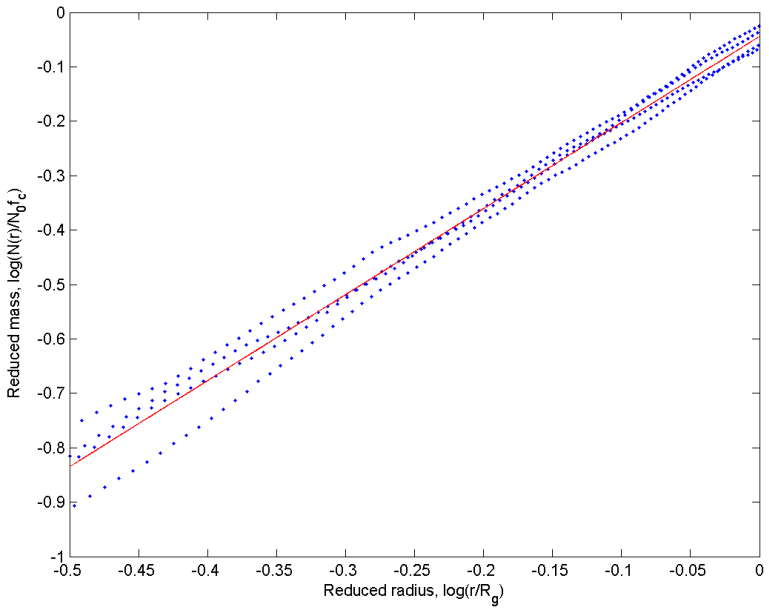

Figure 6.5: Plot of data points (blue) in region 2, above the "knee" at $log(r/R_g) \approx -0.5$ corresponding to $r/R_g \approx 1/3$. The linear regression line is shown in red.

2.00 ± 0.26 for region 1. Outside this radius, in region 2, the fractal dimension is $D = 1.58 \pm 0.04$. Figure 6.6 shows the breakthrough cluster for CD25 with the regions 1 and 2 indicated.

Fractal dimension of flow patterns in open deformable porous media

As seen in figure 5.13, the number-radius relation does not scale equally for all growing clusters of size $Rg(t)$, or over all radii $r_{min} < r < R_g(t)$. Therefore, as in the previous section, the observations of $log(N(r)/N_0 f_c)$ vs. $log(r/R_g)$ for the breakthrough patterns in OD25, OD50, OD75 and OD100 were plotted into one graph as shown in figure 6.7.

The knee observed in the plot separates two regions in the number-radius relation for the experiments, where the regions have different slopes. Results of regression analyses on region 1 ($log(r/R_g) \in [-1, -0.5]$) and region 2 ($log(r/R_g) \in [-0.5, 1]$) are listed in table 6.4 and shown in figures 6.8 and 6.9.

The mass dimension calculated for region 1, $D = 1.89 \pm 0.17$, indicates thick invasion fingers which exceeds the scaling relation of viscous fingering. Since the uncertainty includes $D = 2.00$

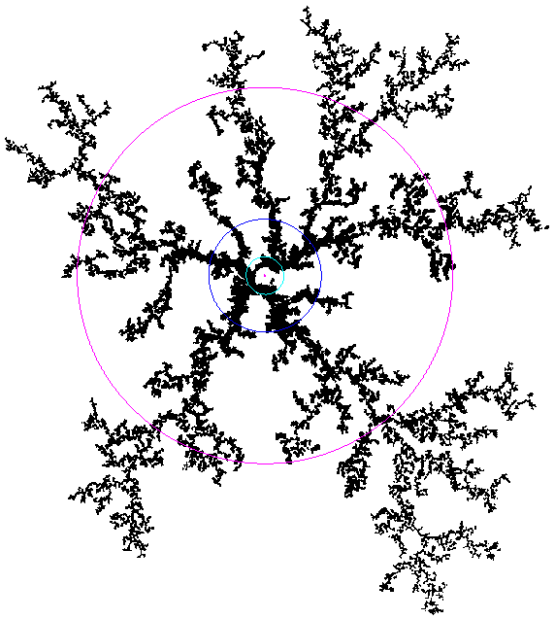

Figure 6.6: The breakthrough cluster in CD25. Between the cyan and blue rings is region 1, and between the blue and magenta rings is region 2. The mass dimensions can be "seen" as the pattern in region 1 is thick, while the pattern outside region 1 looks like viscous fingering in a non-deformable porous media.

Region	$c\sigma_{ls}$	$c\sigma_{le}$	r^2	r	Mass dimension, D
1	0.13	0.17	0.946	0.973	1.89±0.17
2	0.04	0.03	0.992	0.996	1.48±0.03

Table 6.4: Results of regression analysis on the regions in the number-radius relation for the observations of flow patterns in open deformable porous media.

for the pattern in region 1, it is assumed to not be fractal in this region. The mass dimension calculated for region 2, $D = 1.48 \pm 0.03$, indicates a fractal flow pattern with mass distribution close to, but less than that of viscous fingering. The fractal dimension in region two is assumed to be explained by capillary fracturing, which creates thicker than pore size conduits for flow. The conduits are able to carry a larger part of the flow, and grows on the expense of viscous fingers. Thicker and straighter fingers instead of thin and wiggly fingers will lower the mass dimension of the pattern. This assumption seems to be consistent with the pattern in figure 6.10, as well as with earlier work with deformable porous media [14] where fractal dimensions of $D_f = 1.51$ and $D_f = 1.52$ were found in the transition between viscous fingering and capillary fracturing.

To investigate the tendency of capillary fracturing outside the R_g of the breakthrough patterns, the number-radius relation in an outer region $r \in log(r/Rg) = [0, 0.1]$ was investigated, see fig. 6.11. This region corresponds to $r/R_g \in [1, 5/4]$ of the breakthrough patterns as shown in fig. 6.12. The results of the regression analysis on the number-radius relation in this region gives the mass dimension $D = 1.11 \pm 0.09$, listed in table 6.5. To get a perspective on this data, the outer region was evaluated for a combination of ND and CD observations, which are found to be

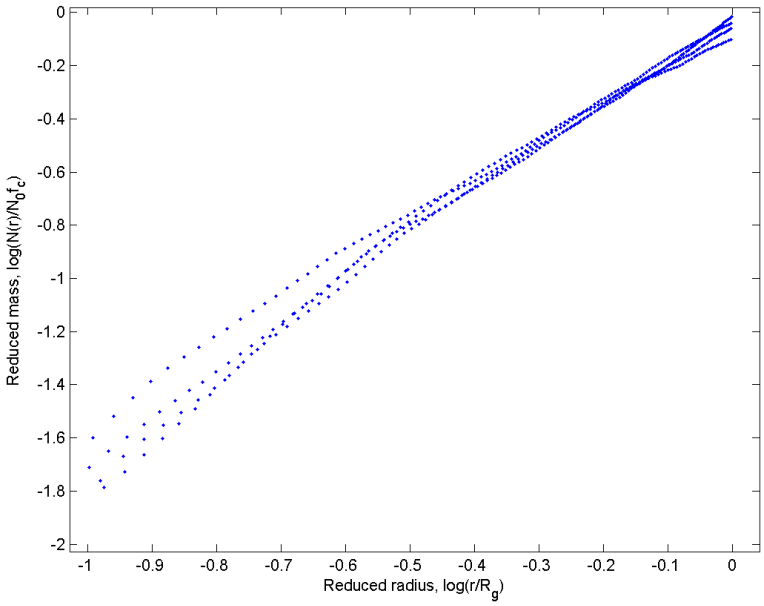

Figure 6.7: The combined number-radius relations for the breakthrough patterns in OD25, OD50, OD75 and OD100. Here, there is also a "knee" in the slopes at $log(r/R_g) \approx -0.5$ corresponding to $r/R_g \approx 1/3$.

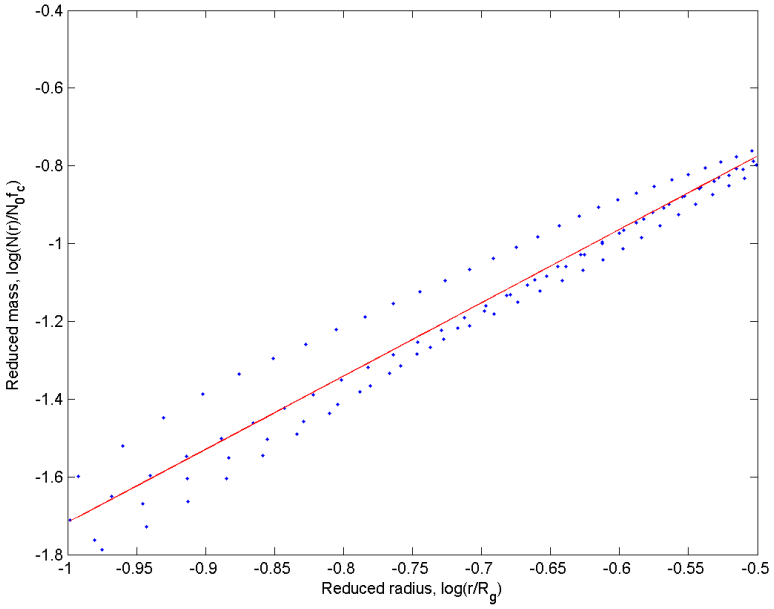

Figure 6.8: Plot of data points (blue) in region 1, below the "knee" at $log(r/R_g) \approx -0.5$ corresponding to $r/R_g \approx 1/3$. The linear regression line is shown in red.

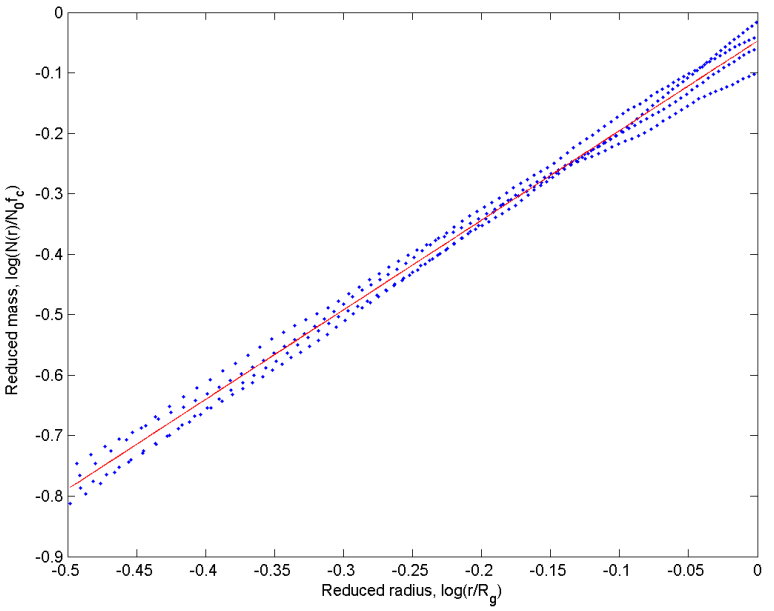

Figure 6.9: Plot of data points (blue) in region 2, above the "knee" at $log(r/R_g) \approx -0.5$ corresponding to $r/R_g \approx 1/3$. The linear regression line is shown in red.

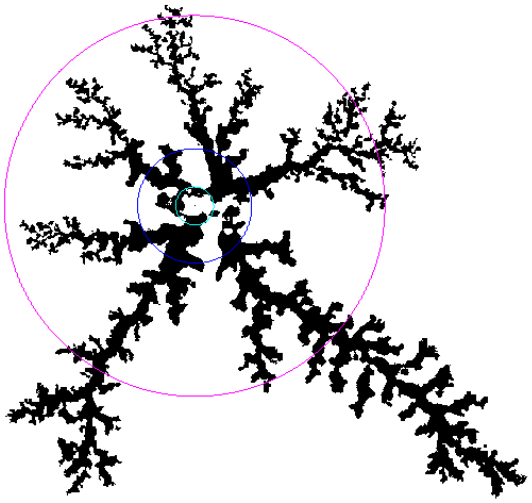

Figure 6.10: The breakthrough cluster in OD75. Between the cyan and blue rings is region 1, and between the blue and magenta rings is region 2. In region 1, the fingers are thick as expected due to the mass dimension $D = 1.89 \pm 0.17$. In region 2, the pattern looks like a mixture of viscous fingering in a non-deformable porous media (top-half) and capillary fracturing (bottom half). This is consistent with the lower fractal dimension $D = 1.48 \pm 0.03 < 1.62$. Also note that outside region 2, the growth of fracture conduits dominate over viscous fingering.

similar in this region as shown in fig. 6.13. The result is $D = 1.33 \pm 0.01$.

This indicates a more concentrated flow pattern in the outer region for the flow in open deformable porous media than for non-deformable and constricted deformable, and that capillary fracturing occurs when the viscous fingers approach the open surface of the porous media. The reason of selecting such a narrow outer region, is due to the finite size of the patterns which leads to flattening of the number-radius relation as $log(N(r)/N_0 f_c) \to -log(f_c)$ for $log(r/R_g) \gg 0$. This flattening is probably also the cause of the low fractal dimensions $D \to 1$ in the outer region.

Region	$c\sigma_{ls}$	$c\sigma_{le}$	r^2	r	Mass dimension, D
Outer, OD	0.02	0.09	0.940	0.970	1.11±0.09
Outer, ND+CD	0.01	0.04	0.990	0.995	1.33±0.04

Table 6.5: Results of regression analysis on the number-radius relation in the outer regions of breakthrough flow patterns.

6.3 Investigation of the multifractal new-growth measure

Explanation for the sudden jump in $log(N_I)$ vs. $log(R_g)$ for OD50

The behavior of the $log(N_I)$ vs. $log(R_g)$ shown in fig. 5.16 for OD50, where there is a sudden jump in the N_I values at $r \approx R_{g,max}/2$, was investigated by looking at the sequence of frames

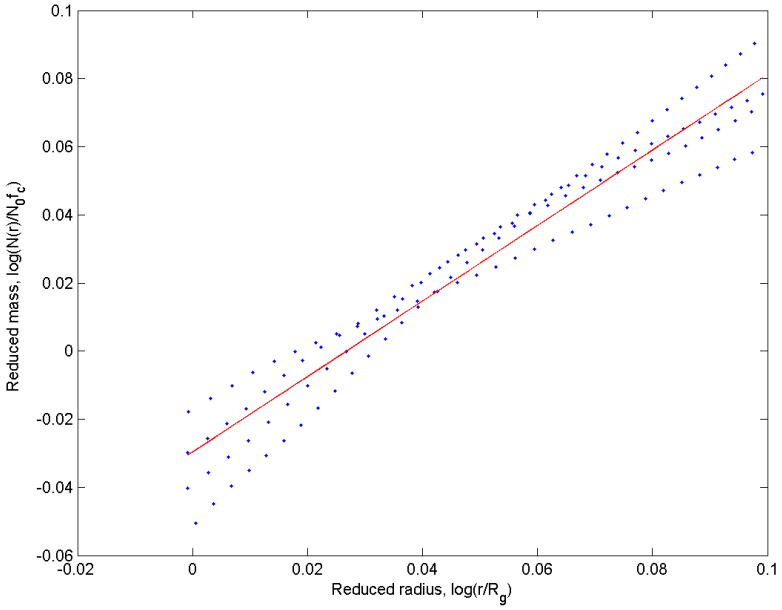

Figure 6.11: The number-radius relation for the outer region of the breakthrough patterns in OD25, OD50, OD75 and OD100.

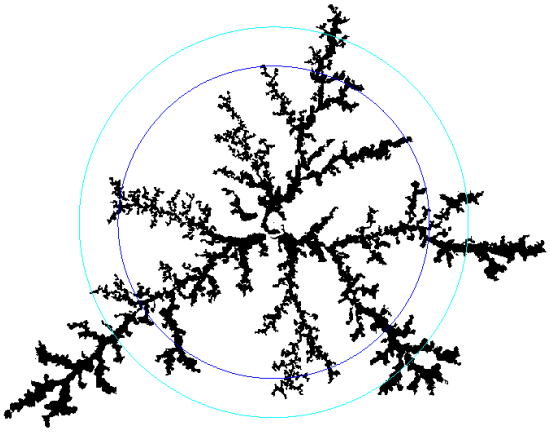

Figure 6.12: The breakthrough cluster in OD50. The outer region is between the rings of radius $r/R_g = 1$ (blue) and $r/R_g = 5/4$ (cyan), where capillary fracturing is starting to dominate the flow.

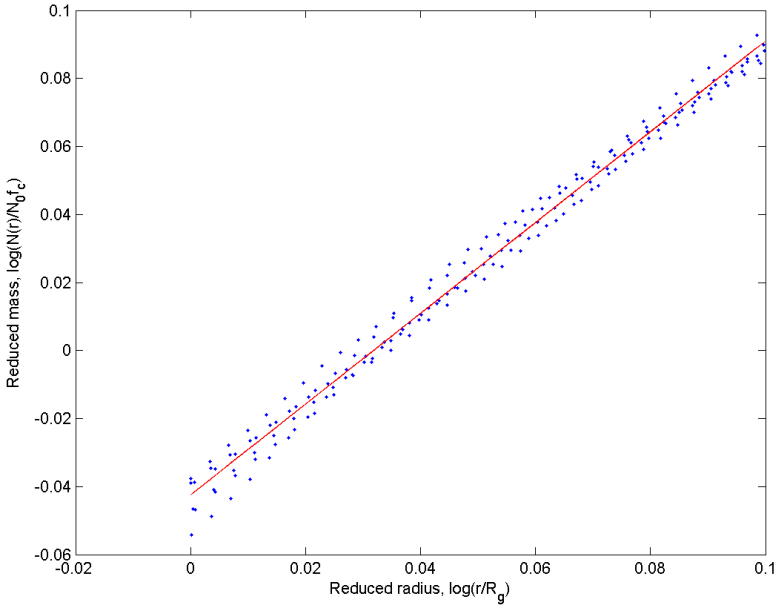

Figure 6.13: The number-radius relation for the outer region of the breakthrough patterns in all ND and CD experiments.

with relative timestep dt_3. It was found that the actual flow pattern started to oscillate as in a shaking motion at the relevant frames, probably because the tripod of the high speed camera was unfortunately bumped into.

It is easy to imagine that the sequence of subtracted frames of a shaking pattern will obtain a lot of extra "growth islands". Therefore, it is decided to exclude the data from OD50 in the multifractal growth analysis.

The multifractal growth in different porous media types on different time intervals.

Based on the findings in the initial evaluation of the new-growth measure, we will combine observations from experiments with the same relative timestep and from the same sample category into sets of similar observations. The new-growth measure will be investigated on intervals of $R_{g,max}/3 < R_{g,max}$ for dt_1 and dt_2, and on the intervals $R_{g,max}/5 < R_{g,max}$ for dt_3 and dt_4. Characteristic differences or similarities in the multifractal growth behavior between experiments and time intervals are looked for.

The results of the calculations of interface dimensions are posted in 6.6.

The sequences of mass exponents $\tau(q)$ are found for each timestep and sample category. The obtained $\tau(q)$ for different timesteps are plotted for each sample category. The plots are shown in figures 6.14, 6.15 and 6.16.

Then we derive α from the sequences of mass exponents, the resulting plots of $\alpha(q)$ vs. q are shown in 6.17, 6.18 and 6.19.

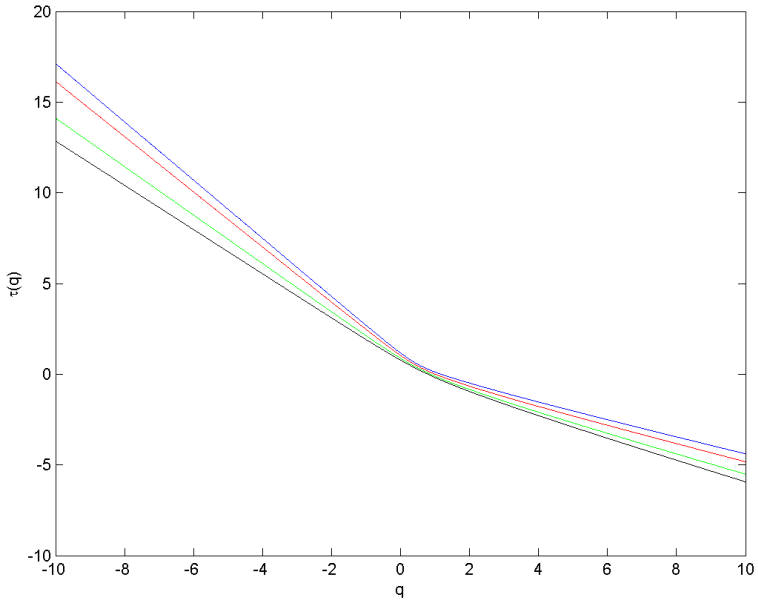

Figure 6.14: The obtained sequence of mass exponents for the new-growth measure of the non-deformable experiments observed at different relative time intervals, $dt_1 = t_0/10$ (blue), $dt_2 = t_0/20$ (red), $dt_3 = t_0/50$ (green) and $dt_4 = t_0/100$ (black).

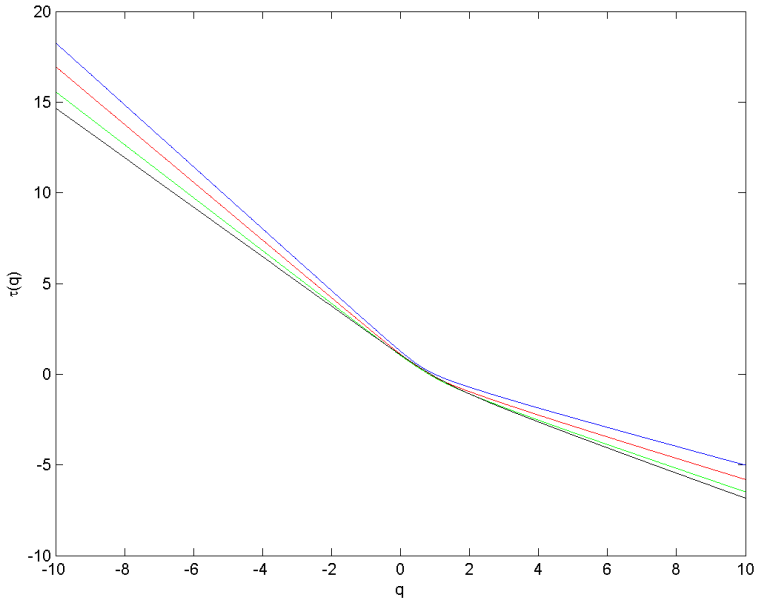

Figure 6.15: The obtained sequence of mass exponents for the new-growth measure of the constricted deformable experiments observed at different relative time intervals, $dt_1 = t_0/10$ (blue), $dt_2 = t_0/20$ (red), $dt_3 = t_0/50$ (green) and $dt_4 = t_0/100$ (black).

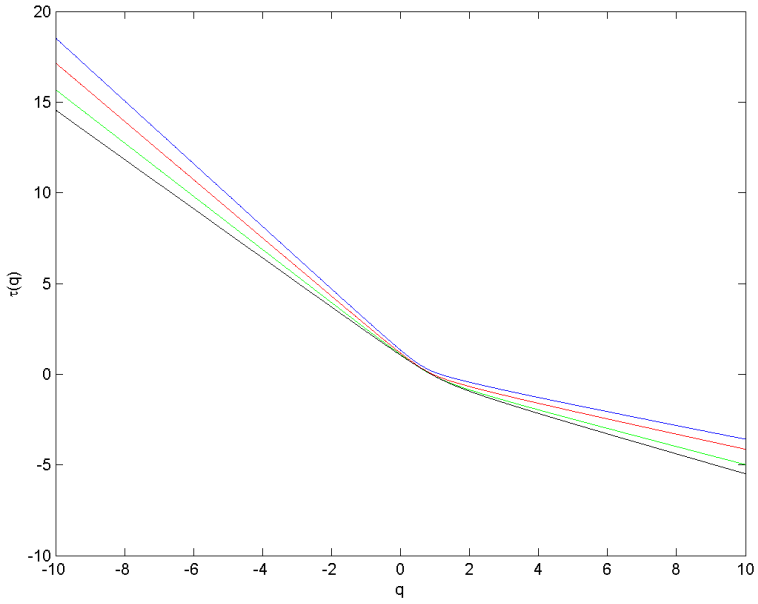

Figure 6.16: The obtained sequence of mass exponents for the new-growth measure of the open deformable experiments observed at different relative time intervals, $dt_1 = t_0/10$ (blue), $dt_2 = t_0/20$ (red), $dt_3 = t_0/50$ (green) and $dt_4 = t_0/100$ (black).

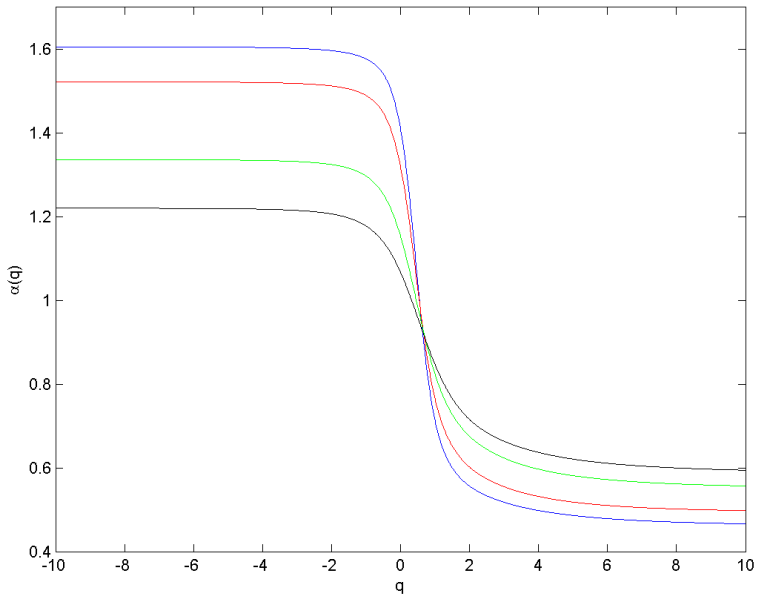

Figure 6.17: Plots of the derived $\alpha(q)$ vs. q for the new-growth measure of flow in a non-deformable porous media observed at the relative time intervals, $dt_1 = t_0/10$ (blue), $dt_2 = t_0/20$ (red), $dt_3 = t_0/50$ (green) and $dt_4 = t_0/100$ (black).

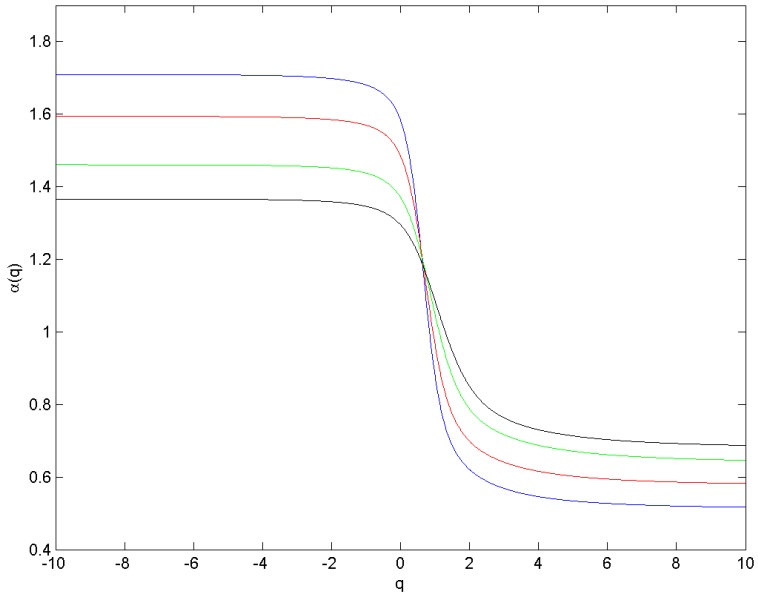

Figure 6.18: Plots of the derived $\alpha(q)$ vs. q for the new-growth measure of flow in a constricted deformable porous media observed at the relative time intervals, $dt_1 = t_0/10$ (blue), $dt_2 = t_0/20$ (red), $dt_3 = t_0/50$ (green) and $dt_4 = t_0/100$ (black).

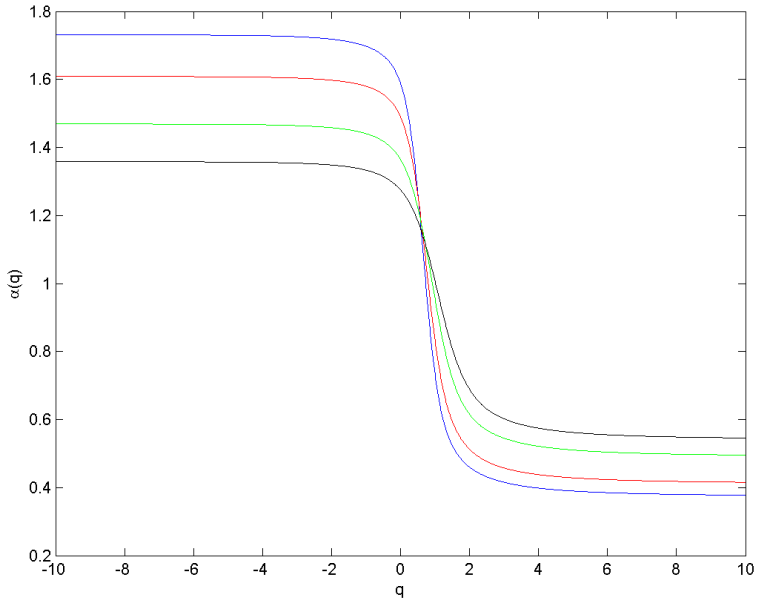

Figure 6.19: Plots of the derived $\alpha(q)$ vs. q for the new-growth measure of flow in an open deformable porous media observed at the relative time intervals, $dt_1 = t_0/10$ (blue), $dt_2 = t_0/20$ (red), $dt_3 = t_0/50$ (green) and $dt_4 = t_0/100$ (black).

Experiment	Relative timestep, dt [s]	$c\sigma_{ls}$	$c\sigma_{le}$	r^2	r	Interface dimension D_I
ND	$t_0/10$	0.06	0.25	0.965	0.982	1.18 ± 0.25
ND	$t_0/20$	0.10	0.30	0.903	0.950	1.04 ± 0.30
ND	$t_0/50$	0.11	0.12	0.907	0.953	0.89 ± 0.12
ND	$t_0/100$	0.13	0.10	0.842	0.918	0.78 ± 0.10
CD	$t_0/10$	0.23	0.57	0.716	0.846	1.28 ± 0.57
CD	$t_0/20$	0.20	0.37	0.689	0.830	1.10 ± 0.37
CD	$t_0/50$	0.21	0.16	0.767	0.876	1.05 ± 0.16
CD	$t_0/100$	0.21	0.13	0.761	0.872	1.08 ± 0.13
OD	$t_0/10$	0.13	0.38	0.910	0.954	1.34 ± 0.38
OD	$t_0/20$	0.16	0.37	0.800	0.895	1.17 ± 0.37
OD	$t_0/50$	0.19	0.17	0.828	0.910	1.09 ± 0.17
OD	$t_0/100$	0.22	0.15	0.759	0.871	1.06 ± 0.15

Table 6.6: Calculation results for the interface dimension for non-deformable (ND), constricted deformable (CD) and open deformable (OD) porous media at different time intervals.

And finally, the $f(\alpha)$ curves can be obtained. They are shown in figures 6.20, 6.21 and 6.22.

6.4 Observations of particle displacement in deformable porous media.

Forces involved

Based on observations of particle displacement in the deformable porous media experiments, three main types of forces are assumed to be involved in the particle displacement. These forces act on different scales and regions in the system.

On the sample size scale, particles are generally displaced in the bulk of the defending fluid if $F_D > F_F$, where F_D is the drag force of the viscous fluid in its flow direction with respect to the particle. F_F is the force of a particles resistance to move. F_F is assumed to be a combination of interparticle interaction and the frictional force between the particle and plates. The drag force of a flowing viscous fluid on a stationary sphere of radius a is given by Stokes law as

$$f_D = 6\pi\mu a v, \tag{6.1}$$

where μ is the viscosity of the fluid and v the Darcy velocity of the fluid. Then, if a group of n particles interact, it is assumed that

$$F_D \sim n f_D. \tag{6.2}$$

Similarily, if the typical friction force of a particle is f_0, it is assumed that

$$F_F \sim n f_0 + F_b, \tag{6.3}$$

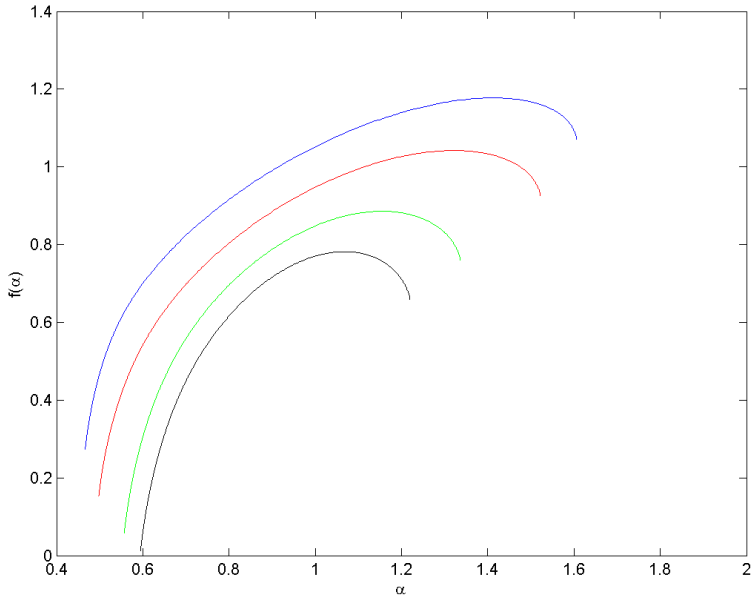

Figure 6.20: The obtained $f(\alpha)$ curves plotted against α for the new-growth measure of flow in a non-deformable porous media observed at the relative time intervals, $dt_1 = t_0/10$ (blue), $dt_2 = t_0/20$ (red), $dt_3 = t_0/50$ (green) and $dt_4 = t_0/100$ (black).

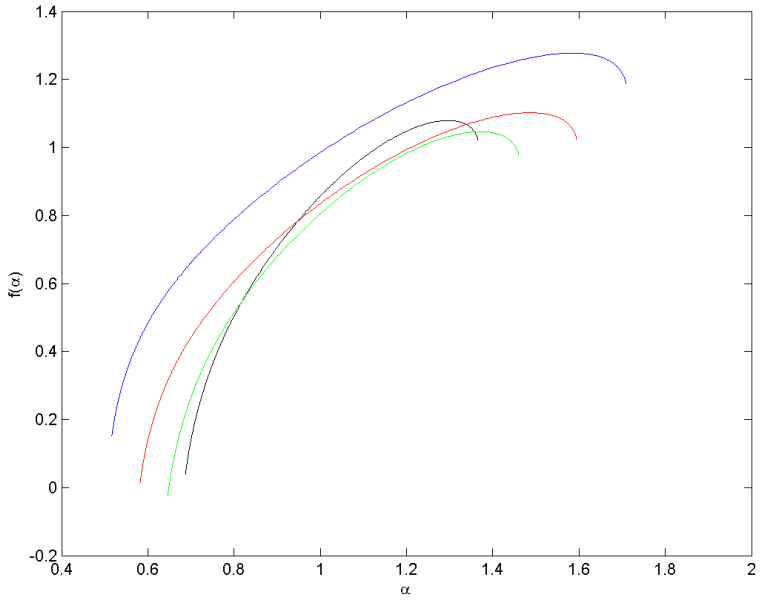

Figure 6.21: The obtained $f(\alpha)$ curves plotted against α for the new-growth measure of flow in a non-deformable porous media observed at the relative time intervals, $dt_1 = t_0/10$ (blue), $dt_2 = t_0/20$ (red), $dt_3 = t_0/50$ (green) and $dt_4 = t_0/100$ (black).

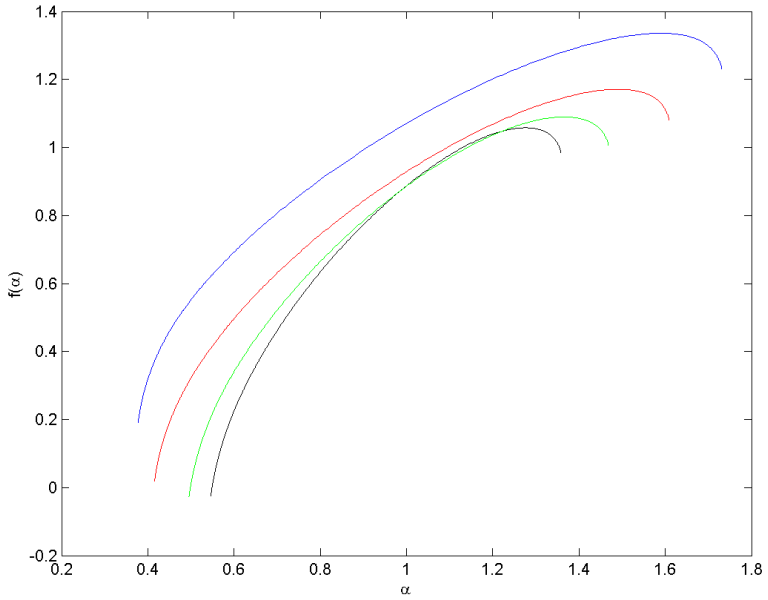

Figure 6.22: The obtained $f(\alpha)$ curves plotted against α for the new-growth measure of flow in a non-deformable porous media observed at the relative time intervals, $dt_1 = t_0/10$ (blue), $dt_2 = t_0/20$ (red), $dt_3 = t_0/50$ (green) and $dt_4 = t_0/100$ (black).

where n is the number of particles interacting, and F_b is some external force on the group of n particles.

On the pore size scale, particle displacement is assumed to occur at the interface between the invading and defending fluids when $f_C > f_F$, where f_C is the local capillary force in a pore neck and f_F is the frictional resistance force of a particle of the pore neck. The f_F of a particle may be a combination of its own friction with the sample plate and interaction with other particles. The capillary force is assumed to act on the particles parallell to their separation l as

$$f_C \sim \pm\gamma/l, \tag{6.4}$$

where it is positive in the case of drainage and negative for imbibition.

This is a hypothesis of involved forces and has not been thoroughly worked with. However, it is some thoughts of what was observed.

6.5 Conclusive summary

Ten experiments of two phase flow in porous Hele-Shaw cells have been performed, where the invading fluid was air and the defending fluid was a viscous glycerol/water solution. The goal of the experiments was to investigate the differences and similarities between flow patterns when given different border conditions in the porous sample. The adjustable control parameters in the experiments were the invasion pressure, which was set to be constant at a given value during two phase flow, and the deformability of the porous sample. The porous sample could be made in three different varieties, i.e. a non-deformable porous media, a constricted but deformable porous media, and an open deformable porous media. Of the ten experiments 2 were non-deformable with a 25mbar injection pressure, 4 were constricted deformable with injection pressures of 25mbar, 50mbar, 75mbar or 100mbar, and 4 were open deformable with the different injection pressures of 25mbar, 50mbar, 75mbar and 100mbar.

The actual invasions were captured on digital images with a high speed camera, capturing frames with a framerate of 125fps or 250fps, giving a fair amount of data to analyze. The analysis was focused on fractal dimensions of the clusters, multifractal growth statistics, displacement of the porous media and visual characterization of the flow patterns.

All the experiments were characterized to lie within the viscous fingering regime in terms of capillary number, which was $Ca \geq 10^{-3}$ for all experiments. With the fact that the displacement regime was drainage of a viscous fluid by an inviscid fluid, an unstable flow patterns was guaranteed.

When it comes to the mass dimension of the flow patterns, we see that the flow patterns in the non-deformable porous media is in excellent agreement with previous studies, where $D = 1.62$. On the other hand, the flow patterns in both types of deformable porous media deviated from this behavior. Flow patterns in both variants of deformable porous media were found to have inital clusters that was not fractal. After they expanded to roughly 1/3 of their breaktrough sizes, they started to obtain a fractal mass dimension, where the flow pattern in the constricted deformable samples tended towards the behavior of the non-deformable flow pattern, and the flow pattern in the open deformable samples had a fractal dimension of about 1.50 until it quickly went over to pure capillary fracturing behavior, and presumably $D \to 1$.

The multifractal growth analysis shows that the effects of decreasing timestep generally decreases the interface dimensions D_I. Which can possibly be explained by the limiting resolution of our experiments and partially the time required for an invasion to occur. We also note that the multifractal growth measure scales equally for the same sample category patterns with the same relative timestep. This may be an indication that the growth of the same cluster types has the same behavior independent of breakthrough time and pressure.

If we decide to compare the new-growth measure of the different flow pattern categories at the timestep $t_0/100$ for example, we see that the deformable patterns have similar values $D_I = 1.06 \pm 0.15$ and $D_I = 1.08 \pm 0.13$. The non-deformable pattern has only $D_I = 0.78 \pm 0.10$. When taking a look at the $f(\alpha)$ curves, it is observed that the patterns in the non-deformable sample has the narrowest and lowest curves, the constricted deformable has the intermediate values, while the open deformable have the widest and tallest $f(\alpha)$ curves. Since the range of α corresponds to a range in μ and $f(\alpha)$ corresponds to a quantity of points, we may interpret this as: the flow pattern in open deformable samples grows fastest and has a more even distribution of growth islands all over its interface, the constricted deformable is somewhere near that behavior and, in the case of the non-deformable there is a smaller range of growth islands mainly distributed on the fingertips. This was confirmed by looking at growth images, where the deformable patterns had observed growth evenly distributed over their interface, while the non-deformable pattern had fewer growth sites, mainly on the fingertips.

Some of the PIV results, figures 6.23 and 6.24, also prove to characterize a difference between flow patterns in non-deformable, constricted deformable and open deformable porous media. The non-deformable porous samples have not been processed with the PIV program, but it is reasonable to assume that the area mean value of particle displacement is zero, which is characteristic for those samples. The constricted deformable samples have "explosive" initial deformations resulting from the two phase flow, but the particles will eventually pack themselves together to a quasi non-deformable matrix. The area mean of the velocity magnitude looks flat in this region, however there is still observed local particle displacements around the growing fingers. The arrest time of the constricted deformable sample is assumed to depend on initial packing density and invasion pressure. The open deformable samples however, has two observed regimes. The first is observed at high invasion pressures (50mbar, 100mbar), and is characterized by an "explosive" initial deformation which never stops during the invasion, meaning that some particles are continuously pushed outwards. At breakthrough, this behavior stops as suddenly as it began. The other regime is observed for the lower invasion pressures (25mbar,50mbar), and is characterized by a constricted deformable start, i.e. the particles are initially displaced "explosively" as usual, then the main flow of particles is arrested in a intermediate stage. When the displacement front approaches the open surface, an "avalanche" of particles occurs and lasts until breakthrough. It is observed that the fingers inducing an avalanche will break through the sample first.

Finally, a visual characterization of the patterns. Starting with the non-deformable pattern, these have the most obvious fractal behavior and scale invariance, consistent with analyses. They look just like they are "supposed" to in the viscous fingering regime: Long, thin fingers with no loops. The patterns in the constricted deformable samples *looks* similar for all invasion pressures: initially thick and straight fingers have a crossover to a behavior looking like viscous fingering. At last, the patterns in the open deformable samples begins with thick straight fingers which goes over to a mixture of fracturing and viscous fingers for the patterns with pressures 25mbar and 50mbar, while the patterns with pressures 75mbar and 100mbar seem to be dominated by fractured conduits.

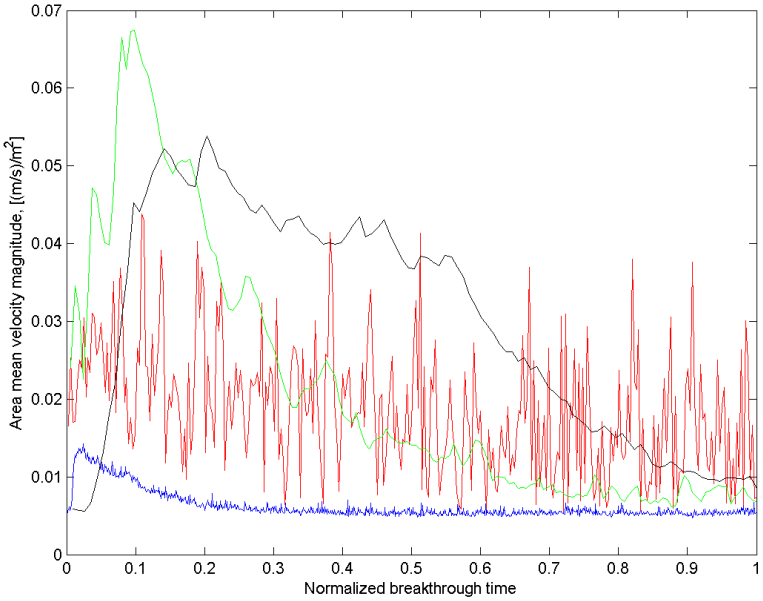

Figure 6.23: The area mean velocity magnitude for the constricted deformable samples vs. the normalized breakthrough time. Blue=CD25, Red=CD50, Green=CD75 and Black=CD100. It actually looks like CD50 was shaken a little during capuring, as for OD50.

When we think of it, the patterns we observe visually seem to be related to the displacement regimes found with the PIV analysis.

6.6 Ideas for further investigation

Due to the particle displacement regimes, it would be interesting to investigate such flow with a form of pressure sensor at the constricting rim, or simply use a rim with known elasticity that could be tracked visually with a high speed camera.

Another interesting improvement would be to increase the experimental resolution, if it was possible to perform such experiments in a larger cell with the same particle sizes.

To obtain the local distributions of pressure gradients in a circular non-deformable viscous fingering experiment, it may be possible to use a seeded defending fluid and capture the invasion with a high speed camera. The resulting experimental data should be suited for PIV processing to obtain the velocity field of the defending fluid. This velocity field could be used together with Darcy's eqution to estimate the pressure gradients between each captured frame, amongst possible other revealed effects.

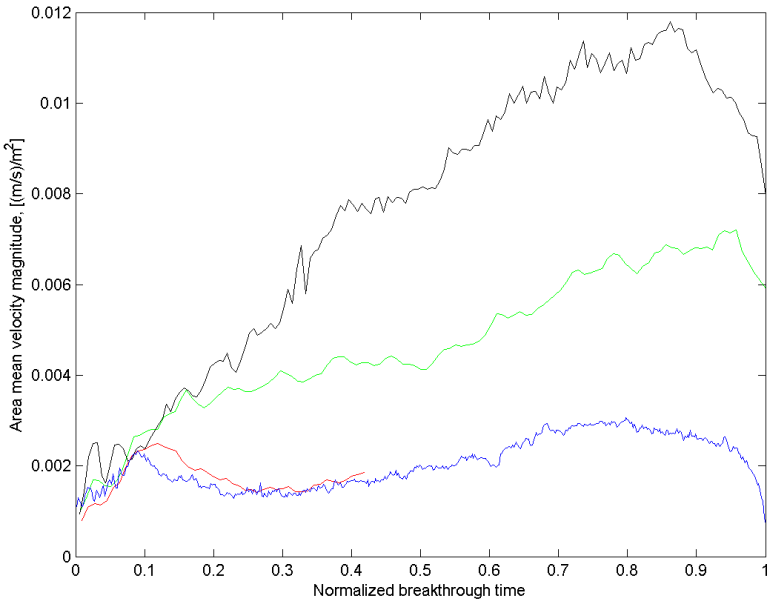

Figure 6.24: The area mean velocity magnitude for the open deformable samples vs. the normalized breakthrough time. Blue=OD25, Red=OD50, Green=OD75 and Black=OD100. Remember that 0D50 was shaking, so this part is removed.

Appendix A

Simulations

A.1 Diffusion Limited Aggregation

Diffusion Limited Aggregation, *DLA*, is an algorithm used to simulate the viscous fingering regime of two phase flow in porous media [1].

For a circular porous media sample, as investigated in this thesis, the algorithm used with Matlab is as follows:

```
%This program performs a simulation of DLA in a circular model.
function DLA


%Create a frame for the simulation
size=input('Define even numbered pixel-size of simulation frame :'); %Define model size
step=input('Define the pixel length of each random walk :'); %Define step-length
frame=zeros(size,size); %Empty size x size frame for simulation
boundary=zeros(size,size);%Empty size x size frame to define boundary
center=0.5*size;
frame(center,center)=1; %Center seed


%Create the model boundary
R=0.4736*size; %Radius of circular model (Similar to experiments)
for i=1:size;
   for j=1:size;
        if sqrt(dot([i-center,j-center],[i-center,j-center]))>=R;
            boundary(i,j)=1; %Fills outside of model
        end
        if sqrt(dot([i-center,j-center],[i-center,j-center]))>=R+1;
            boundary(i,j)=0; %Creates an outline on the boundary
        end
    end
end
Stats=regionprops(im2bw(boundary),'PixelList');
Boundpos=Stats.PixelList;


%Create random walker at random site on model boundary
h=waitbar(0,'Simulating');
breakthrough=0;
while breakthrough==0;
    Randstart=Boundpos(randi(length(Boundpos)),:);
    a=Randstart(1);
    b=Randstart(2);
```

```
     %Walk algorithm
    move1=[-1,0,1]*step;
    move2=[-1,1]*step;
    fused=0;
    while fused==0;
        amove=move1(randi(length(move1))); %Motion in a-direction
        bmove=0;
        if amove==0;
            bmove=move2(randi(length(move2))); %Motion in b-direction
        end




         %Reflect walker attempting to leave model
        if sqrt(dot([(a+amove)-center,(b+bmove)-center],[(a+amove)-center,(b+bmove)-center]))>R+1;
            amove=0;
            bmove=0;
        end
        a=a+amove;
        b=b+bmove;




         %Fuse walker where it hits the growing cluster
        if frame(a+1,b)==1;
            frame(a,b)=1;
            fused=1;
        end
        if frame(a-1,b)==1;
            frame(a,b)=1;
            fused=1;
        end
        if frame(a,b+1)==1;
            frame(a,b)=1;
            fused=1;
        end
        if frame(a,b-1)==1;
            frame(a,b)=1;
            fused=1;
        end
        if frame(a+1,b+1)==1;
            frame(a,b)=1;
            fused=1;
        end
        if frame(a+1,b-1)==1;
            frame(a,b)=1;
            fused=1;
        end
        if frame(a-1,b+1)==1;
            frame(a,b)=1;
            fused=1;
        end
        if frame(a-1,b-1)==1;
            frame(a,b)=1;
            fused=1;
        end
    end
    %Check for breakthrough
    if sqrt(dot([a-center,b-center],[a-center,b-center]))>=R;
        breakthrough=1;
    end
    indicator=sqrt(dot([a-center,b-center],[a-center,b-center]));
    waitbar(indicator/R,h,['Fused at ' num2str(indicator/R) ' of model radius.']);
end
waitbar(1,h,'Done!');
close(h);
imshow(frame);
imwrite(frame,['DLA' num2str(size) '.png']);
end
```

A.2 Invasion Percolation

Invasion percolation, *IP*, is an algorthm used to simulate the capillary fingering regime of two phase flow in porous media [1].

For a circular porous media sample, as investigated in this thesis, the algorithm used with Matlab is as follows:

```
%This program performs a simulation of IP in a circular model.
function IP


%Create a frame for the simulation
size=input('Define even numbered side length (pixels) of simulation frame :'); %Define model size
frame=zeros(size,size); %Empty size x size frame for simulation
random=zeros(size,size); %Empty size x size frame to define random matrix
boundary=zeros(size,size);%Empty size x size frame to define boundary
center=0.5*size;
frame(center,center)=1; %Center seed


%Create the random numbers
R=0.4736*size; %Radius of circular model (Similar to experiments)
for i=1:size;
   for j=1:size;
        random(i,j)=2*randi(10);%Assign random even integer from 2 to 20
        if sqrt(dot([i-center,j-center],[i-center,j-center]))>=R;
            boundary(i,j)=1; %Fills outside of model
        end
    end
end
boundary=im2uint8(boundary);
random=im2uint8(random*(1/20));
model=(random-boundary)*(20/255) + boundary*(1/255);


%Preparations before IP simulation
se=strel('square',3); %3x3 square structure element
frame=im2bw(frame); %Transform frame to logical


%IP
h=waitbar(0,'Simulating');
s=1;
front=im2uint8(imdilate(frame,se)-frame)*(1/255); %First front
front=front.*model; %Random values at first front
while sum(sum(front==1))==0; %Check for breakthrough
    for a=2:2:20 %Find front minima
        if sum(sum(front==a))>0;
            frame=frame+(front==a); %Fill front minima
            break
        end
    end
    front=im2uint8(imdilate(frame,se)-frame)*(1/255); %Update front
    front=front.*model; %Random values at updated front
    waitbar(1,h,['Iteration number ' num2str(s)]);
    s=s+1;
end
%Save IP image
imwrite(frame,['IP' num2str(size) '.png']);
imshow(frame);
close('h');
```

Appendix B

Image processing with Matlab

B.1 Important Matlab commands for image processing

Bibliography

[1] K.T.Tallakstad (2007). *Steady-state, simultaneous, two-phase flow in porous media.*

[2] J.Feder (1996). *Flow in Porous Media.* Lecture notes.

[3] R.A.Freedman, H.D.Young, A.L.Ford (2008). *University Physics, 12th ed.* Pearson Addison-Wesley.

[4] K.J.Måløy, J.Feder, T.Jøssang (1985). *Viscous Fingering Fractals in Porous Media.* Phys. Rev. Lett, **55** 2688.

[5] R.Holtzman, M.L.Szulczewski, R.Juanes (2012). *Capillary Fracturing in granular media.* (Preprint).

[6] J.Feder (1988). *Fractals.* Plenum Press.

[7] M.Frame, B.Mandelbrot, N.Neger. *classes.yale.edu/fractals/.*

[8] Viscosimeter manual.

[9] D.R.Lide. *CRC Handbook of Chemistry and Physics, 89th ed.*

[10] http://chemistry.about.com/od/mathsciencefundamentals/a/sigfigures.htm.

[11] M.L.Boas (2006). *Mathematical Methods in the Physical Sciences, 3rd ed.* Wiley.

[12] D.C.Lay (2006). *Linear Algebra and its applications, 3rd ed.* Pearson Addison-Wesley.

[13] http://www.coventry.ac.uk/ec/ nhunt/regress/good2.html.

[14] R.Holzmann, R.Juanes (2010). *Crossover from fingering to fracturing in deformable disordered media.* Phys. Rev. E, **82** 046305.